

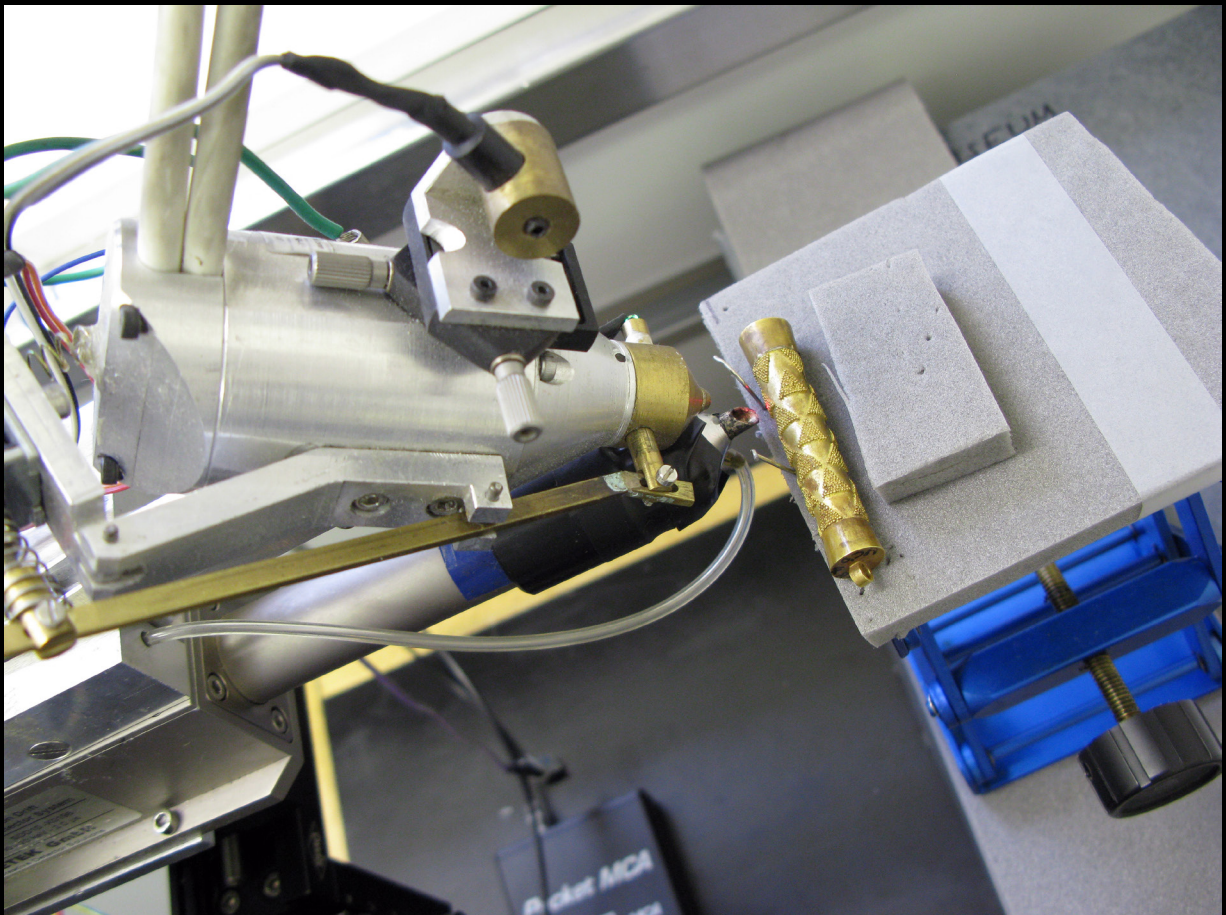


McDONALD INSTITUTE MONOGRAPHS

Ancient Egyptian gold

Archaeology and science in jewellery
(3500–1000 BC)

Edited by Maria F. Guerra, Marcos Martín-Torres
& Stephen Quirke



Ancient Egyptian gold



McDONALD INSTITUTE MONOGRAPHS

Ancient Egyptian gold Archaeology and science in jewellery (3500–1000 BC)

Edited by Maria F. Guerra, Marcos Martín-Torres
& Stephen Quirke

with contributions from

Wolfram Grajetzki, Maria F. Guerra, Marei Hacke, Mona Hess,
Susan La Niece, Quentin Lemasson, Lindsay MacDonald, Margaret Maitland,
Marcos Martín-Torres, Nigel Meeks, Gianluca Miniaci, Brice Moignard,
Jack Ogden, Claire Pacheco, Sandrine Pagès-Camagna, Laurent Pichon,
Matthew Ponting, Campbell Price, Stephen Quirke, Martin Radtke,
Uwe Reinholz, Ian Shaw, Jim Tate, Isabel Tissot & Lore Troalen

Published by:

McDonald Institute for Archaeological Research
University of Cambridge
Downing Street
Cambridge, UK
CB2 3ER
(0)(1223) 339327
eaj31@cam.ac.uk
www.mcdonald.cam.ac.uk



McDonald Institute for Archaeological Research, 2023

© 2023 McDonald Institute for Archaeological Research.

Ancient Egyptian gold is made available under a Creative Commons Attribution-NonCommercial-NoDerivatives 4.0 (International) Licence:
<https://creativecommons.org/licenses/by-nc-nd/4.0/>

Content within this publication is licensed under CC BY-NC-ND 4.0, with the exception of: © The Trustees of the British Museum. Shared under a Creative Commons Attribution-NonCommercial-ShareAlike 4.0 International (CC BY-NC-SA 4.0) licence. © National Museums Scotland. Shared under a Creative Commons Attribution-NonCommercial 4.0 (CC BY-NC 4.0) licence.

ISBN: 978-1-913344-13-9

On the front cover: *Analysis of the gold cylindrical amulet from Haraga at The Petrie Museum of Egyptian Archaeology (UC6482) using a portable XRF spectrometer.*
On the back cover: *Details under the SEM of the triangular designs of granulation on the tube of the cylindrical amulet from Haraga.*

Cover design by Dora Kemp and Ben Plumridge.
Typesetting and layout by Ben Plumridge.

Edited for the Institute by Matthew Davies (*Series Editor*).

CONTENTS

| | | |
|--------------------|--|-------|
| Contributors | | xi |
| Figures | | xiii |
| Tables | | xx |
| Editorial foreword | | xxiii |
| Part I | Gold and goldsmiths in ancient Egypt | |
| <i>Chapter 1</i> | Gold, an exceptional material | 3 |
| | MARIA F. GUERRA | |
| | Why gold? | 3 |
| | Exploiting gold sources | 4 |
| | Towards a gold metallurgy? | 8 |
| | From grain to object | 10 |
| <i>Chapter 2</i> | Centres of goldworking in ancient Egypt: Egyptological questions and sources | 27 |
| | STEPHEN QUIRKE | |
| | Archaeology of procurement and archaeology of production | 29 |
| | Bronze Age Egyptian written sources on procurement and working of gold | 37 |
| | Interpreting ancient Egyptian depictions of metal-working | 57 |
| | Concluding questions | 67 |
| <i>Chapter 3</i> | Jewellery in Egyptian burials | 75 |
| | WOLFRAM GRAJETZKI | |
| | Three level system of Egyptian burials | 75 |
| | Chronological overview | 76 |
| <i>Chapter 4</i> | Jewellery manufacture: an Egyptian quartet | 87 |
| | JACK OGDEN | |
| | Wire | 88 |
| | Engraving | 95 |
| | Gold cladding | 96 |
| | Enamel | 99 |
| <i>Chapter 5</i> | Reflections on gold: colour and workshop practices in Egypt | 105 |
| | MARIA F. GUERRA | |
| | A question of colour | 105 |
| | Making colourful strings | 108 |
| | One object, several goldsmiths | 112 |
| | Gold, another colour | 114 |
| | Gold alloys, chance or circumstances? | 118 |
| Part II | New analyses of ancient Egyptian jewellery | |
| <i>Chapter 6</i> | Analytical approaches to Egyptian goldwork | 131 |
| <i>Chapter 6.1</i> | Analysing gold jewellery | 133 |
| | MARIA F. GUERRA | |
| <i>Chapter 6.2</i> | Goldwork under white light and X-rays: inferring technologies | 137 |
| | LORE TROALEN & MARIA F. GUERRA | |

| | | |
|--------------------|---|-----|
| <i>Chapter 6.3</i> | Egyptian gold jewellery under the SEM-EDS | 143 |
| | MARIA F. GUERRA | |
| | From optical to electron microscopy | 143 |
| | Imaging with SEM | 144 |
| | SEM-EDS microanalysis | 147 |
| <i>Chapter 6.4</i> | Elemental analysis of goldwork with portable XRF equipment | 149 |
| | MARIA F. GUERRA & MARCOS MARTINÓN-TORRES | |
| <i>Chapter 6.5</i> | New analytical development for the analysis of Egyptian jewellery at AGLAE: mapping hard soldered joins and PGE inclusions | 153 |
| | QUENTIN LEMASSON, BRICE MOIGNARD, CLAIRE PACHECO, LAURENT PICHON & MARIA F. GUERRA | |
| | Fast mapping with PIXE at AGLAE | 153 |
| | Analytical challenges | 154 |
| | Estimating the depth of analysis | 155 |
| | Homogeneity of the analytical data | 155 |
| | Limits of detection | 157 |
| | PGE inclusions on hard soldered joins | 157 |
| | Conclusion | 158 |
| <i>Chapter 6.6</i> | Double Dispersive X-Ray Fluorescence analysis for the provenance of gold | 159 |
| | MARTIN RADTKE & UWE REINHOLZ | |
| | D ² XRF | 159 |
| | D ² XRF performance | 161 |
| | Application | 164 |
| | Conclusions | 164 |
| <i>Chapter 6.7</i> | 3D imaging, colour and specularity of an Egyptian Scarab | 165 |
| | LINDSAY MACDONALD & MONA HESS | |
| | 3D digitization | 165 |
| | Evaluation of 3D reconstruction methods | 167 |
| <i>Chapter 6.8</i> | The corrosion of precious metals: the case of Egyptian goldwork | 175 |
| | ISABEL TISSOT & MARIA F. GUERRA | |
| | Corrosion of precious metals | 175 |
| | Corrosion of Egyptian goldwork | 177 |
| | Characterization of the corroded surface | 179 |
| | Intergranular corrosion and stress corrosion cracking | 183 |
| | Conclusions | 183 |
| <i>Chapter 7</i> | The early jewellery | 193 |
| <i>Chapter 7.1</i> | The early jewellery analysed | 195 |
| | MARIA F. GUERRA | |
| <i>Chapter 7.2</i> | Introduction to sites | 197 |
| | WOLFRAM GRAJETZKI | |
| | Abydos | 197 |
| | Qau and Badari | 197 |
| <i>Chapter 7.3</i> | Predynastic and Early Dynastic goldwork from Abydos | 201 |
| | MARIA F. GUERRA, NIGEL MEEKS & STEPHEN QUIRKE | |
| | Predynastic diadem from tomb 1730 at Abydos | 201 |
| | Beads and gold foils from 1st Dynasty tombs at Abydos | 206 |

| | | |
|--------------------|--|-----|
| <i>Chapter 7.4</i> | First Intermediate Period goldwork from Qau and Badari MARIA F. GUERRA, MARCOS MARTINÓN-TORRES & STEPHEN QUIRKE | 215 |
| | Polychrome strings with cowrie-shaped beads | 215 |
| | The large beads | 219 |
| | The amulet pendants | 222 |
| | Making small ring beads | 226 |
| | The gold alloys | 228 |
| <i>Chapter 8</i> | Middle Kingdom jewellery | 245 |
| <i>Chapter 8.1</i> | Jewellery in the Middle Kingdom MARIA F. GUERRA | 247 |
| <i>Chapter 8.2</i> | Haraga tomb 72 LORE TROALEN, MARGARET MAITLAND & MARIA F. GUERRA | 249 |
| | The gold jewellery | 249 |
| | The gold alloys | 255 |
| | Conclusion | 258 |
| <i>Chapter 8.3</i> | Riqqa tomb 124 LORE TROALEN, MARIA F. GUERRA, MARGARET MAITLAND, MATTHEW PONTING & CAMPBELL PRICE | 261 |
| | Manufacture and restoration | 261 |
| | Analytical data | 264 |
| <i>Chapter 8.4</i> | Objects from excavations at Haraga, Lahun and other sites MARIA F. GUERRA & STEPHEN QUIRKE | 267 |
| | The objects from Haraga | 267 |
| | The objects from Lahun | 270 |
| | Objects from Naqada and Buhen | 272 |
| | The gold alloys | 274 |
| <i>Chapter 8.5</i> | Granulation in Egypt and the cylindrical amulet from Haraga MARIA F. GUERRA & NIGEL MEEKS | 279 |
| | A question of technology? | 279 |
| | Granulation in Egypt | 280 |
| | Technical study of amulet UC6482 | 283 |
| <i>Chapter 8.6</i> | Jewellery from Abydos excavated by Garstang MARIA F. GUERRA, LORE TROALEN, MATTHEW PONTING & IAN SHAW | 287 |
| | The analysed corpus | 287 |
| | Technological study | 288 |
| | The gold alloys | 291 |
| <i>Chapter 8.7</i> | Middle Kingdom jewellery in the collection of the Petrie Museum MARIA F. GUERRA & STEPHEN QUIRKE | 297 |
| <i>Chapter 8.8</i> | Necklace British Museum EA3077 said to be from Thebes NIGEL MEEKS, SUSAN LA NIECE, STEPHEN QUIRKE & MARIA F. GUERRA | 303 |
| <i>Chapter 9</i> | Second Intermediate Period jewellery | 313 |
| <i>Chapter 9.1</i> | Jewellery in the Second Intermediate Period MARIA F. GUERRA | 315 |

| | | |
|---------------------|--|-----|
| <i>Chapter 9.2</i> | The Qurna burial | 317 |
| | LORE TROALEN, JAMES TATE & MARIA F. GUERRA | |
| | The Qurna gold jewellery | 317 |
| | Gold alloys from Qurna | 318 |
| | Joining technique | 322 |
| | Conclusions | 326 |
| <i>Chapter 9.3</i> | Second Intermediate Period jewellery in the collection of the British Museum | 327 |
| | SUSAN LA NIECE, GIANLUCA MINIACI, MAREI HACKE & MARIA F. GUERRA | |
| | Technical description | 327 |
| | Gold alloys and joining technique | 331 |
| | Conclusions | 332 |
| <i>Chapter 9.4</i> | Jewellery bearing the names of Ahhotep and Ahmose | 335 |
| | MARIA F. GUERRA & SANDRINE PAGÈS-CAMAGNA | |
| | The jewellery construction | 337 |
| | The gold alloys and the joining technique | 340 |
| | Conclusions | 343 |
| <i>Chapter 9.5</i> | Second Intermediate Period jewellery in the collection of the Petrie Museum | 345 |
| | MARIA F. GUERRA, MARCOS MARTINÓN-TORRES & STEPHEN QUIRKE | |
| | Jewellery from Qau | 345 |
| | Jewellery bearing the names of Kamose and Seqenenra Taa | 349 |
| | The gold alloys | 352 |
| | Conclusions | 354 |
| <i>Chapter 10</i> | New Kingdom jewellery | 359 |
| <i>Chapter 10.1</i> | Jewellery in the New Kingdom | 361 |
| | MARIA F. GUERRA | |
| <i>Chapter 10.2</i> | Jewellery from tomb 296 at Riqqa | 363 |
| | LORE TROALEN & MARIA F. GUERRA | |
| | The group of jewellery | 363 |
| | The gold alloys and the soldering process | 363 |
| <i>Chapter 10.3</i> | Making pennanular ear ornaments in Egypt | 369 |
| | MARIA F. GUERRA | |
| | The ribbed penannular earrings | 370 |
| | Penannular earrings with one tube | 374 |
| | The gold alloys | 376 |
| | Concluding remarks | 380 |
| | Appendix: Ribbed penannular earrings with triangular tubes | 381 |
| <i>Chapter 10.4</i> | Finger-rings | 387 |
| | MARIA F. GUERRA, SUSAN LA NIECE, NIGEL MEEKS, STEPHEN QUIRKE & LORE TROALEN | |
| | Rings for the fingers in Egypt | 387 |
| | Swivelling finger-rings and signet rings in the collection of the British Museum | 389 |
| | Finger-rings supposedly from the Royal Tomb at Amarna and comparators | 394 |
| | New Kingdom finger-rings with wires | 404 |
| <i>Chapter 10.5</i> | Jewellery reportedly from the Royal Tomb at Amarna | 411 |
| | LORE TROALEN, MARIA F. GUERRA & MARGARET MAITLAND | |

| | | |
|---------------------|---|-----|
| <i>Chapter 10.6</i> | New Kingdom strings in the collection of the British Museum | 419 |
| | NIGEL MEEKS, SUSAN LA NIECE & MARIA F. GUERRA | |
| | String EA14696 | 419 |
| | String EA66827 | 424 |
| | The gold alloys | 429 |
| <i>Chapter 10.7</i> | On beads, pendants, scarabs and chains dated to the New Kingdom | 433 |
| | MARIA F. GUERRA & STEPHEN QUIRKE | |
| | Technological study | 433 |
| | The gold alloys | 439 |
| <i>Chapter 11</i> | Towards a conclusion: Qurna in context | 449 |
| | MARIA F. GUERRA | |
| | The Qurna collar and the use of hard soldering in Egypt | 451 |
| | Egyptian tiny beads and the Qurna child's necklace | 455 |
| | Puzzling Qurna earrings | 457 |
| | The whitish and heavily worn Qurna girdle | 465 |
| | Egyptian gold alloys and the Qurna group | 468 |
| | Final remarks | 475 |
| <i>Appendix 1</i> | Map of Egypt with cited sites | 481 |
| <i>Appendix 2</i> | Egyptian chronology 4th millennium BC – AD 395 | 482 |
| <i>Appendix 3</i> | Kings cited in text, with tentative dates, by dynasty | 483 |
| <i>Appendix 4</i> | Sudan chronology | 484 |
| <i>Appendix 5</i> | List of objects analysed | 485 |
| <i>Appendix 6</i> | Index of objects analysed | 489 |
| <i>Appendix 7</i> | Illustration credits | 496 |

CONTRIBUTORS

WOLFRAM GRAJETZKI

University College London, Institute of
Archaeology, 31–34 Gordon Square, London WC1H
0PY, UK.

Email: w.grajetzki@ucl.ac.uk

MARIA FILOMENA GUERRA

Centre national de la recherche scientifique,
UMR 8233 (Monaris), Sorbonne Université – CNRS,
4 Place de Jussieu, 75252 Paris Cedex 05, France.

Email: maria.guerra@cnsr.fr

MAREI HACKE

Swedish National Heritage Board,
Riksantikvarieämbetet, Kulturvårdsavdelningen,
Box 1114, 621 22 Visby, Sweden.

Email: marei.hacke@raa.se

MONA HESS

Otto-Friedrich-Universität Bamberg,
Institut für Archäologische Wissenschaften,
Denkmalwissenschaften und Kunstgeschichte,
Am Zwinger 4 (Villa), 96047 Bamberg, Germany.

Email: mona.hess@uni-bamberg.de

SUSAN LA NIECE

The British Museum, Department of Scientific
Research, Great Russell Street, London WC1B 3DG,
UK.

Email: slaniece@britishmuseum.org

QUENTIN LEMASSON

Centre de Recherche et de Restauration des Musées
de France, Palais du Louvre – Porte des Lions,
14, quai François Mitterrand, 75001 Paris, France.

Email: quentin.lemasson@culture.gouv.fr

LINDSAY MACDONALD

University College London, Department of
Civil, Environmental and Geomatic Engineering,
Chadwick Building, Gower Street, London WC1E
6BT, UK.

Email: lindsay.macdonald@ucl.ac.uk

MARGARET MAITLAND

National Museums Scotland, World Cultures
Department, Chambers Street, Edinburgh EH1 1JF,
UK.

Email: m.maitland@nms.ac.uk

MARCOS MARTINÓN-TORRES

University of Cambridge, McDonald Institute
for Archaeological Research, Downing Street,
Cambridge CB2 3ER, UK.

Email: m.martinon-torres@arch.cam.ac.uk

NIGEL MEEKS

The British Museum, Department of Scientific
Research, Great Russell Street, London WC1B 3DG,
UK.

Email: nmeeks@britishmuseum.org

GIANLUCA MINIACI

University of Pisa, Department of Civiltà e Forme
del Sapere, Via Trieste 40, 56126 Pisa, Italy.

Email: gianluca.miniaci@unipi.it

BRICE MOIGNARD

Centre de Recherche et de Restauration des Musées
de France, Palais du Louvre – Porte des Lions,
14, quai François Mitterrand, 75001 Paris, France.

Email: brice.moignard@culture.gouv.fr

JACK OGDEN

Society of Jewellery Historians, Scientific Research,
The British Museum, London WC1B 3DG, UK.

Email: jack@striptwist.com

CLAIRE PACHECO

Centre de Recherche et de Restauration des Musées
de France, Palais du Louvre – Porte des Lions,
14, quai François Mitterrand, 75001 Paris, France.

Email: claire.pacheco@culture.gouv.fr

SANDRINE PAGES-CAMAGNAT

Centre de Recherche et de Restauration des Musées
de France, Palais du Louvre – Porte des Lions,
14, quai François Mitterrand, 75001 Paris, France.

LAURENT PICHON

Centre de Recherche et de Restauration des Musées
de France, Palais du Louvre – Porte des Lions,
14, quai François Mitterrand, 75001 Paris, France.

Email: laurent.pichon@culture.gouv.fr

MATTHEW PONTING

University of Liverpool, Department of
Archaeology, Classics and Egyptology, 12–14
Abercromby Square, Liverpool L69 7WZ, UK.

Email: M.Ponting@liverpool.ac.uk

CAMPBELL PRICE

The University of Manchester, Manchester Museum
Department, Oxford Road, Manchester M13 9PL,
UK.

Email: campbell.price@manchester.ac.uk

STEPHEN QUIRKE

University College London, Institute of
Archaeology, 31–34 Gordon Square, London WC1H
0PY, UK.

Email: s.quirke@ucl.ac.uk

MARTIN RADTKE

Bundesanstalt für Materialforschung und -prüfung,
Richard-Willstätter-Straße 11, 12489 Berlin,
Germany.

Email: martin.radtke@bam.de

UWE REINHOLZ†

Bundesanstalt für Materialforschung und -prüfung,
Richard-Willstätter-Straße 11, 12489 Berlin,
Germany.

IAN SHAW

University of Liverpool, Department of
Archaeology, Classics and Egyptology, 12–14
Abercromby Square, Liverpool L69 7WZ, UK.

Email: Ishaw@liverpool.ac.uk

JIM TATE

National Museums Scotland, Chambers Street,
Edinburgh EH1 1JF, UK.

Email: j.tate@nms.ac.uk

ISABEL TISSOT

NOVA University of Lisbon, LIBPhys, Campus da
Caparica, 2829-516 Caparica, Portugal.

Email: Isabeltissot@fct.unl.pt

LORE TROALEN

National Museums Scotland, Collections Services
Department, National Museums Collection Centre,
242 West Granton Road, Edinburgh EH5 1JA, UK.

Email: l.troalen@nms.ac.uk

Figures

| | | |
|------|--|----|
| 1.1 | <i>Au-Ag-Cu ternary phase diagram showing the relation between composition and colour of the alloy.</i> | 4 |
| 1.2 | <i>Tomb 15, Beni Hassan: workshop scene where different types of objects are plated and gilt.</i> | 4 |
| 1.3 | <i>Formation of the main types of gold placer deposits.</i> | 5 |
| 1.4 | <i>Gold panning in Lusitania (from De Re Metallica) and a modern pan containing gold nuggets.</i> | 6 |
| 1.5 | <i>Amounts of silver in gold grains from mines in the Egyptian Eastern Desert.</i> | 7 |
| 1.6 | <i>Tomb of Wepemnefert at Giza: scene showing metallurgical processes.</i> | 12 |
| 1.7 | <i>Representation of some solder alloys in the Au-Ag-Cu ternary phase diagram.</i> | 14 |
| 2.1 | <i>Web of operations in Roman gold mining at Três Minas (2nd century AD).</i> | 28 |
| 2.2 | <i>From ore to object: metal production sequence.</i> | 29 |
| 2.3 | <i>Gold-mining sites in Egypt assigned to the 'Old to Middle Kingdom' phase.</i> | 30 |
| 2.4 | <i>Identified Old to Middle Kingdom sites of copper, gold and lead extraction.</i> | 30 |
| 2.5 | <i>The Balat workshop at phase 3, rooms 7–8 at right, 5–6 at left.</i> | 34 |
| 2.6 | <i>The Balat workshop: distribution of ceramic finds related to metalworking.</i> | 35 |
| 2.7 | <i>Ramesside jar rim sherd with start of the verse on the sculptor and goldsmith in the Teaching of Khety.</i> | 39 |
| 2.8 | <i>Locations of inscriptions with smnty titles in expedition areas.</i> | 42 |
| 2.9 | <i>Unprovenanced limestone stela referring to 'the chapel of the goldsmith Kegy'.</i> | 48 |
| 2.10 | <i>Glazed steatite scarabs inscribed for the goldsmith Nebipu and the overseer of goldsmiths Saptah.</i> | 49 |
| 2.11 | <i>Stela of the head goldsmiths Panehsy and Paramheb.</i> | 50 |
| 2.12 | <i>Miniature votive stela of the goldsmith Khonsumes.</i> | 53 |
| 2.13 | <i>New Kingdom chapels among the Old Kingdom monuments of north central Saqqara.</i> | 55 |
| 2.14 | <i>Papyrus of head of makers or fine gold-leaf Neferrenpet, with gold foil decoration.</i> | 57 |
| 2.15 | <i>The context of metalworking depictions (melting, pouring and hammering) and necklace-stringing.</i> | 60 |
| 2.16 | <i>Depictions of metalworking in the tomb-chapel of vizier Rekhmira, 18th Dynasty, Thebes.</i> | 63 |
| 2.17 | <i>Depictions relating to gold working in the tomb-chapel of Khay, Saqqara.</i> | 66 |
| 2.18 | <i>Crucible from Badari 4964, c. 2100–2000 BC.</i> | 69 |
| 3.1 | <i>Categories of Egyptian burials: three steps of burial equipment types.</i> | 76 |
| 3.2 | <i>Examples of Old Kingdom funerary jewellery: two diadems and gold wire with beads.</i> | 77 |
| 3.3 | <i>Amulets, found in burials at Qau and Badari, First Intermediate Period.</i> | 79 |
| 3.4 | <i>Necklaces from the burial of Mayet with a torque-like string.</i> | 80 |
| 3.5 | <i>Necklace of Wah.</i> | 81 |
| 3.6 | <i>Burial of Nubhetpti-khered with the typical jewellery equipment of a high status person.</i> | 81 |
| 3.7 | <i>Objects from the jewellery box of the king's daughter Sithathor at Dahshur.</i> | 83 |
| 3.8 | <i>The broad collar of Senebtysy, especially made for the burial.</i> | 83 |
| 4.1 | <i>Wire drawing showing how the wire is compressed and elongated by wire drawing.</i> | 88 |
| 4.2 | <i>Gold bracelet from Mostagedda. First Intermediate Period.</i> | 89 |
| 4.3 | <i>Detail of the bracelet in Figure 4.2 showing break.</i> | 89 |
| 4.4 | <i>The construction of strip-twist wire.</i> | 90 |
| 4.5 | <i>Detail of the wire and granulation on one of Tutankhamun's daggers (18th Dynasty).</i> | 90 |
| 4.6 | <i>Gold and lapis lazuli scarab ring (17th Dynasty).</i> | 91 |
| 4.7 | <i>Detail of the ring in Figure 4.6 showing the seams on the wire.</i> | 91 |
| 4.8 | <i>Drawing showing how strip drawing curls a strip round into a circular section.</i> | 91 |
| 4.9 | <i>Magnesite jar with gold lid. From the tomb of Khasekhemy at Abydos, 2nd Dynasty.</i> | 92 |
| 4.10 | <i>Detail of the gold lid and binding wire on the jar in Figure 4.9.</i> | 92 |
| 4.11 | <i>Detail of the twisted wire 'ropes' on the jar in Figure 4.9.</i> | 93 |
| 4.12 | <i>Detail of the wires on the jar in Figure 4.9.</i> | 93 |
| 4.13 | <i>Gold wire diadem from the tomb of Senebtysy at Lisht, late 12th to early 13th Dynasty.</i> | 94 |
| 4.14 | <i>Gold base from a scarab ring with the name of Ameny from Lisht, Middle Kingdom.</i> | 96 |
| 4.15 | <i>Detail of the ring in Figure 4.14.</i> | 96 |
| 4.16 | <i>Gold base on a gold and amethyst scarab ring of Senusret III from Dahshur.</i> | 97 |
| 4.17 | <i>Detail of the engraving on the ring in Figure 4.16.</i> | 97 |
| 4.18 | <i>Detail of the base plate on the ring in Figure 4.6 showing chased inscription and recent scratches.</i> | 97 |
| 4.19 | <i>Two of the pendants from a New Kingdom Egyptian collar found in tomb 93 at Enkomi, Cyprus.</i> | 98 |

| | | |
|------|--|-----|
| 4.20 | <i>Detail of a gold and glass (perhaps enamel) pectoral from the tomb of Wendjebaendjed.</i> | 100 |
| 4.21 | <i>Detail of a gold and glass (perhaps enamel) pectoral from the tomb of Wendjebaendjed.</i> | 100 |
| 4.22 | <i>Detail of the enamelled disk in the centre of a gold bowl from the tomb of Wendjebaendjed.</i> | 101 |
| 5.1 | <i>Gold shell-shaped pendants from several tombs, some inscribed.</i> | 106 |
| 5.2 | <i>Detail of the pectoral of Sathathoriunet with the name of Senusret II.</i> | 107 |
| 5.3 | <i>Components of different colours in a string of beads from Badari, tomb 4903.</i> | 107 |
| 5.4 | <i>The four bracelets from the tomb of king Djer at Umm el-Qaab.</i> | 108 |
| 5.5 | <i>Second bracelet and one of the 'hour-glass' beads in the bracelet.</i> | 109 |
| 5.6 | <i>Broad anklets and bracelet of Sathathoriunet, 12th Dynasty, Lahun.</i> | 110 |
| 5.7 | <i>One of the ring beads from the Qurna child's necklace.</i> | 111 |
| 5.8 | <i>Details of the beads and separators strung in Sathathoriunet's anklets and bracelet.</i> | 111 |
| 5.9 | <i>Detail of necklace British Museum EA3077, said to be from Thebes.</i> | 112 |
| 5.10 | <i>Feline-head shaped hollow gold beads from two girdles.</i> | 113 |
| 5.11 | <i>The ropes of motifs in two items from the tomb of Tutankhamun.</i> | 114 |
| 5.12 | <i>Reflectivity spectra of copper, silver, and gold and estimated reflectivity of several Au-Ag alloys.</i> | 116 |
| 5.13 | <i>Detail of string of beads from tomb 7923 at Qau.</i> | 117 |
| 5.14 | <i>Elemental composition of objects dated from Predynastic to First Intermediate Period.</i> | 117 |
| 6.1 | <i>Compact high-resolution video microscope with colour image sensor.</i> | 137 |
| 6.2 | <i>Strip-twisted wire in a Roman Period earring, showing the helical seam and the hollow interior.</i> | 138 |
| 6.3 | <i>Roman Period bracelet and X-radiograph of its pair.</i> | 138 |
| 6.4 | <i>X-radiograph of string of beads from Haraga, tomb 72.</i> | 139 |
| 6.5 | <i>X-radiograph of finger-ring NMS A.1883.49.8.</i> | 140 |
| 6.6 | <i>X-radiograph of finger-ring NMS A.212.12.</i> | 140 |
| 6.7 | <i>The main emissions by bombardment with an electron beam and radius of interaction volume.</i> | 144 |
| 6.8 | <i>Part of gold pendant in the form of a hawk with spread wings under the SEM.</i> | 145 |
| 6.9 | <i>SE images of a detail of pendant N 1855A.</i> | 146 |
| 6.10 | <i>SE images of granules and wires in pendant N 1855A.</i> | 146 |
| 6.11 | <i>SE images of pendant N 1855A, showing details related to the production of the granules.</i> | 147 |
| 6.12 | <i>SE image of a detail of the edge of pendant N 1855A.</i> | 148 |
| 6.13 | <i>CNRS portable XRF spectrometer, showing the positioning of the beam spot.</i> | 150 |
| 6.14 | <i>UCL Institute of Archaeology handheld XRF equipment.</i> | 151 |
| 6.15 | <i>The handheld XRF equipment of the C2RMF with its lightweight stand.</i> | 151 |
| 6.16 | <i>University of Liverpool handheld XRF equipment.</i> | 152 |
| 6.17 | <i>AGLAE external microprobe: location of the six detector, exit window, and video microscope.</i> | 154 |
| 6.18 | <i>Elemental distribution of Ir by PIXE in colour scale.</i> | 155 |
| 6.19 | <i>Elemental distribution of Cu, Ag, Au, Ir, Ru and Os by PIXE in colour scale.</i> | 158 |
| 6.20 | <i>The developed setup for D²XRF measurements.</i> | 160 |
| 6.21 | <i>Cu Kα peak for 0.1 mm and 1 mm beam size and using the second-order reflex.</i> | 162 |
| 6.22 | <i>Effect of energy dispersion of the pnCCD chip for an Au standard at the BAMline.</i> | 163 |
| 6.23 | <i>D²XRF spectrum of NA-Au-30 at the mySpot beamline.</i> | 163 |
| 6.24 | <i>Six views of scarab UC11365 illuminated by a circle of 16 flashlights.</i> | 166 |
| 6.25 | <i>Photogrammetric imaging setup with scarab UC11365 on target board.</i> | 166 |
| 6.26 | <i>Positioning scarab UC11365 on the baseboard of the UCL dome.</i> | 167 |
| 6.27 | <i>Photogrammetric reconstruction and detail showing erroneous cut by craftsperson.</i> | 167 |
| 6.28 | <i>3D point cloud generated by the colour laser scanner.</i> | 167 |
| 6.29 | <i>3D reconstruction from photometric normals.</i> | 167 |
| 6.30 | <i>Comparison of point cloud from photometric stereo reconstruction and laser scanner.</i> | 168 |
| 6.31 | <i>Measurement of gold band on a scarab.</i> | 169 |
| 6.32 | <i>Colorimetric coordinates of 10 measurements at different positions on the gold band around the scarab.</i> | 169 |
| 6.33 | <i>Image of scarab, with enlarged detail showing sampling locations for gold and steatite.</i> | 170 |
| 6.34 | <i>Intensity distributions from 64 lamps for a single pixel for steatite and gold.</i> | 170 |
| 6.35 | <i>Image components derived from processing the original set of 64 images: (left) albedo, (right) normals.</i> | 171 |
| 6.36 | <i>Image components: (left) specular quotient, (right) specular colour.</i> | 171 |
| 6.37 | <i>Scatter plot of specular vector angle vs normal vector angle and specular vs albedo colours.</i> | 172 |

| | | |
|-------|---|-----|
| 6.38 | <i>Fitting of flank and Lorentzian function and function generated.</i> | 172 |
| 6.39 | <i>Original photograph and rendered image, both illuminated from same hemisphere coordinates.</i> | 173 |
| 6.40 | <i>Detail of Early Bronze Age archer's armband, displaying a reddish corroded layer with iridescent effect.</i> | 176 |
| 6.41 | <i>Iron Age earring with stress-induced corrosion and crack in an Early Bronze Age diadem.</i> | 177 |
| 6.42 | <i>Corroded surfaces of a cartouche-shaped box and 12th Dynasty beads.</i> | 178 |
| 6.43 | <i>Fragments of corroded gold foils from burials excavated at Abydos, North Cemetery.</i> | 178 |
| 6.44 | <i>Fragments of wood with gold leaf excavated at Abydos, North Cemetery.</i> | 179 |
| 6.45 | <i>Gold foils with heterogeneous coloured surface and homogeneous red colour.</i> | 180 |
| 6.46 | <i>Gold versus silver contents obtained by μXRF for a gold foil with heterogeneous coloured surface.</i> | 181 |
| 6.47 | <i>Ratio Au/Ag versus S content obtained by μXRF for corroded and non-corroded areas.</i> | 181 |
| 6.48 | <i>FEG-SEM-SE micrographs of the heterogeneous corroded area of Abydos foil fragment 2.6.</i> | 182 |
| 6.49 | <i>FEG-SEM-SE micrographs of homogeneous red corroded areas of a gold fragment from Abydos and Haraga.</i> | 182 |
| 6.50 | <i>FEG-SEM-SE micrograph of the Haraga bead fragment with heterogeneous surface.</i> | 183 |
| 6.51 | <i>SEM-SE micrograph of the intergranular corrosion and corrosion products of the cartouche-shaped box.</i> | 184 |
| 7.1 | <i>Diadem from intact grave 1730 at Abydos.</i> | 202 |
| 7.2 | <i>Detail of diadem showing the tiny gold beads, with table of measurements for select beads.</i> | 202 |
| 7.3 | <i>Details under the SEM of the small gold ring beads in the diadem.</i> | 203 |
| 7.4 | <i>Method for making small rings.</i> | 203 |
| 7.5 | <i>SEM details of the small gold ring diadem beads.</i> | 204 |
| 7.6 | <i>Silver versus copper contents of the gold alloys used for the diadem compared to Predynastic jewellery.</i> | 205 |
| 7.7a | <i>Two of the four pieces of gold foil thought to be from Abydos tomb B10.</i> | 207 |
| 7.7b | <i>String of beads recorded as from tomb 500 at the funerary enclosure for king Djer.</i> | 207 |
| 7.8 | <i>Ball-shaped gold bead and biconical gold bead in Abydos tomb 500 string.</i> | 208 |
| 7.9 | <i>Scraped surface of the biconical gold bead suggesting a shaping or finishing process.</i> | 208 |
| 7.10a | <i>Silver versus copper contents for gold beads and foils from Abydos and other items.</i> | 210 |
| 7.10b | <i>Silver versus copper contents by date for the same objects.</i> | 210 |
| 7.11 | <i>Silver versus copper contents by date as in Figure 7.10b, adding hypothetical alloys.</i> | 212 |
| 7.12 | <i>String of beads from tomb 7923 at Qau.</i> | 216 |
| 7.13 | <i>Small ring beads from string UC18092 under the SEM showing production details.</i> | 217 |
| 7.14 | <i>The four cowrie beads from tomb 3053 at Matmar.</i> | 217 |
| 7.15 | <i>A detail of the string from tomb 4903 at Badari and of some of its gold beads.</i> | 218 |
| 7.16 | <i>One of the ribbed tubular gold beads from Badari tomb 4903 under the SEM.</i> | 219 |
| 7.17 | <i>One of the barrel beads from Badari tomb 4903.</i> | 219 |
| 7.18 | <i>Detail of string from Qau tomb 1030 showing several gold components.</i> | 220 |
| 7.19 | <i>Two of the spherical beads in the Qau tomb 1030 string.</i> | 220 |
| 7.20 | <i>Some of the gold beads from tomb 7777 at Qau.</i> | 221 |
| 7.21 | <i>Details of the decorated gold barrel bead from Qau tomb 7777.</i> | 221 |
| 7.22 | <i>One of the gold amulets in the shape of the god Heh in string from Badari tomb 4903.</i> | 222 |
| 7.23 | <i>Details of the flattened and rolled wires in gold Heh amulet from Badari tomb 4932.</i> | 223 |
| 7.24 | <i>Amulet pendants in the shape of a quail chick with crown, from tombs 5270 and 5281 at Badari.</i> | 223 |
| 7.25 | <i>Detail of string from tomb 3029 at Matmar, showing several components.</i> | 224 |
| 7.26 | <i>Details of the legs of bird amulets from Matmar tomb 3029.</i> | 224 |
| 7.27 | <i>Detail of gold string UC20649 from Badari tomb 4915.</i> | 225 |
| 7.28 | <i>Ankh-shaped, Taweret-shaped and bee-shaped amulets from Qau tomb 1030.</i> | 225 |
| 7.29 | <i>Ring beads from Badari tomb 4915, and one of their visible PGE inclusions.</i> | 227 |
| 7.30 | <i>The ring beads from Badari tomb 4915 under the SEM.</i> | 227 |
| 7.31 | <i>The tiny beads from Matmar 3029.</i> | 227 |
| 7.32 | <i>The tiny beads from Qau tomb 1030, showing variety of colour and shape.</i> | 229 |
| 7.33 | <i>Some of the ring beads of string UC20896 from Qau tomb 7777.</i> | 229 |
| 7.34 | <i>The variety of the small ring beads from Badari tomb 3306.</i> | 229 |
| 7.35 | <i>Silver versus copper contents for jewellery from Qau and Matmar.</i> | 231 |
| 7.36 | <i>Silver versus copper contents for jewellery from Qau and Matmar compared to other objects.</i> | 231 |
| 7.37 | <i>Some of the rings of a gilt copper chain from the tomb of king Khasekhemwy, Umm el-Qaab.</i> | 232 |
| 7.38 | <i>Silver versus copper contents of small ring beads from Qau and Badari.</i> | 234 |

| | | |
|------|--|-----|
| 7.39 | <i>Silver versus copper contents obtained for the bird amulets analysed.</i> | 234 |
| 7.40 | <i>Silver versus copper contents obtained for the bird and tiny amulets analysed.</i> | 236 |
| 7.41 | <i>Silver versus copper contents obtained for all amulet pendants analysed and button seal UC34110.</i> | 236 |
| 7.42 | <i>Unprovenanced button seal-amulet with details.</i> | 237 |
| 7.43 | <i>Silver versus copper contents obtained for all the analysed beads except the small ring beads.</i> | 237 |
| 7.44 | <i>Silver versus copper contents obtained for all the analysed amulets and beads.</i> | 239 |
| 7.45 | <i>Silver versus copper contents obtained for First Intermediate Period jewellery.</i> | 239 |
| 8.1 | <i>The gold jewellery from Haraga tomb 72.</i> | 250 |
| 8.2 | <i>Representation of a daughter of Ukhhotep IV, in his tomb-chapel at Meir.</i> | 251 |
| 8.3 | <i>Blue faience female figure from a burial at Deir el Bahari, Thebes.</i> | 251 |
| 8.4 | <i>The three gold catfish pendants from tomb 72.</i> | 251 |
| 8.5 | <i>Details from three strings from Haraga tomb 72.</i> | 252 |
| 8.6 | <i>String of biconical and ball beads and X-radiograph revealing various densities.</i> | 253 |
| 8.7 | <i>X-radiographs of two fish pendants, revealing the construction of each.</i> | 253 |
| 8.8 | <i>SEM-AEI micrographs of pendant NMS A.1914.1079.</i> | 254 |
| 8.9 | <i>SEM-AEI micrographs of pendant NMS A.1914.1080.</i> | 255 |
| 8.10 | <i>Silver versus copper contents obtained by analysis of the strings from Haraga tomb 72.</i> | 256 |
| 8.11 | <i>Silver versus copper contents obtained by analysis of the fish pendants from Haraga tomb 72.</i> | 256 |
| 8.12 | <i>PGE inclusion in pendants NMS A.1914.1080-1.</i> | 258 |
| 8.13 | <i>Gold objects from tomb 124 at Riqqa in the collection of the Manchester Museum.</i> | 262 |
| 8.14 | <i>Surface scratches and cracks of the restored pectoral and modern wires in the pendant.</i> | 262 |
| 8.15 | <i>Details of the winged beetle pendant.</i> | 263 |
| 8.16 | <i>The suspension rings of the pectoral and the winged beetle pendant.</i> | 263 |
| 8.17 | <i>Details of the shell shaped pendant, with visible surface scratches.</i> | 264 |
| 8.18 | <i>Silver versus copper contents obtained for the jewellery from tomb 124 at Riqqa.</i> | 265 |
| 8.19 | <i>Fish pendant from tomb 520 at Haraga, with a detail of the fish's body.</i> | 268 |
| 8.20 | <i>Fish pendant from Haraga tomb 520, showing the head and the copper-based tail.</i> | 268 |
| 8.21 | <i>Gold cowrie pendants and cylinder amulets with gold caps from tomb 211 at Haraga.</i> | 269 |
| 8.22 | <i>Details of the gold cylinder amulet from tomb 211 at Haraga.</i> | 269 |
| 8.23 | <i>Details under the SEM of granules soldered to the cylinder.</i> | 269 |
| 8.24 | <i>Detail of the pierced hole (modern?) used for suspension of the gold shell shaped pendant.</i> | 270 |
| 8.25 | <i>Restrung beads and amulets from Lahun, with a detail of the gold bead.</i> | 270 |
| 8.26 | <i>Details of the two ends of the gold bead in the string from Lahun.</i> | 271 |
| 8.27 | <i>Private-name scarab of steatite mounted in a gold sheet.</i> | 271 |
| 8.28 | <i>Two scraps of gold foil with decoration from royal tomb 8 at Lahun.</i> | 272 |
| 8.29 | <i>Lozenge shaped gold bead from the Egyptian fort at Buhen (Sudan).</i> | 273 |
| 8.30 | <i>Private-name scarab of amethyst set in a gold plinth, acquired during excavations at Naqada.</i> | 273 |
| 8.31 | <i>Black jasper scarab set in a gold base plate, from excavations at Naqada.</i> | 274 |
| 8.32 | <i>Silver versus copper contents obtained for the gold jewellery and foils from Haraga.</i> | 275 |
| 8.33 | <i>Silver versus copper contents obtained for the gold jewellery and foils from Lahun.</i> | 275 |
| 8.34 | <i>Silver versus copper contents obtained for the gold jewellery from different excavated sites.</i> | 277 |
| 8.35 | <i>Silver versus copper contents obtained for gold jewellery and foils from Lahun, Haraga and Riqqa.</i> | 277 |
| 8.36 | <i>Cylindrical amulet UC6482 from tomb 211 at Haraga.</i> | 280 |
| 8.37 | <i>Jewellery with granulation from Mereret's burial, Dahshur.</i> | 281 |
| 8.38 | <i>Cylindrical gold amulet pendant from Lisht North.</i> | 281 |
| 8.39 | <i>Hollow cylindrical gold amulet pendant from Saqqara.</i> | 282 |
| 8.40 | <i>The cap, suspension ring, and triangles in granulation of amulet UC6482.</i> | 283 |
| 8.41 | <i>The cracks on the surface of the Haraga cylindrical amulet.</i> | 284 |
| 8.42 | <i>SEM-SE image showing triangular geometrical designs of granulation.</i> | 284 |
| 8.43 | <i>One of the analysed triangles in granulation and composition of the granules and solders.</i> | 285 |
| 8.44 | <i>Gilded objects from Abydos tomb 381.</i> | 288 |
| 8.45 | <i>Fragments of gilded wooden artefacts from excavations at Abydos, tombs 533 and probably 432.</i> | 289 |
| 8.46 | <i>Gold mount for a heart-scarab, from Abydos tomb 405.</i> | 289 |
| 8.47 | <i>Details of the gold heart-scarab mount.</i> | 290 |

| | | |
|------|--|-----|
| 8.48 | <i>Cylindrical pendant amulet with gold caps from Abydos tomb 459.</i> | 290 |
| 8.49 | <i>One of the gold rings of the Abydos 459 cylinder amulet.</i> | 291 |
| 8.50 | <i>The gold caps of the Abydos 459 cylinder amulet.</i> | 291 |
| 8.51 | <i>Gold and electrum beads from Abydos tomb 492.</i> | 292 |
| 8.52 | <i>Silver versus copper contents obtained for the gold leaves and foils from Abydos.</i> | 293 |
| 8.53 | <i>Silver versus copper contents obtained for gold leaves and foils from Abydos, Haraga and Lahun.</i> | 293 |
| 8.54 | <i>Silver versus copper contents obtained for all the gold objects from Abydos.</i> | 294 |
| 8.55 | <i>PGE inclusion at the surface of the Abydos heart scarab mount.</i> | 294 |
| 8.56 | <i>Details of cylindrical case amulet UC52202.</i> | 298 |
| 8.57 | <i>Gold cowrie shell shaped bead with two holes at each end restrung in string UC8971.</i> | 298 |
| 8.58 | <i>Cowrie shell shaped beads in the girdles of Hepy and Sathathoriunet.</i> | 298 |
| 8.59 | <i>Some of the gold components of string UC8973.</i> | 299 |
| 8.60 | <i>Some of the gold components of string UC36475.</i> | 299 |
| 8.61 | <i>One of the barrel beads in string UC36475 made from gold foil.</i> | 299 |
| 8.62 | <i>Some of the small ring beads found in deposit 1300 at Sidmant.</i> | 300 |
| 8.63 | <i>Silver versus copper contents obtained for Middle Kingdom gold jewellery.</i> | 301 |
| 8.64 | <i>Some of the many PGE inclusions visible at the surface of gold cowrie shell shaped bead in string UC8971.</i> | 301 |
| 8.65 | <i>Silver versus copper contents of Middle Kingdom gold jewellery.</i> | 302 |
| 8.66 | <i>Components said to be from Thebes, restrung as a necklace, British Museum EA3077.</i> | 304 |
| 8.67 | <i>One of the cowrie shell beads, and the X-radiograph showing the spheres inside the beads.</i> | 304 |
| 8.68 | <i>X-radiograph showing the mounting of the two fish pendants.</i> | 305 |
| 8.69 | <i>Details of the two fish pendants.</i> | 305 |
| 8.70 | <i>One of the sidelock pendants, chased after mounting the upper gold sheet.</i> | 306 |
| 8.71 | <i>Front and X-radiograph of the papyrus umbel pendant with a god Heh amulet.</i> | 306 |
| 8.72 | <i>Cloisonné work of the papyrus umbel pendant and the body and arms of the Heh amulet.</i> | 307 |
| 8.73 | <i>SEM image of one of the spherical beads of gold foil.</i> | 307 |
| 8.74 | <i>Silver versus copper contents obtained by SEM-EDS for the components of necklace EA3077.</i> | 308 |
| 8.75 | <i>Point analysis tracking across the edge seam solder of a cowrie-shell shaped bead (EA3077).</i> | 308 |
| 9.1 | <i>Ahhotep's group of jewellery and weapons exhibited in the Egyptian Museum, Cairo.</i> | 316 |
| 9.2 | <i>The Qurna adult's jewellery set: necklace; bracelets; earrings; girdle.</i> | 318 |
| 9.3 | <i>SEM micrographs and X-Radiographic plate showing details of Qurna jewellery.</i> | 319 |
| 9.4 | <i>Silver versus copper contents obtained for the jewellery from the Qurna burial.</i> | 321 |
| 9.5 | <i>PGE inclusions in the adult's earrings and necklace.</i> | 322 |
| 9.6 | <i>SEM-AEI micrographs of the adult's and child's earrings.</i> | 323 |
| 9.7 | <i>X-radiographs revealing details of construction of the adult's jewellery.</i> | 324 |
| 9.8 | <i>SEM-SEI micrographs of the adult's girdle.</i> | 324 |
| 9.9 | <i>SEM-BSC micrographs of a ring from the adult's necklace.</i> | 325 |
| 9.10 | <i>Heart-scarab of king Sobekemsaf.</i> | 328 |
| 9.11 | <i>X-radiographic image of the heart-scarab of king Sobekemsaf.</i> | 328 |
| 9.12 | <i>Details of the Sobekemsaf heart-scarab.</i> | 328 |
| 9.13 | <i>Details of hieroglyphs on the Sobekemsaf heart-scarab.</i> | 329 |
| 9.14 | <i>Finger-ring with lapis lazuli scarab, EA57698: at right the inscription on the underside.</i> | 329 |
| 9.15 | <i>Details of finger-ring EA57698.</i> | 330 |
| 9.16 | <i>Details of the wire of the shank of finger-ring EA57698.</i> | 330 |
| 9.17 | <i>Spacer-bars inscribed for king Nubkheperra and queen Sobekemsaf, EA57699 and EA57700.</i> | 330 |
| 9.18 | <i>Detail of the hieroglyphs incised on underside of spacer-bar EA57699.</i> | 331 |
| 9.19 | <i>PGE inclusion at the surface of king Sobekemsaf's heart-scarab.</i> | 332 |
| 9.20 | <i>Gold jewellery in the Louvre Museum bearing the names of Ahhotep and Ahmose.</i> | 336 |
| 9.21 | <i>Details of the Seth amulets.</i> | 337 |
| 9.22 | <i>The as-cast finishing of the inner side of the signet ring bearing the name Ahhotep.</i> | 337 |
| 9.23 | <i>Details of the closing system of the cartouche-shaped box bearing the name Ahmose.</i> | 338 |
| 9.24 | <i>Details of cartouche-box bearing the name of Ahmose.</i> | 338 |
| 9.25 | <i>Details of one armband lion, showing PGE inclusions and corrosion products.</i> | 339 |
| 9.26 | <i>Details of the chased decoration and tail of one armband lion.</i> | 339 |

| | | |
|-------|---|-----|
| 9.27 | <i>Silver versus copper contents obtained for the jewellery bearing the names Ahhotep and Ahmose.</i> | 341 |
| 9.28 | <i>Silver versus copper contents obtained for Second Intermediate Period jewellery.</i> | 343 |
| 9.29 | <i>Gold jewellery from tomb 3757 at Badari and tomb 7352 at Qau.</i> | 346 |
| 9.30 | <i>Details of the mounting of crescent bead from Qau tomb 7352.</i> | 346 |
| 9.31 | <i>Details of the coiled wires from Badari tomb 3757.</i> | 347 |
| 9.32 | <i>The double tubular bead and barrel beads in the string from Badari tomb 3757.</i> | 347 |
| 9.33 | <i>Different forms of barrel beads in the string from Badari tomb 3757.</i> | 347 |
| 9.34 | <i>Some of the barrel beads from Badari tomb 3757, showing marks of wear from use.</i> | 348 |
| 9.35 | <i>Some of the quite regular small gold beads from Badari tomb 3757.</i> | 348 |
| 9.36 | <i>Details of one of the tiny Badari 3757 beads.</i> | 348 |
| 9.37 | <i>Ring and barrel beads from Qau tomb 7323, with PGE inclusions and marks of wear.</i> | 349 |
| 9.38 | <i>Unprovenanced oval gold pendant bearing the name of Kamose.</i> | 350 |
| 9.39 | <i>Details of the Kamose pendant showing the suspension ring made by rolling the gold strip.</i> | 350 |
| 9.40 | <i>Unprovenanced gold shell pendant with the cartouche of king Taa.</i> | 350 |
| 9.41 | <i>Details of the cartouche of king Taa on the gold shell pendant.</i> | 351 |
| 9.42 | <i>Details of the inscription on the Taa gold shell pendant.</i> | 351 |
| 9.43 | <i>The guidelines of the motif and the cracks in the Taa gold shell pendant.</i> | 352 |
| 9.44 | <i>Silver versus copper contents obtained for the jewellery in the Petrie Museum.</i> | 352 |
| 9.45 | <i>Silver versus copper contents obtained for the Second Intermediate Period objects analysed.</i> | 354 |
| 10.1 | <i>The gold necklace from tomb 296 at Riqqa.</i> | 364 |
| 10.2 | <i>One of the three ribbed penannular earrings from tomb 296 at Riqqa.</i> | 364 |
| 10.3 | <i>X-radiograph of the necklace and detail of the joining of the beads.</i> | 365 |
| 10.4 | <i>SEM-AEI micrographs of several beads observed in the necklace.</i> | 365 |
| 10.5 | <i>Details of the scarabs and scaraboid bead in the necklace.</i> | 365 |
| 10.6 | <i>SEM-AEI micrographs of one ribbed penannular earring.</i> | 366 |
| 10.7 | <i>Silver versus copper contents obtained for the gold items from tomb 296.</i> | 366 |
| 10.8 | <i>One of the ribbed penannular earrings from tomb 1371 at Deir el-Medina, Thebes.</i> | 371 |
| 10.9 | <i>Closing tube sheets in several ribbed penannular earrings.</i> | 371 |
| 10.10 | <i>Ribbed penannular earrings from Riqqa with V-shaped gold sheets.</i> | 372 |
| 10.11 | <i>Details of ribbed penannular earring N2084 with hollow round tubes.</i> | 373 |
| 10.12 | <i>Gold hollow penannular earrings with one round tube and PGE inclusions.</i> | 374 |
| 10.13 | <i>Penannular earring with hollow tube and suspension system.</i> | 375 |
| 10.14 | <i>X-radiography of a gold penannular earring with hollow tube.</i> | 375 |
| 10.15 | <i>Details of a penannular earring under the SEM.</i> | 376 |
| 10.16 | <i>Silver versus copper contents obtained for the gold penannular earrings analysed.</i> | 377 |
| 10.17 | <i>Silver versus copper contents for gold penannular earrings and Second Intermediate Period objects.</i> | 377 |
| 10.18 | <i>Mounting of a scarab swivelling finger-ring according to Vernier.</i> | 388 |
| 10.19 | <i>Middle Kingdom finger-ring from tomb G62 at Abydos.</i> | 389 |
| 10.20 | <i>Finger-ring EA37308, with details under the stereomicroscope.</i> | 390 |
| 10.21 | <i>Finger-ring EA2922, with lapis cylinder in gold mount.</i> | 391 |
| 10.22 | <i>Swivelling mechanism and the long wires wound around the shank of finger-ring EA2922.</i> | 391 |
| 10.23 | <i>Finger-ring EA4159, with detail of the chipped edge of the faience bezel.</i> | 392 |
| 10.24 | <i>Details of the swivelling mechanism of finger-ring EA4159.</i> | 392 |
| 10.25 | <i>The Ashburnham finger-ring with construction details.</i> | 393 |
| 10.26 | <i>The Ashburnham finger-ring: tool marks left by sharp engraving/chasing tools.</i> | 394 |
| 10.27 | <i>Finger-ring with carnelian wedjat-eye A.1883.49.8 and X-radiograph.</i> | 395 |
| 10.28 | <i>SEM-BSE details of finger-ring A.1883.49.8.</i> | 395 |
| 10.29 | <i>Finger-ring with a cat on a plinth EA54547 and X-radiograph.</i> | 396 |
| 10.30 | <i>Details of the finger-ring EA54547.</i> | 396 |
| 10.31 | <i>Finger-ring with frog and granulation A.1883.49.2 and X-radiographs.</i> | 397 |
| 10.32 | <i>Details of the finger-ring A.1883.49.2.</i> | 398 |
| 10.33 | <i>SEM-BSE detail of finger-ring A.1883.49.2.</i> | 398 |
| 10.34 | <i>SEM-AEI details of finger-ring A.1883.49.2.</i> | 399 |
| 10.35 | <i>Gold finger-ring with frog figure, Cleveland Museum of Art 1916-658.</i> | 399 |

| | | |
|-------|--|-----|
| 10.36 | <i>Finger-ring with frog and granulation EA2923.</i> | 400 |
| 10.37 | <i>SEM-BSE image of finger-ring EA2923 showing details of the granulation.</i> | 400 |
| 10.38 | <i>SEM-BSE images of bezel, end shanks and hammered wire of finger-ring EA2923.</i> | 401 |
| 10.39 | <i>Areas analysed by μPIXE on finger-ring A.1883.49.2.</i> | 401 |
| 10.40 | <i>PGE tiny silvery coloured inclusions at the surface of finger-rings A.1883.49.2 and EA2923.</i> | 403 |
| 10.41 | <i>Finger-ring AF2462, with a detail showing the thinned shank entering the bezel.</i> | 404 |
| 10.42 | <i>Detail under the SEM of the shank of finger-ring AF2462.</i> | 405 |
| 10.43 | <i>Creases visible at the surface of the coiled shank of finger-ring AF2462.</i> | 405 |
| 10.44 | <i>Finger-ring UC12689 with details of construction.</i> | 405 |
| 10.45 | <i>Finger-ring UC12683 with details of the gold pivot wire wound around the shank.</i> | 406 |
| 10.46 | <i>The tool marks of the inscription of signet ring A.1965.362.</i> | 406 |
| 10.47 | <i>Gold signet ring N747 bearing the cartouche of Horemheb.</i> | 407 |
| 10.48 | <i>Sharp linear tool marks on the bezel of finger-ring N747.</i> | 407 |
| 10.49 | <i>The small spindle soldered to the cup terminal of the shank of finger-ring N747.</i> | 408 |
| 10.50 | <i>The coiled gold wire decorating the shank of gold finger-ring N747.</i> | 408 |
| 10.51 | <i>Finger-ring in openwork wire UC58121, with details.</i> | 409 |
| 10.52 | <i>Silver versus copper contents for New Kingdom and Ahhotep's finger-rings analysed.</i> | 410 |
| 10.53 | <i>Signet finger-ring NMS A.1883.49.1 with the name of Queen Neferneferuat-en-Nefertiti.</i> | 412 |
| 10.54 | <i>Gold sequin A.1883.49.6 with detail of embossed design with piercing back to front.</i> | 412 |
| 10.55 | <i>Gold foil fragment NMS A.1883.49.15.</i> | 412 |
| 10.56 | <i>Ear-stud NMS A.1883.49.9 and its construction under X-ray.</i> | 412 |
| 10.57 | <i>Details under the SEM and stereomicroscope of ear-stud A.1883.49.9.</i> | 413 |
| 10.58 | <i>Details of beads in string A.1883.49.13, showing the modern mounting.</i> | 414 |
| 10.59 | <i>X-radiograph of the bead composition NMS A.1883.49.13.</i> | 415 |
| 10.60 | <i>SEM-AEI details of string A.1883.49.13.</i> | 415 |
| 10.61 | <i>Silver versus copper contents obtained for the Amarna Royal Tomb New Kingdom objects.</i> | 416 |
| 10.62 | <i>Wallet bead string EA14696 with X-radiographic view.</i> | 420 |
| 10.63 | <i>The pairs of holes for cords in two of the beads in string EA14696.</i> | 420 |
| 10.64 | <i>String EA14696: wallet and duck beads and large PGE inclusion.</i> | 420 |
| 10.65 | <i>Details of wallet beads in string EA14696.</i> | 421 |
| 10.66 | <i>Details of duck beads in string EA14696.</i> | 422 |
| 10.67 | <i>String EA14696: the two types of duck-shaped beads and the X-radiographic image.</i> | 422 |
| 10.68 | <i>Duck-shaped beads in string EA14696 with large hatched wings and dot-punched decoration.</i> | 423 |
| 10.69 | <i>Duck bead in string EA14696 under the SEM.</i> | 423 |
| 10.70 | <i>String EA14696: the snake's head terminal and the lotus terminal.</i> | 423 |
| 10.71 | <i>Details of the lotus terminal of string EA14696.</i> | 424 |
| 10.72 | <i>PGE inclusion in components of string EA14696.</i> | 424 |
| 10.73 | <i>Reconstructed bead and pendant necklace British Museum EA66827.</i> | 425 |
| 10.74 | <i>Details of necklace EA66827 components and X-radiography.</i> | 426 |
| 10.75 | <i>Details of drop-shaped pendant in necklace EA66827.</i> | 426 |
| 10.76 | <i>Details of inlaid nefer-shaped pendants of necklace EA66827.</i> | 427 |
| 10.77 | <i>Details of a nefer-shaped pendant, assembled like a closed box.</i> | 427 |
| 10.78 | <i>X-radiographs of a spherical bead and nasturtium seed bead.</i> | 428 |
| 10.79 | <i>SEM images of small ring beads in necklace EA66827 and diadem EA37532.</i> | 429 |
| 10.80 | <i>The group of jewellery of the Khamwaset find, Serapeum, Saqqara.</i> | 434 |
| 10.81 | <i>Details of the loop-in-loop chain E2990A.</i> | 434 |
| 10.82 | <i>Details of a nefer-shaped pendant from Sidmant tomb 406.</i> | 435 |
| 10.83 | <i>String of New Kingdom components from Madinat al-Ghurab, UC45602.</i> | 436 |
| 10.84 | <i>Details of the scorpion-shaped pendant in string UC45602.</i> | 436 |
| 10.85 | <i>The biggest scarab in string UC45602.</i> | 437 |
| 10.86 | <i>The smallest scarab in string UC45602.</i> | 437 |
| 10.87 | <i>The heavily corroded hollow metal scarab in string UC45602.</i> | 437 |
| 10.88 | <i>Gold sheet with the throne-name of king Amenhotep III (Nebmaatra), UC12323.</i> | 438 |
| 10.89 | <i>Some of the gold components of string E22658.</i> | 438 |

| | | |
|-------|---|-----|
| 10.90 | <i>Details of string E22658 showing diverse beads.</i> | 439 |
| 10.91 | <i>The variety of forms and dimensions of the tiny gold beads in string E 22658.</i> | 439 |
| 10.92 | <i>Groups of tiny beads in string E22658 of different types, dimensions and compositions.</i> | 442 |
| 10.93 | <i>Silver versus copper contents for the New Kingdom objects analysed.</i> | 443 |
| 10.94 | <i>Silver versus copper contents for New Kingdom objects.</i> | 443 |
| 11.1 | <i>The two coffins of a young woman and a child excavated at Qurna by Petrie.</i> | 450 |
| 11.2 | <i>The gold jewellery worn by the woman buried at Qurna as shown by Petrie.</i> | 450 |
| 11.3 | <i>The fastening system of the Qurna collar.</i> | 451 |
| 11.4 | <i>Details of small collar EA14693.</i> | 452 |
| 11.5 | <i>Choker of gold rings from Asasif, Thebes.</i> | 452 |
| 11.6 | <i>Details of the ring beads strung in the Asasif choker, showing one PGE inclusion.</i> | 453 |
| 11.7 | <i>Ring beads strung in the Qurna collar, with tool marks and smoothed surfaces.</i> | 453 |
| 11.8 | <i>Silver versus copper contents for Second Intermediate Period and New Kingdom base and solder alloys.</i> | 454 |
| 11.9 | <i>Silver versus copper contents for the base and solder alloys analysed in this volume.</i> | 455 |
| 11.10 | <i>Some of the irregular tiny beads in the necklace of the child buried at Qurna.</i> | 456 |
| 11.11 | <i>Some of the very regular tiny beads from Qau tomb 7923.</i> | 456 |
| 11.12 | <i>The so-called earrings of the Qurna child, under the stereomicroscope.</i> | 457 |
| 11.13 | <i>The reverse of the pectoral from Middle Kingdom tomb 124 excavated at Riqqa.</i> | 458 |
| 11.14 | <i>The beaded penannular earrings from Qurna as shown by Petrie, and with a detail.</i> | 459 |
| 11.15 | <i>One of four ribbed penannular earrings excavated in 1911 at Birabi, Thebes.</i> | 459 |
| 11.16 | <i>Early 18th Dynasty beaded penannular earring from Mandara, Dra Abu al-Naga, Thebes.</i> | 460 |
| 11.17 | <i>Pair of gold spiral rings from Asasif, Thebes.</i> | 460 |
| 11.18 | <i>Gold sheets closing the triangular tubes of the earrings from Deir el-Medina, tomb 1371.</i> | 461 |
| 11.19 | <i>Gold sheets closing the beaded tubes of the earrings from Qurna.</i> | 461 |
| 11.20 | <i>Detail of the ribbed penannular earring from Riqqa (Manchester Museum 6146).</i> | 462 |
| 11.21 | <i>Earring from Asasif and fragment from a hinged bracelet or belt from Gaza.</i> | 462 |
| 11.22 | <i>Earrings and scarab from city grave 2 at Tell Ajjul and the scarab from Qurna.</i> | 464 |
| 11.23 | <i>The group of jewellery from burial A1, Pit 1, Courtyard CC 41, Asasif, Thebes.</i> | 465 |
| 11.24 | <i>Two of the chased wallet-shaped beads in the girdle from Qurna.</i> | 466 |
| 11.25 | <i>One wallet-shaped bead and some of the barrel beads in the girdle from Qurna.</i> | 467 |
| 11.26 | <i>Barrel beads from Second Intermediate Period strings from Badari 3757 and Qau 7323.</i> | 467 |
| 11.27 | <i>The heavily worn gold mount of lapis lazuli scarab bearing the name of Ahhotep.</i> | 468 |
| 11.28 | <i>Silver versus copper contents for the Qurna jewellery with comparative data.</i> | 469 |
| 11.29 | <i>Silver versus copper contents for the Qurna jewellery and gold objects from Nubia.</i> | 470 |
| 11.30 | <i>Silver versus copper contents obtained for the Second Intermediate period jewellery.</i> | 471 |
| 11.31 | <i>Silver versus copper contents obtained for the New Kingdom jewellery.</i> | 472 |
| 11.32 | <i>Ratio Cu/Au as a function of ratio Ag/Au obtained for Qurna and New Kingdom jewellery.</i> | 473 |
| 11.33 | <i>Silver versus copper contents obtained for the Middle Kingdom jewellery.</i> | 473 |
| 11.34 | <i>Silver versus copper contents obtained for all the tiny beads analysed in this volume.</i> | 474 |

Tables

| | | |
|-----|---|------|
| 0.1 | <i>Numbers of artefacts (museum inventory numbers) analysed by site and period.</i> | xxiv |
| 1.1 | <i>List of gold minerals, after Boyle.</i> | 5 |
| 2.1 | <i>Early Egyptian gold-mining chronology, after Klemm & Klemm.</i> | 29 |
| 2.2 | <i>Types of settlement at mining and quarrying sites, after Shaw.</i> | 31 |
| 2.3 | <i>Old Kingdom Buhen material possibly related to copper-working, in the Petrie Museum.</i> | 32 |
| 2.4 | <i>Operations for obtaining copper archaeologically attested at Ayn Soukhna.</i> | 34 |
| 2.5 | <i>Inventory of the storage-vase from the Qantir workshop sector.</i> | 37 |
| 2.6 | <i>The great word-list of Amenemipet, section on artists, compared with the evidence from Qantir.</i> | 38 |
| 2.7 | <i>Manual occupations described in the Teaching of Duau Khety.</i> | 39 |
| 2.8 | <i>Different word-contexts attested for ancient Egyptian designations of artists.</i> | 40 |
| 2.9 | <i>Titles, in expedition areas, incorporating the element 'prospector/purveyor of metal ore'.</i> | 41 |

| | | |
|------|---|-----|
| 2.10 | <i>Attestations of coppersmiths in Sinai inscriptions, after Gardiner et al.</i> | 44 |
| 2.11 | <i>Attestations of named goldsmiths by object-type.</i> | 45 |
| 2.12 | <i>Middle Kingdom sources for named goldsmiths, after Ward.</i> | 46 |
| 2.13 | <i>Middle Kingdom sources for named overseers of goldsmiths, after Ward.</i> | 47 |
| 2.14 | <i>Middle Kingdom sources for named section overseers of goldsmiths, after Ward.</i> | 47 |
| 2.15 | <i>New Kingdom sources for men designated as overseers of goldsmiths.</i> | 51 |
| 2.16 | <i>New Kingdom sources for men designated as head goldsmiths.</i> | 51 |
| 2.17 | <i>Old and Middle Kingdom metalworking depictions, by date.</i> | 58 |
| 2.18 | <i>New Kingdom metalworking depictions, numbering after Drenkhahn and Prell.</i> | 59 |
| 2.19 | <i>Summary of Old and Middle Kingdom metalworking scenes, after Drenkhahn and Scheel.</i> | 61 |
| 2.20 | <i>Summary of New Kingdom metalworking scenes, after Drenkhahn.</i> | 62 |
| 2.21 | <i>Words for metal in inscriptions accompanying metalworking scenes.</i> | 62 |
| 2.22 | <i>Conversations in Old Kingdom chapel scenes, after Scheel.</i> | 64 |
| 2.23 | <i>Words spoken without replies in Old Kingdom scenes, after Scheel.</i> | 65 |
| 3.1 | <i>Jewellery types in the late Middle Kingdom.</i> | 82 |
| 6.1 | <i>Effective penetration depth of Au, Cu and Ag lines: PIXE, XRF and EDS.</i> | 135 |
| 6.2 | <i>Results obtained by SEM-EDS and μPIXE analysis of gold pendant N 1855A.</i> | 148 |
| 6.3 | <i>Results obtained using handheld XRF for three gold beads from string UC26275</i> | 152 |
| 6.4a | <i>Depth of analysis calculated for four typical Egyptian gold alloys at our experimental conditions.</i> | 156 |
| 6.4b | <i>Depth of analysis calculated for four typical PGE inclusions at our experimental conditions.</i> | 156 |
| 6.5 | <i>Results obtained for selected areas from centre to rim of the biggest PGE inclusion.</i> | 156 |
| 6.6 | <i>Results obtained for the PGE inclusion and the gold alloy.</i> | 157 |
| 6.7 | <i>Results obtained for the PGE inclusions, hard solder alloy and base alloy.</i> | 157 |
| 6.8 | <i>Qualitative comparison of 3D representations.</i> | 168 |
| 6.9 | <i>List of the objects studied, with their identification, accession number, and collection.</i> | 178 |
| 6.10 | <i>Results obtained by μPIXE, SEM-EDS and μXRF for the studied objects.</i> | 180 |
| 6.11 | <i>Results obtained for the three layers in the blue corroded area of fragment 2.6.</i> | 181 |
| 6.12 | <i>Results obtained for the base alloy and corrosion layer of foil fragment 2.4.</i> | 181 |
| 7.1 | <i>Results obtained for the composition of diadem from Abydos tomb 1730.</i> | 205 |
| 7.2 | <i>Data published by Gale & Gale and Payne for Predynastic items.</i> | 206 |
| 7.3 | <i>Composition of foils UC35689, gold beads in string UC36517 and comparators.</i> | 209 |
| 7.4 | <i>Hypothetical native gold alloys and artificial silver alloy.</i> | 212 |
| 7.5 | <i>First Intermediate Period jewellery analysed in this chapter.</i> | 215 |
| 7.6 | <i>Results obtained for the jewellery from tomb 7923 at Qau and tomb 3053 at Matmar.</i> | 230 |
| 7.7 | <i>Results obtained by SEM-EDS for the small beads analysed.</i> | 233 |
| 7.8 | <i>Results obtained by XRF for the amulets analysed.</i> | 235 |
| 7.9 | <i>Results obtained by XRF for the beads analysed (excluding the smaller ones).</i> | 238 |
| 8.1 | <i>Results obtained by XRF and μPIXE for the Haraga tomb 72 necklaces and scarab.</i> | 257 |
| 8.2 | <i>Results obtained by XRF and μPIXE for the Haraga pendants.</i> | 258 |
| 8.3 | <i>Results obtained by SEM-EDS for the PGE inclusions analysed in the Haraga jewellery.</i> | 258 |
| 8.4 | <i>Elements visible in the spectra obtained by SEM-EDS for inlays from the Riqqa pectoral.</i> | 264 |
| 8.5 | <i>Results obtained for the different components of the jewellery from Riqqa tomb 124.</i> | 265 |
| 8.6 | <i>Results obtained for one cell plate and adjacent solder alloy in the Riqqa pectoral.</i> | 266 |
| 8.7 | <i>Results obtained for PGE inclusions in Riqqa tomb 124 pendant and pectoral.</i> | 266 |
| 8.8 | <i>Results obtained for the gold scraps and jewellery from excavation at Haraga.</i> | 274 |
| 8.9 | <i>Results obtained for the gold scraps and jewellery from excavation at Lahun.</i> | 276 |
| 8.10 | <i>Results obtained for the jewellery from excavations at Naqada and Buhen.</i> | 276 |
| 8.11 | <i>Results obtained for the components of the Haraga 211 cylinder amulet.</i> | 283 |
| 8.12 | <i>Results obtained for the granules and solders of the Haraga 211 cylinder amulet.</i> | 285 |
| 8.13 | <i>Results obtained by SEM-EDS for the foils and jewellery from excavations at Abydos.</i> | 292 |
| 8.14 | <i>Results obtained for Middle Kingdom gold objects in the collection of the Petrie Museum.</i> | 300 |
| 8.15 | <i>Results obtained by SEM-EDS for necklace EA3077.</i> | 307 |
| 9.1 | <i>Results obtained for the Qurna jewellery using several techniques.</i> | 320 |
| 9.2 | <i>Results obtained by SEM-EDS for PGE inclusions in the Qurna jewellery.</i> | 322 |

| | | |
|-------|--|-----|
| 9.3 | <i>Results obtained for the joining areas in the Qurna jewellery.</i> | 325 |
| 9.4 | <i>Results obtained by XRF and SEM-EDS for the heart-scarab of king Sobekemsaf.</i> | 331 |
| 9.5 | <i>Results obtained by XRF and SEM-EDS for finger-ring EA57698.</i> | 331 |
| 9.6 | <i>Results obtained by XRF for spacer-bars EA57699 and EA57700.</i> | 332 |
| 9.7 | <i>Results obtained by SEM-EDS for PGE inclusions.</i> | 332 |
| 9.8 | <i>Results obtained for the jewellery bearing the names of Ahhotep and Ahmose.</i> | 340 |
| 9.9 | <i>Results obtained for the joins and base alloys of armband E7168 and scarab E3297.</i> | 341 |
| 9.10 | <i>Results obtained for PGE inclusions in the objects bearing the names of Ahhotep and Ahmose.</i> | 342 |
| 9.11 | <i>Results obtained for objects from several excavations and bearing king names.</i> | 353 |
| 10.1 | <i>Results obtained for the base and the solder alloys for Riqqa tomb 296 jewellery.</i> | 367 |
| 10.2 | <i>Results obtained for the PGE inclusions in the jewellery from tomb 296 at Riqqa.</i> | 368 |
| 10.3 | <i>Results obtained and published for penannular earrings.</i> | 378 |
| 10.4 | <i>Results obtained for the PGE inclusions in the earrings studied.</i> | 380 |
| 10.5 | <i>Information on the ribbed penannular earrings with triangular hoops considered.</i> | 382 |
| 10.6 | <i>Results obtained for the finger-rings in the collection of the British Museum.</i> | 394 |
| 10.7 | <i>Results obtained for finger-rings in the NMS and British Museum collections.</i> | 402 |
| 10.8 | <i>Results obtained for the PGE inclusions in the NMS finger-rings.</i> | 403 |
| 10.9 | <i>Results obtained for the finger-rings in the Louvre Museum, Petrie Museum and NMS.</i> | 409 |
| 10.10 | <i>Results obtained for the New Kingdom objects associated with the Royal Tomb at El-'Amarna.</i> | 414 |
| 10.11 | <i>Results obtained for the two strings in the British Museum.</i> | 430 |
| 10.12 | <i>Results obtained for the small ring beads in necklace EA66827.</i> | 430 |
| 10.13 | <i>Results obtained for New Kingdom objects in the Louvre Museum and the Petrie Museum.</i> | 440 |
| 10.14 | <i>Results obtained by SEM-EDS for the different components of string E22658.</i> | 440 |

Editorial foreword

This volume aims to present a wide range of perspectives on early Egyptian goldwork, integrating the complementary yet distinct approaches of archaeology, materials science, jewellery and Egyptology. On one level, our primary task has been to present new analytical data on the manufacturing technology and elemental composition of dozens of artefacts preserved at six European museums. At the same time, we have sought to anchor and contextualize this new information based on current research from three perspectives: an introduction to the fundamental geochemistry and material properties of gold, a reanalysis of historical sources and of goldwork manufacturing-techniques, and a guide to the key analytical techniques employed. In this way, we wish to ensure that the volume is accessible to specialists and students from different backgrounds. We anticipate that this body of material will provide a rich source of information for further interrogation and discussion in the future, and our concluding chapter offers a first synthesis of some key points emerging from this new research. There we focus particularly on the findings that seem to us most significant, alongside open questions and suggestions for future work. In so doing, we explicitly highlight some of the many strands beyond the scope of the work presented here, hoping that they may provide pointers for others. We emphasize that the volume is addressed not only to those interested in the archaeology of Egypt in the timespan covered, but equally to scholars researching past technologies and archaeological goldwork elsewhere, who may find technical observations of broader scope that could prompt cross-cultural comparisons.

In spite of the substantial amount of data compiled here for the first time, it is important to remind ourselves of some potential biases that are inherent to this work and may thus skew our interpretations. The most important of these concerns the selection of

objects. This project starts and, in many ways, remains throughout its course with the exceptional group of gold jewellery buried in Qurna, on the west bank of Thebes in Upper Egypt, with a woman and child whose names are unknown to us, at some point in the 17th or 16th century BC. Today the Qurna group is the most important Egyptian assemblage in the National Museum of Scotland, Edinburgh. In 2008, curator Bill Manley with materials scientists Jim Tate, Lore Troalen and Maria Filomena Guerra launched a programme of new analyses of the goldwork from the group. Already in this first investigation, the scope extended to comparison with jewellery from the preceding and following centuries (Tate et al. 2009; Troalen et al. 2009). With funding obtained from the CNRS, Guerra could then expand the range of collections involved in collaboration with Thilo Rehren at UCL, to include the UCL Petrie Museum of Egyptian Archaeology and the UCL Institute of Archaeology with its laboratory facilities, as well as the National Museums of Scotland and the British Museum as project partners (CNRS project PICS 5995 EBAJ-Au). On the initiative of Jim Tate, contact had been established already with colleagues Matthew Ponting and Ian Shaw at the University of Liverpool. As a result, the Garstang Museum is also participant in the wider project, together with the Manchester Museum, through the support of curator Campbell Price, and the Louvre Museum, through the support of curator H el ene Guichard and the late Sandrine Pag es-Camagna, material scientist at C2RMF (Centre de Recherche et de Restauration des Mus ees de France). We wish to emphasize here the fundamental role of Sandrine Pag es-Camagna in crucial stages of the project; without her participation the project could not have achieved a significant part of its aims – notably comparison between the Qurna group and the nearest securely dated examples of royal goldwork from the reigns of kings Kamose and Ahmose.

Other institutions participated with the provision of access to particularly specialized equipment: AGLAE facilities at C2RMF, Bundesanstalt für Materialforschung und –prüfung, and LIBPhys at NOVA University of Lisbon

With this new support, the research agenda was able to grow organically, adapting to fresh questions emerging from preliminary results, while contingent on the artefacts present in museums that were accessible to the project. Indeed, the history of the collections has been a significant factor, both enabling and constraining our research. The Louvre collections contain a range of jewellery from early excavations in Thebes, including representative material from the late second millennium BC settlement Deir al-Madina, and major works from 16th century royal burials uncovered during fieldwork directed by Auguste Mariette. The British Museum and the other participating museums in England and Scotland also preserve a mixture of material from documented excavations and earlier undocumented collecting practice. Here colonial history frames the kinds of material available. During and after the full British military occupation of Egypt (1882–1922), the Antiquities Service of Egypt under French Directors permitted officially recognized institutions to excavate in Egypt and, in return for the enrichment of the Egyptian Museum Cairo, to take a share of finds from excavations. Following division of finds in Egypt, excavation funding bodies based at Liverpool (since 1903) and London (since 1882) distributed finds to dozens of sponsoring museums (Stevenson 2019). The university museums in Liverpool and London were among the major recipients

of these finds, and also hold substantial excavation archives. The Qurna group itself and several other sets of jewellery analysed during the project are unusual examples of this pattern of dispersal, where the vast majority of items distributed belonged to the types of objects found in large numbers in fieldwork. The project was therefore able to investigate objects from a wide social spectrum, from palace production (Qurna group, Haraga fish and cylinder, items of kings Ahmose and Kamose from Thebes) to finds in cemeteries of regional rural towns and villages (Qau, Badari, Matmar). At the same time, in expanding the chronological scope of analyses forwards to the New Kingdom and back to the late prehistory of Egypt, the participating museums could not cover every social group for every period. Most notably, and perhaps surprisingly for those outside the museum circle, these collections hold none of the major goldwork from the age of the great pyramids, the mid-third millennium BC. At that period, the concentration of power at Memphis around kingship separates the royal court from the regions, and this is reflected in the tombs of the period and in the distribution of finds. Gold and gilt ornaments are more prominent in burials at the Memphite cemeteries: Giza and Saqqara. The single outstanding assemblage of Egyptian goldwork from the mid-third millennium BC is the unparalleled burial of material related to Hetepheres, mother of king Khufu; the finds are on display in the Egyptian Museum Cairo. Egyptologists from Cairo, Vienna, Boston, Hildesheim and Leipzig directed excavations at Giza; their museums received a share in finds (Manuelian 1999). The museums in our project, from Paris to Edinburgh,

Table 0.1. Numbers of artefacts (museum inventory numbers) analysed by site and period.

| | Dyn 1-2 | First IP | Middle Kingdom | Second IP(-Dyn18) | New Kingdom | ? | Total |
|--------------|----------|-----------|----------------|-------------------|-------------|----------|------------|
| Memphis | | | | | 2 | | 2 |
| Riqqa | | | 4 | | 7 | | 11 |
| Haraga | | | 13 + 1? | | | | 14 |
| Lahun | | | 5 | | | | 5 |
| Ghurab | | | | | 1 | | 1 |
| Sidmant | | | 1 | | 1 | | 2 |
| Amarna | | | | | 8 | | 8 |
| Qau area | | 15 | | 5 | | | 20 |
| Abydos | 4 | | 2 + 2? | 2 | | 3 | 13 |
| Naqada | | | 2 | | | | 2 |
| Thebes | | | 2 | 2 + 7? | 4 | | 15 |
| *Qurna | | | | 12 | | | 12 |
| Buhen | | | 1 | | | | 1 |
| ? | | 1 | 5 | 2 | 22 | | 30 |
| TOTAL | 4 | 16 | 36 | 30 | 45 | 3 | 136 |

are not on that distribution map. With this and other lesser gaps, our sample, however extensive, cannot and does not claim to be random or representative of an underlying population of 'Egyptian goldwork'. On our chronological range from fourth to second millennia BC, there are peaks and troughs in the frequency of artefacts, and we encourage the reader to keep these in mind graphically, in order to assess our interpretations in context and to develop their own further research agendas (see Table 0.1).

Another delimiting factor in the selection of objects derives from our focus on technique, directing our attention predominantly to jewellery, rather than other gold elements such as the prominent use of sheets for gilding larger substrates of wood or plaster. Gold foils were included for comparative purposes, particularly in the investigation of composition, but to a lesser extent. Furthermore, within the rich repertoire of Egyptian gold jewellery, we took a particular interest in select assemblages, starting with the Qurna group itself, and within these certain specific features, such as the small beads found in the child's coffin and the adult's girdle. While these are fascinating manifestations of both technology and consumption, they are not necessarily representative of a broader corpus. We would also emphasize that we sought primarily artefacts with well-recorded archaeological contexts, as these evidently allow for more robust inferences, and provide the most secure foundations on which to build further research. Where the museums could provide access to material not from documented excavations, but acquired before 1970, we have included certain items if they helped to complete gaps in understanding, as a secondary circle of supplementary information. In each such case we have done our utmost to investigate their authenticity and source, but undeniably any interpretation based on an unprovenanced object will have to remain tentative. Indeed, one of our analytical investigations demonstrated the risks in building historical conclusions on material without documented

excavation context; a gold shell inscribed with the name of king Taa, who reigned close in time to the Qurna group, presents disconcerting features more consistent with modern rather than with ancient manufacture.

A final and equally important constraint concerns the background and expertise of the editors and contributors to this volume. While together we span interdisciplinary breadth, and have found synergies in our research, inevitably there remain areas beyond our interests and access, and indeed beyond the time scope of the project. For example, our data may be used as a starting point to address issues of provenance, but targeted consideration of the extraction methods and possible geological sources of gold is not addressed in detail in this volume. Instead, much more emphasis has been placed on issues of technology, and the application of the results to a concluding interpretation of the Qurna group. We look forward to seeing how others may take up such topics, and feel sure that the woman and child of Qurna will continue to pose new questions.

Finally, for the opportunity to share our discussions and findings with a wider research audience, we would like to express our gratitude to the McDonald Institute for Archaeological Research for including this volume in its series.

References

- Manuelian, P. Der, 1999. Excavating the Old Kingdom. The Giza necropolis and other mastaba fields. In *Egyptian Art in the Age of the Pyramids*, ed. D. Arnold. New York: Metropolitan Museum of Art, 139–53.
- Stevenson, A., 2019. *Scattered Finds. Archaeology, Egyptology and Museums*. London: UCL Press.
- Tate, J., Eremin, K., Troalen, L.G., Guerra, M.F., Goring, E. & Manley, W.P., 2009. The 17th Dynasty gold necklace from Qurneh, Egypt. *ArcheoSciences* 33, 121–8.
- Troalen, L., Guerra, M.F., Manley, W.P. & Tate, J., 2009. Technological Study of Gold Jewellery from the 17th and 18th Dynasties in Egypt. *ArcheoSciences* 33, 111–19.

Chapter 6

Analytical approaches to Egyptian goldwork

Maria F. Guerra, Mona Hess, Quentin Lemasson,
Lindsay MacDonald, Marcos Martín-Torres, Nigel Meeks,
Brice Moignard, Claire Pacheco, Laurent Pichon,
Martin Radtke, Uwe Reinholz†, Isabel Tissot & Lore Troalen

The structure and composition of ancient gold objects retain information about their long history of manufacture, from the exploitation of the ore to the finishing touches, as well as evidence of their use, deposition, and degradation. By developing an efficient analytical strategy, it is possible to retrieve that information. This chapter sets the necessary foundation

to explore fully the analytical results presented in the following chapters of this volume. The techniques employed in the analyses of the Egyptian jewellery are described and the analytical parameters provided. For more established techniques, only brief introductions are presented, while more recent developments are presented in greater detail.

Chapter 6.1

Analysing gold jewellery

Maria F. Guerra

Ancient gold objects are commonly made from gold alloys containing variable amounts of silver and copper. These objects may be decorated with parts made from other metals or alloys, and might be enhanced by addition of other materials that enrich their appearance. Like any other object made in the past, those made from gold alloys retain in their structure and composition information about their long history of manufacture, from the exploitation of the ore to the finishing touches. They contain as well evidence on their use, abandonment, deposition, and degradation. By developing an analytical strategy based on the many analytical techniques nowadays available, it is possible to retrieve that information. The aim of this chapter is to provide the necessary basis to explore fully the following chapters of this volume, where we present the analytical results obtained for the Egyptian items studied.

As questions on ancient gold objects cover several scientific areas – metallurgy, physics, chemistry, etc. – the development of an efficient analytical protocol requires a clear definition of the enquiry. When developing this protocol, we need to consider several particularities of goldwork, such as how the object was made, what its function was, and what its state of conservation is. The importance of the workshops' practices and their chronological and territorial spread make the understanding of the steps of construction of an object fundamental. The technologies employed by the goldsmiths may be partially characterized by using specific techniques of examination. These techniques consist of the observation of the morphology and structure at several depths and scales by using different lights and radiations. Thus examination can provide, for instance, information on the goldsmith's skilled work of mounting, decorating and finishing. In addition to a 2D image of an object, for example a macrophotography or a detailed image under the

stereomicroscope, a realistic 3D image of a gold item can encompass much information on its manufacture and function. The high reflectance of gold, however, renders the simulation of the appearance of the original object difficult. Therefore, the choice of the method of 3D acquisition is fundamental. While the Egyptian gold jewellery analysed in this volume was regularly documented at several magnifications by using macrophotography, optical microscopy and scanning electron microscopy (SEM), Chapter 6.7 explores the capability of 3D image acquisition to represent the colour and surface details of materials used in the production of the jewellery.

Detailed observation of goldwork involves description of the manufacturing details. These features can be observed on the object surface by optical microscopy using white light, or in the internal structure by radiography using, in general, incident X-rays. Some examples of the application of optical microscopy and radiography to the study of Egyptian jewellery included in this volume are discussed in Chapter 6.2. The objects were also regularly documented by using SEM, a technique that provides images of the object surface at higher magnification and resolution. When imaging with secondary (SE) or backscattered (BSE) electrons, it is possible to obtain, respectively, topographic or chemical contrast. This technique has in addition a major advantage: it is frequently equipped with an EDS (energy dispersive spectrometry) system (SEM-EDS), combining studies on morphology with elemental analysis. SEM-EDS is commonly used in the study of gold jewellery, as discussed in Chapter 6.3. When higher resolution images are necessary, such as when studying the corrosion mechanisms of gold alloys, it is possible to use a SEM equipment with a field emission gun (FEG). As discussed in Chapter 6.8, the atmospheric corrosion of Egyptian gold objects results on the development of corrosion compounds

contained in a very thin surface layer, in general thinner than 1 μm (Tissot et al. 2015, 2019). Although not used in this volume, other SEM-based configurations are available, such as SEM-EBDS (electron backscatter diffraction), used to perform microstructural characterization, and FIB-SEM (focused ion beam), which uses a focused beam of electrons to image the sample and a focused beam of ions for successive removal of very thin layers (local sputtering).

Documentation of the object surface and manufacture is necessary to define the analytical protocol to be applied when searching for the materials composition. This step in the analytical protocol avoids misinterpretation of data obtained in certain regions of analysis, which might result in an incorrect characterization of the object. A common example is the analysis of a joining region. In a gold object the same elements (Au, Ag and Cu) are frequently present in the base alloys and in the solder alloys, but the composition of an area containing hard soldered joints is not necessarily representative of the whole object. If a hard soldered joint is present, it will normally contain different levels of Cu and sometimes Ag than the base alloy, because the solder is a gold alloy with lower melting point.

In general, analytical techniques applied to the study of gold jewellery are of three types: elemental, isotopic and structural. When applying these techniques to the study of goldwork, the first are of very broad applicability, the second provide essentially information on the origin and circulation of the materials, and the latter are in general applied to the study of the decorative materials and of the naturally or artificially modified surfaces. Therefore, the choice of the types of techniques included in the analytical protocol is an essential stage, as it will dictate the type of data obtained and hence the questions we can address.

While each broad type of analytical technique provides a particular kind of information about the object, each specific technique included in each category has particular characteristics. For example, in the above-mentioned situation of the analysis of a hard solder joint, it can be adequately probed by using X-ray Fluorescence Analysis (XRF) only when the appropriate equipment is used. When using handheld XRF, with a spot of several millimetres, the spatial resolution is not sufficient to analyse the majority of the joining areas only, which are much smaller. In this case, the results obtained provide an average composition of both the base alloy and the hard solder. When XRF equipment with polycapillary focusing optics (μXRF) is used, the excitation beam is reduced to a small spot, down to tens of micrometres, permitting scanning the region of interest. Distribution maps of the elements present

can then be constructed, which chemically separate the two zones and thus provide the elemental composition (or at least an estimation) of both the hard solder alloy and the gold base alloy in the parts being joined. The important role played by SEM-EDS in this case should be highlighted. EDS element maps can be constructed with very high spatial resolution and low effective penetration depth.

The technical performance parameters that play an important role when studying goldwork are typically, in addition to spatial resolution, the depth of analysis, the limits of detection and the portability (Guerra 2008, 2018). Techniques providing accurate depth profiling are essential when defining the analytical protocol. According to the question, the effective penetration depth must be low for surface analysis and high for bulk analysis. Conversely, when searching for the gold origin and trade routes it is necessary to use techniques with very good detection limits for certain trace elements or to measure isotope ratios, in order to be able to link the object to a source of metal. The provenance and circulation of objects and materials can only be efficiently defined this way, but because gold objects are rare, small and precious, the employed techniques must be entirely non-destructive. Isotopic analysis, because it typically requires a sample, is only occasionally employed in the study of goldwork (Standish et al. 2015; Jansen et al. 2021).

Finally, instrument portability is often a necessary requirement when analysing goldwork held at museums, and this constrains the questions that can be addressed. For example, in addition to limited detection limits and spatial resolution, mobile techniques only occasionally provide effective element maps. Indeed, and in spite of the availability of benchtop SEM technology, (with however small sample chamber and low accelerating voltage), only mobile XRF systems, a few systems with polycapillary optics, or handheld XRF can easily be moved for *in situ* analysis of the gold objects. Another possible handheld technique is LIBS (Laser-Induced Breakdown Spectroscopy), which uses laser ablation. LIBS has better detection limits than XRF for low atomic number elements, which is not the case of gold matrices, but offers depth profiling, important when analysing, for example, chemically modified surfaces. When jewellery contain components in other materials, techniques such as Raman spectrometry, offering portable equipment, provide additional information.

When analysing gold jewellery, the development of an analytical protocol is a 'wise' combination of the most appropriate techniques and those that can be adopted according to the situation. Chapter 6 will not discuss in detail the difficulties faced by

Table 6.1. Effective penetration depth in μm calculated for the Au L α line, the Cu K α line and the Ag K α line for PIXE and XRF and Ag L α line for EDS in the case of four gold alloys containing different amounts of silver and copper, based on Troalen et al. (2014) and Troalen & Guerra (2016) (see also Chapter 6.5).

| Alloy (wt%) | (μm) | | | | | | | | |
|-------------|-----------------|------|-----|------|------|------|------|------|------|
| | PIXE | | | XRF | | | EDS | | |
| Au–Ag–Cu | Au | Ag | Cu | Au | Ag | Cu | Au | Ag | Cu |
| 95.8–4–0.2 | 7.4 | 11.1 | 5.1 | 12.7 | 27.8 | 7.9 | 0.5 | 0.5 | 0.5 |
| 86–12–2 | 7.9 | 12.1 | 5.5 | 13.5 | 32.4 | 8.6 | 0.45 | 0.45 | 0.45 |
| 68–30–2 | 8.8 | 14.0 | 6.1 | 15.2 | 43.1 | 9.8 | 0.6 | 0.6 | 0.5 |
| 50–48–2 | 9.6 | 15.8 | 6.8 | 17.0 | 60.0 | 10.8 | 0.6 | 0.6 | 0.6 |

the analyst when analysing ancient goldwork, or every challenging angle of the science-based study of goldwork. An analytical protocol must take into account several aspects of the gold objects, including the steps of production, the identification of marks of function, marks of use and reuse, and signs of disclaim and degradation, first in the burial context and then in the museum context (atmospheric corrosion). The choice of the analytical protocols used in this volume was based on the different possibilities that opened to us when studying each collection, and by focusing on particular questions mostly related to the objects construction and the type of gold used (alluvial gold or reef gold). Non-destructive techniques that can be moved to the museums were prioritized. For this reason, optical microscopy was the main observation technique applied in this study, even if in a few cases X-radiography, SEM and 3D imaging allowed us to complete the object's observation.

The majority of the items were analysed by XRF for the composition of the alloys. The use of small and portable equipment is often a good option, because it provides some flexibility with low costs. The analytical data obtained by XRF was as much as possible complemented for the joins and small parts of the objects (wires, cloison, granules, etc.) by using SEM-EDS. Nevertheless, we had also the opportunity to apply to the study of a few items the latest PIXE methodology (Particle Induced X-ray Emission) developed at the AGLAE accelerator, in Paris, to construct element maps. This development is discussed in Chapter 6.5. PIXE, with good spatial resolution when using a μbeam , is based on X-ray spectrometry (using the same physical phenomena as XRF), but the photon beam of

the XRF systems is replaced here by an incident micro beam of protons. Table 6.1 (from Troalen et al. 2014) compares the effective penetration depth for XRF, PIXE and EDS in the case of gold alloys typically employed in the manufacture of Egyptian jewellery. This parameter depends on several characteristics, such as the type and energy of the incident beam, the atomic number of the element analysed and the X-ray line used in the calculation; in Table 6.1 our experimental conditions are detailed.

In addition to advantages related to the quantification of the detected chemical elements, PIXE attains better detection limits than XRF for elements in gold alloys, a high atomic number matrix. Therefore, mapping minor and trace elements becomes possible. However, even when using specific filters (Guerra 2004, 2008) the detection limits attained in the case of gold matrices constrain the analysis of some important trace elements (Guerra et al. 2008). Among these are the platinum-group elements (PGE). For gold jewellery containing PGE inclusions, PIXE element maps allow an accurate determination of the composition at different depths of the mapped inclusions, as discussed in Chapter 6.5, but PIXE is not appropriate to search for low PGE amounts in a gold matrix. Therefore, the use of synchrotron radiation (SR) to determine low contents of PGE in gold alloys, namely using SRXRF was considered for particular items that could be sampled. SRXRF, which uses focused monochromatic beams, is also based on X-ray spectrometry. The use of SR very much improves the detection limits of elements present in gold alloys (Guerra 2021), particularly when associated to wavelength-dispersive X-ray spectrometry (WDS), replacing the more conventional EDS configuration. In our case, D²XRF was improved to search PGE amounts in the particular case of thin gold fragment sheets. The results obtained are discussed in Chapter 6.6.

The different sections of Chapter 6 introduce the techniques mentioned and the analytical parameters employed in the analyses of the Egyptian jewellery. For more established techniques, only brief introductions are presented, with a few examples of applications, but the more recent instrumental developments are presented in greater detail.

References

For references see pp.185–91 at the end of this chapter.

Chapter 6.2

Goldwork under white light and X-rays: inferring technologies

Lore Troalen & Maria F. Guerra

By examining jewellery with increased magnification, small details can be revealed which contribute to the understanding of the objects construction, or which provide information on their use-wear and function.

Optical microscopy allows detailed visual examination of the objects under white light (Bass 2010). In the case of jewellery, transmitted light cannot be used to observe the metallic parts, although information can be gained for precious stone inserts. The observation of jewellery is best carried out under a stereomicroscope; the incident light reflected from the metallic surfaces is split and focused through two eyepieces to allow comfortable viewing with both eyes. The major problem of this technique is the high optical reflectivity of gold alloys, for wavelengths higher than 500 nm it is close to that of aluminium (Fearon et al. 2007; Blaber et al. 2010). To overcome this problem, examination of the metallic surfaces can be carried out by scanning electron microscopy (SEM), discussed in Chapter 6.3. The visual images obtained from the interaction of an electron beam with the object, in topographical or in atomic number contrast modes and over a very high range of magnifications, do not suffer from the same reflectivity problems.

Stereomicroscopes can attain high magnification. However, most of the details related to the construction of jewellery items can generally be most usefully examined under magnifications of up to $\times 100$. An alternative is to use an inspection system with high quality optics, which provides a digital image directly to a computer display via a USB connection and which is easily moved to museums (Fig. 6.1). Many of them attain magnifications equivalent to common stereomicroscopes and provide good resolution images (Guerra & Rehren 2009). One example of stereomicroscope imaging is provided in Figure 6.2, where a detail of the wire from a Roman Period earring (NMS A.1883.49.5), shows the morphology corresponding to

the manufacture of the wire using the strip-twisting technique (Oddy 1977, 2004).

It is often necessary to use a combination of optical microscopy with white light and radiography to fully understand the various aspects of jewellery manufacturing (Borel 1995). Radiography provides an insight into the internal structure of an object (Lang & Middleton 2005), revealing details of manufacture that



Figure 6.1. Working at the Petrie Museum with the compact high-resolution Flexia video microscope from Optilia with a colour 5.0 MP CMOS image sensor (2592×1944), a zoom reaching $\times 100$, a built-in LED illumination and a Bersoft image measurement software.



Figure 6.2. Details under the stereomicroscope of a strip-twisted wire in a Roman Period earring (NMS A.1883.49.5) showing the helical seam and the hollow interior.

cannot be seen by direct observation of the objects. In the case of metals, radiography can additionally reveal the development of internal deterioration processes that do not feature on the surface. Some construction details can be revealed by radiography. For example, it is possible to describe the manufacture of a bracelet dated to the Roman Period (NMS A.1883.49.4), made using three thick gold hoops twisted and with the ends decorated with coiled wires (Fig. 6.3a). X-ray imaging revealed that the bracelet is made of twisted hollow tubes and that the coiled wires are additional and probably soldered to the terminal ends (Fig. 6.3b). Thiaudière (2005) provides more details on the manufacture of this type of bracelets.

Radiographic images are obtained by exposure of an object to, most commonly, X-rays generated by

an X-ray tube. When X-rays are used, the technique is named X-radiography, but other sources of radiation with different penetration depths in one material and higher intensity can be used to radiograph an object, such as gamma-rays (gamma-rays imaging),

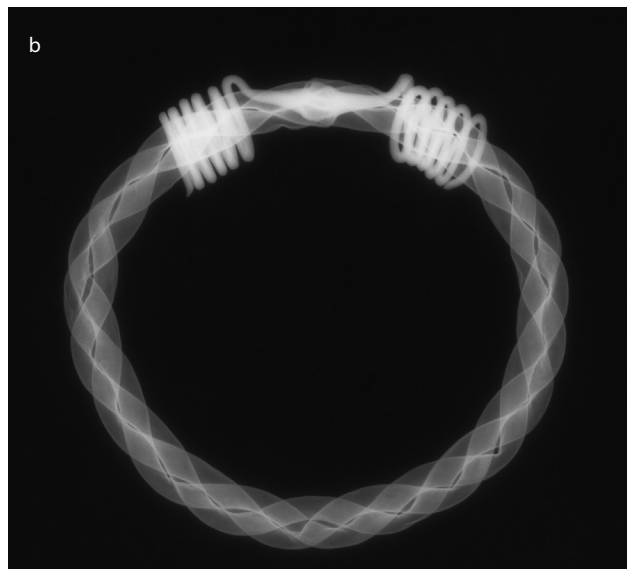


Figure 6.3. (a) Bracelet (NMS A.1883.49.4 A) dated to the Roman Period and (b) X-radiograph of its pair (NMS A.1883.49.4) revealing the coiled hollow tubes with the addition of a coiled wire, soldered to each of the terminal ends. X-ray conditions were 3 minutes exposition at 300 kV, 4 mA, with a filtration of 1.3 mm brass, 1.4 mm copper and 0.5 mm lead at a working distance of 1 m, with Agfa Structurix D7 film and 0.125 mm lead screen intensifier (Plate 20091009-1).

synchrotron radiation (SR radiography), electrons (beta-ray imaging), and neutrons (neutron radiography). Each technique is based on radiation that interacts in a different way with the metallic structure, and in the case of neutron radiography, the neutron beam will interact with the nuclei and therefore provide different, often complementary, information to X-radiography (Casali 2006).

In a conventional configuration, one X-ray sensitive film (analogue system) or one phosphor photo-sensitive plate (in the first case for direct viewing after chemical processing and in the second to be read digitally) are used to collect the image. They are placed under the object to collect the transmitted X-rays. Digital systems are easier to use because analogue systems using photographic films require chemical development processing. In transmission mode, the incident X-ray beam loses energy during its path in the material, the amount of attenuation leading to the 2D-images, which are the projection of the 3D object.

More complex systems such as computed tomography (CT) produce a point cloud of depth-sensitive data which is used to create a pseudo 3D-image of the object (Morigi et al. 2010). Where very small features need to be imaged, a micro-focus X-ray tube with a small focal spot (*c.* 50 μm voxel size) may be used to provide the best resolution (Freeth et al. 2006; Troalen et al. 2010).

The 2D images from radiography show variations in contrast because X-ray mass attenuation and energy absorption coefficients increase with the atomic number of the materials. In the images of an object of uniform thickness but variable chemical composition, the darkest areas correspond to the most intense flux of radiation reaching the detector and thus to the areas where composition has the lowest atomic numbers (Barham 2007). X-radiography can therefore provide information on gold sheet thicknesses when the composition is uniform; and on the variation in alloy composition when the thickness is constant. To illustrate this, the X-radiography in Figure 6.4 of a

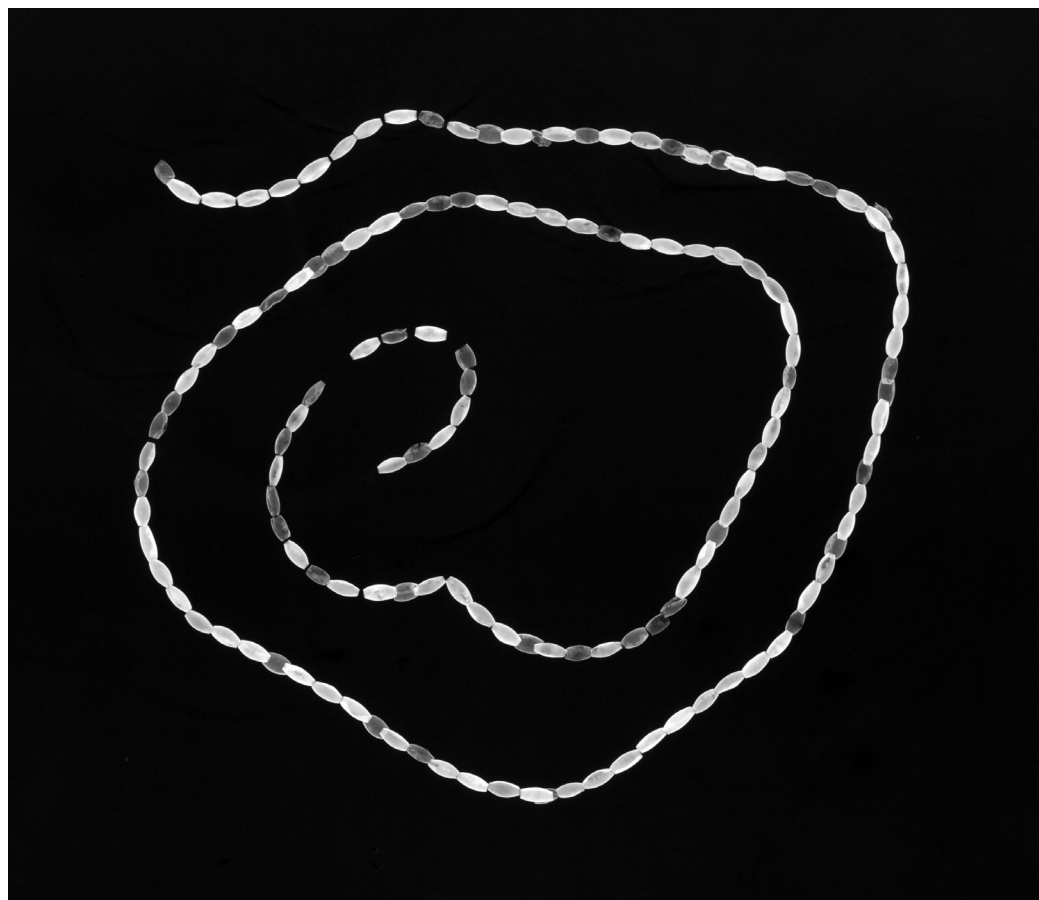


Figure 6.4. X-radiograph showing variable densities of gold foils used in a string of beads from Haraga, tomb 72 (NMS A.1914.1092). X-ray conditions were 1.5 minutes exposition at 90 kV at working distance of 1 m, using Agfa Structurix Film D7 with 0.125 mm lead screen intensifiers (Plate 20100419-10).

string of biconical gold beads from tomb 72 at Haraga (see Chapter 8.2), displays some contrasts between the beads that are explained predominantly by composition differences. The elemental analysis of this group of strung beads showed that the gold beads are made of alloys containing variable silver contents (see Table 8.1 in Chapter 8.2). It is of course possible that different alloys might have been hammered out at variable thicknesses; however, given the equivalent typology of the beads, it is more likely that the variable opacities observed on the X-ray plate relate to the composition of the gold alloys.

One of the greatest difficulties comes from very dense materials. High atomic number and significant thickness of metal highly reduce the X-ray penetration. Although gold has a very high density (19320 kg/m³, compared to aluminium 2712 kg/m³ and even to lead 11341 kg/m³), when the correct exposure factors and parameters are used, images may still be obtained for some objects which provide useful information about their construction. Many factors contribute to the quality of an X-radiograph, such as the energy, intensity and monochromacy of the incident X-ray beam as well as the positioning of both the object and the detector related to the incident beam and the exposure time (Borel 1995; Lang & Middleton 2005; Kodak 1966).

In addition to these parameters, the type of film will greatly affect the resolution and contrast of the X-radiograph. It is necessary to use films with ultra-fine to fine grains to achieve high contrast radiography, although today these are replaced increasingly by digital capture and computed tomography (Morigi et al. 2010; Huang et al. 2016). When X-raying gold artefacts, the use of a high energy primary beam combined with suitable filtering greatly enhances the level of details that can be obtained from the same object, as can be seen below with the X-ray plates of one penannular earring in the collection of the NMS (A.1909.527.18). The earring, made of almost pure gold alloy, is one of a pair found by Petrie (1909) in a Second Intermediate Period burial at Qurna (see Chapter 9.2). These earrings display little use-wear and the X-ray obtained at 340 kV allows a detailed observation of the shaping of the earrings and the soldering technique used (see Fig. 9.7b in Chapter 9.2).

Another example is provided in Chapter 8.8, where the X-raying of a Middle Kingdom string in the British Museum (EA3077), revealed the presence of small round beads (possibly made of ceramic or metal) inside one of the cowrie-shell shaped beads, possibly deliberately to produce some sound. This explains the tinkling sounds of other gold cowrie shell-shaped

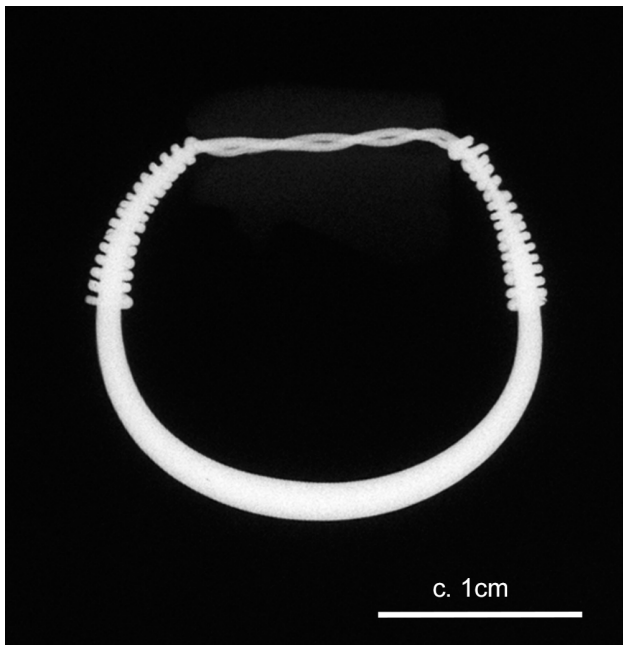


Figure 6.5. X-radiograph of finger-ring NMS A.1883.49.8 showing the twisted shank wire within the carnelian bezel (NMS X-ray plate 260209-4, 3.5 mA, 300 kV, 1 min, lead screen, 2 mm Cu filter, Structurix film D7).

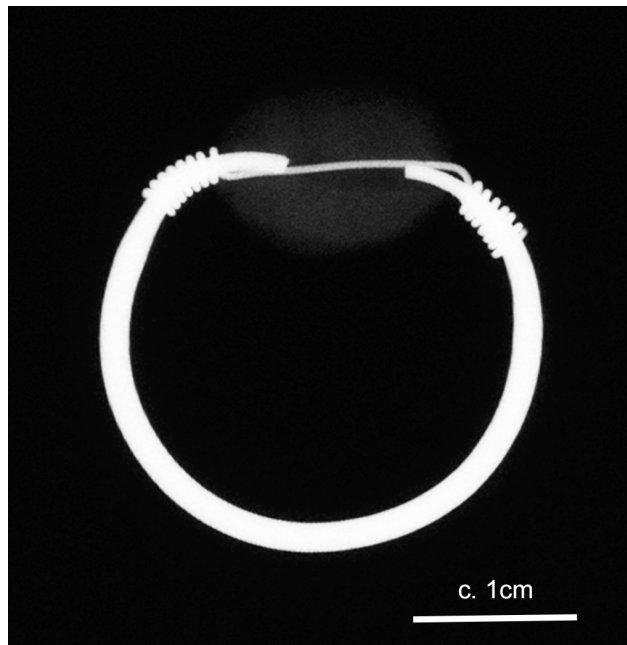


Figure 6.6. X-radiograph of finger-ring NMS A.212.12 showing the cut shank ends within the steatite bezel and the additional coiled wire (NMS X-ray plate 20091009-12, 4 mA, 180 kV, 4 min, lead screen, 2.7 mm Cu, Structurix D7).

beads dated to the Middle Kingdom (see Chapter 8.8), several from the tomb of Hor excavated at Abydos (Silverman 1997, 197) and those from Princess Mereret's girdle (Andrews 1990, 141–2). X-radiography can also reveal hidden information, as for the Second Intermediate Period girdle from the mentioned Qurna burial, in the collection of the NMS (A.1909.527.18). Several barrel beads have slipped inside a wallet bead (Fig. 9.3c in Chapter 9.2), which allowed us to re-evaluate the number of barrel beads in comparison to what was reported for that item by Petrie (1909) in his excavation report. Additional features visible on that X-ray plate are small variation in densities within the wallet beads, resulting from shaping the gold sheet to the required form and from the chased decoration, both of which changed the gold foil thickness.

X-radiography can also be used to investigate mounting techniques, for example the swivelling mechanism of finger-rings. Figures 6.5 and 6.6 compare the mounting techniques of two finger-rings from the NMS collections. Both finger-rings comprise a bezel made in a material more transparent to X-rays than gold: a carnelian *wedjat*-eye (NMS A.1883.49.8, Fig. 6.5) and a glazed steatite scarab (NMS A.212., Fig. 6.6). X-ray observation reveals different mounting techniques. Finger-ring A.1883.49.8 presents the typical mounting technique observed in New Kingdom finger-rings (see Chapter 10.4.3), the gold shank was thinned to enter the bezel and then coiled at each extremity to create the swivelling mechanism. In the case of finger-ring A.212.12, a wire was added to decorate the hoop and create the effect of a swivelling mechanism. Microscopic observation revealed the use

of a modern drawn wire and therefore confirmed a modern addition.

Finally, X-ray imaging can also reveal the presence of hidden pieces of jewellery present in wrapped mummies. The first X-radiographies carried out on the mid-18th Dynasty mummies of Kha and his wife Meryt by Curto & Mancini (1968), revealed the presence of ribbed penannular earrings, a broad collar and a girdle wore by Meryt as well as penannular earrings, a bracelet, a heart-scarab, several amulets and a collar wore by Kha. The collar of Kha is a string of lenticular beads in gold and, despite containing one single strand of beads, has been identified as a shebyu collar (Binder 2008). The mummies were imaged again in 2001 with Multidetector computed tomography (MDCT) and in 2014 using mobile X-radiography (Bianucci et al. 2015). In addition to the quite detailed images obtained for the jewellery, the presence of additional pieces was revealed, including several finger-rings on both bodies and a bracelet worn by Meryt. Among the grave goods of Kha and Meryt, two sealed vases were additionally submitted to neutron radiography and tomography (Festa et al. 2018). Other recent studies using MDCT were undertaken to investigate royal mummies dated from the 18th to the early 20th Dynasties in the collection of the Egyptian Museum in Cairo. Of interest, is the study of the mummy of king Seti I, which revealed the presence of different amulets placed inside the wrapping bands (Saleem & Hawass 2014).

References

For references see pp.185–91 at the end of this chapter.

Chapter 6.3

Egyptian gold jewellery under the SEM-EDS

Maria F. Guerra

From optical to electron microscopy

Based on the interaction of radiation with matter and using both particle and wave properties of the radiation, scientific imaging provides a wide range of details on objects made from precious metals. By choosing the equipment and the imaging conditions – type of incident radiation, wavelength (from the infrared to the gamma rays in the case of electromagnetic radiation), angle of incidence, etc. – precise details on the same object can be imaged at different depths (from surface to bulk) and at different magnifications.

Among the most popular methods used to reveal manufacturing traits of gold jewellery are microscopy techniques, with conventional optical microscopes and electron microscopes being the most widely used devices. As the smallest distance that our eyes can resolve is 0.1 to 0.2 mm (Croft 2006), by simple observation of the object those techniques can reveal details that are invisible to the naked eye.

The use of optical microscopy in the study of gold jewellery consists in general of the observation of an object under a stereomicroscope, without any prior preparation or sampling, and using incident white light as illumination source. The images obtained can be captured –for example with digital or CCD cameras – and then stored. A broad range of optical microscopes with different magnification powers is nowadays available, many of them being compact and therefore mobile, with some low-cost devices (several can be plugged into a USB port on a computer) having rather good quality objective lenses.

Although higher magnification can be reached, the most common objective lenses have magnification powers from $\times 4$ to $\times 100$, because spatial resolution is limited by the diffraction of the light passing through the opening. For an object represented as the sum

of an infinite set of point sources, the lowest distinguishable distance between two of them is limited by the wavelength of the light source (380–780 nm for visible light), the numerical aperture of the objective lens (typically 0.2 to 1.3) and the refractive index of the imaging medium (Wolf 2007). Therefore, in the most favourable case, the lateral resolution of a conventional optical microscope cannot exceed 0.2 μm , and the useful magnification varies from $\times 500$ to $\times 1000$ (Abramowitz 2003, Hinsch 2007).

It was only in the 1930s that researchers overcame the difficulties related to the resolution limit associated with the properties of light. This was achieved by replacement of the visible light source by an electron beam – electrons have much shorter wavelengths than visible light – and consequent replacement of the optical lenses used to focus the radiation by electromagnetic lenses. The development of electron microscopes, based on the interaction of electrons with matter, made it possible to observe details hitherto inaccessible.

Electron microscopes play a crucial role in the field of cultural heritage (e.g. Ponting 2004; Adriaens & Dowsett 2004; Schreiner et al. 2007; Freestone et al. 2007; Meeks et al. 2012; Brunetti et al. 2013; Sciau 2016), in particular Scanning Electron Microscopes (SEM) and Transmission Electron Microscopes (TEM). However, a thin sample (nanometric) must be prepared for examination in a TEM (Williams & Carter 2009) whilst an object can be observed without preparation under a SEM. This makes SEM one of the most attractive techniques in the field of cultural heritage. Because of its characteristics, SEM is a technique widely applied to the study of goldwork (e.g. Duczko 1985; Meeks 2000; Guerra 2006; Fitton et al. 2009; Perea et al. 2010; Martínón-Torres et al. 2012). Other than the magnification, the important role of SEM in the study of jewellery is related to the use of

an electron beam as the illumination source, because it allows overcoming the problems related to the high reflectivity of silver (for wavelengths $> 0.3 \mu\text{m}$) and gold (for wavelengths $> 0.5 \mu\text{m}$) under visible light (Hass 1955, fig. 1).

The useful magnification of a SEM varies from $\times 200.000$ to $\times 1.000.000$, and its resolution can attain $c. 1 \text{ nm}$ (Ul-Hamid 2018), depending on the type of equipment available. For example, although the electron beam is often obtained by heating a tungsten filament to a temperature of $c. 2800 \text{ K}$ (thermionic-emission gun), an SEM can be equipped with a higher brightness electron source such as a FEG (field emission gun). However, even though it provides higher spatial resolution and higher magnification, operated below $\sim 10^{-7} \text{ Pa}$ the FEG requires the use of higher vacuum in the sample chamber than the vacuum used in a conventional SEM (below $\sim 10^{-4} \text{ Pa}$).

Imaging with SEM

In a SEM, the samples are imaged by scanning their surfaces with a focused electron beam. The interaction of electrons with matter causes the emission of electromagnetic radiation and particles as shown in Figure 6.7. SEM imaging uses the elastic and inelastic scattering of electrons. These electrons, which have different energies, are collected and transformed into images that are displayed on a screen and which can be stored. The electrons elastically scattered (higher energy) are named backscattered electrons (BSE); they are used to produce images in chemical contrast, that is, differences in atomic number (Z) are reflected as differences in contrast. Those resulting from inelastic scattering with the sample (lower energy) are named secondary electrons (SE); they are used to produce images in topographic contrast.

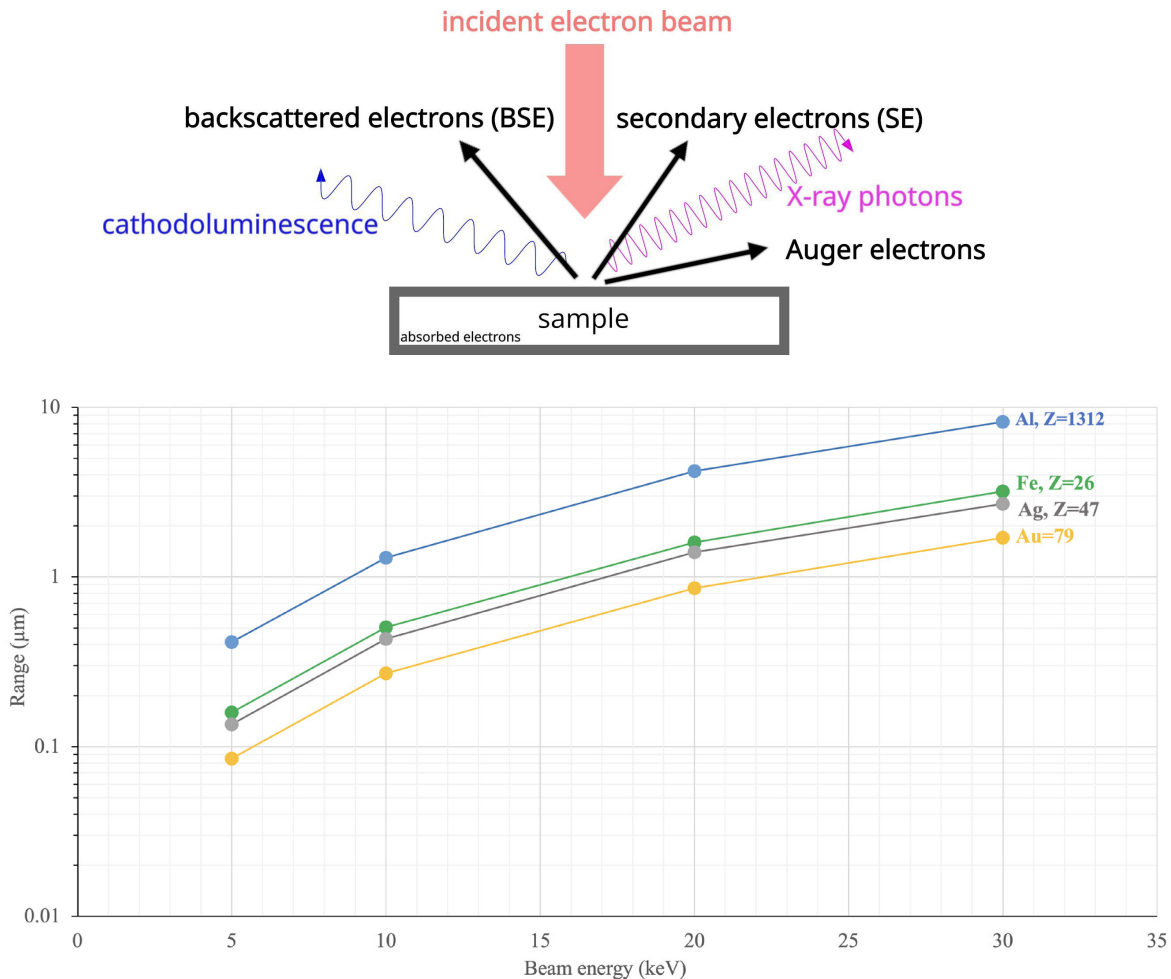


Figure 6.7. (Top) the main emissions that occur when a thick sample is bombarded with an electron beam in an SEM; (above) the radius of the interaction volume centred on the beam impact point for four metals with different Z in function of the energy of the incident electron beam (based on Goldstein et al. 2018, tab. 1.1).

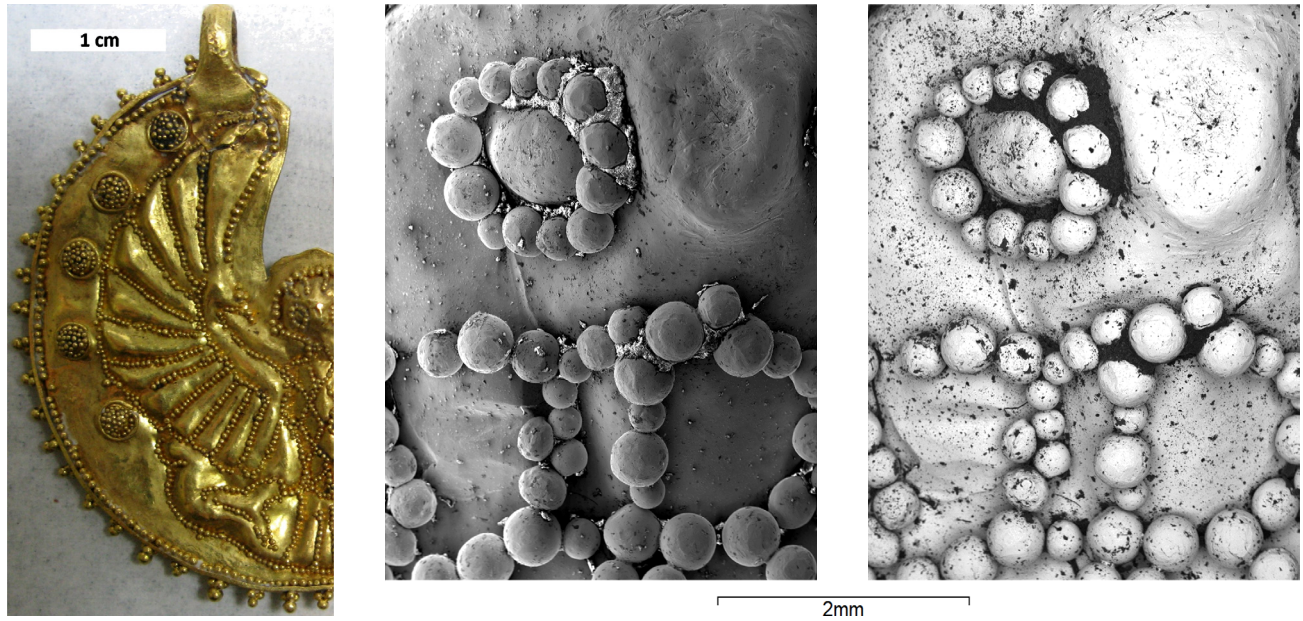


Figure 6.8. On the left, one of the symmetrical parts of gold pendant N 1855A in the form of a hawk with spread wings. On the right are shown the SE (left) and the BSE (right) images of a detail of the decoration obtained under the SEM.

Figure 6.8 shows the SE and BSE images of a detail of the decoration in repoussé and granulation of a gold pendant. Dirt and dust, with low Z, appear black, particularly between the granules, whilst gold, a high Z material, appears whitish. In a BSE image, the brighter the material appears, the higher its Z is. Because they are non-conductive, dirt and dust appear in the SE image very bright, enclosed in a blackish halo. This is associated to charging. This image defect is caused by saturation of the signal during image acquisition (Goldstein et al. 2018). Electron accumulation in the sample can be reduced by either coating the low conducting samples with a thin layer of a conducting material (carbon, gold, platinum) or operating the SEM in low vacuum. Although made from high conducting materials, fragile jewellery (e.g. corroded) and jewellery containing materials that charge up or outgas in vacuum can hardly be analysed using conventional SEM. The development of, among others, variable pressure (VP-) and environmental (E-) SEMs, which allow for low vacuum imaging (Stokes 2008, 2012), greatly improved the versatility of the technique, in particular when the equipment includes sample chambers that accommodate large objects.

As the volume of interaction in the sample is small (varying with the energy of the electron beam and the Z of the material), the information only comes from the surface of the sample. Observation of a complex gold or silver object under an SEM provides therefore a wide variety of information on its surface. For example,

particular details can be observed just by increasing the magnification in an area of interest as shown in Figure 6.9 for the mentioned pendant, where a small piece of gold sheet can be seen, that remained stuck under one of the granules.

The unprovenanced pendant observed under the SEM (no. 93 in Seipel 2001) is made by joining two gold sheets in repoussé with granulation, cut to the form of a hawk with spread wings. Bought from B. Drovetti in 1827 as a pendant hanging from a now absent gold chain (no. 178 in Champollion 1827),¹ it is part of the Louvre Museum collection (N 1855A). The pendant is dated to c. 1500–1300 BC,² because it is typologically and technologically close to the crescent and hawk type pendants (nos. 1–17 in Negbi 1970³) excavated in Tell el-Ajjul (Petrie 1931–34; Petrie 1952) and to the hawk pendant found inside the Uluburun shipwreck (Bass 1986; Pulak 2008). None of them, however, is as close to N 1855A as the unprovenanced two pieces in the Rijksmuseum van Oudheden in Leiden (G 1272-3), probably bought in 1828 from G. Anastasi. They were suggested to come from an Egyptian find (Lilyquist 1993, 1994). Their technological description in Tufnell (1983) can be used to describe the manufacture of N 1855A. All three pieces are so similar that the same workshop (or goldsmith) could have produced them.⁴

Figure 6.8 shows the hawks' beak and one of the eyes in repoussé, the latter surrounded by granules with a wide variety of diameters. On the other side

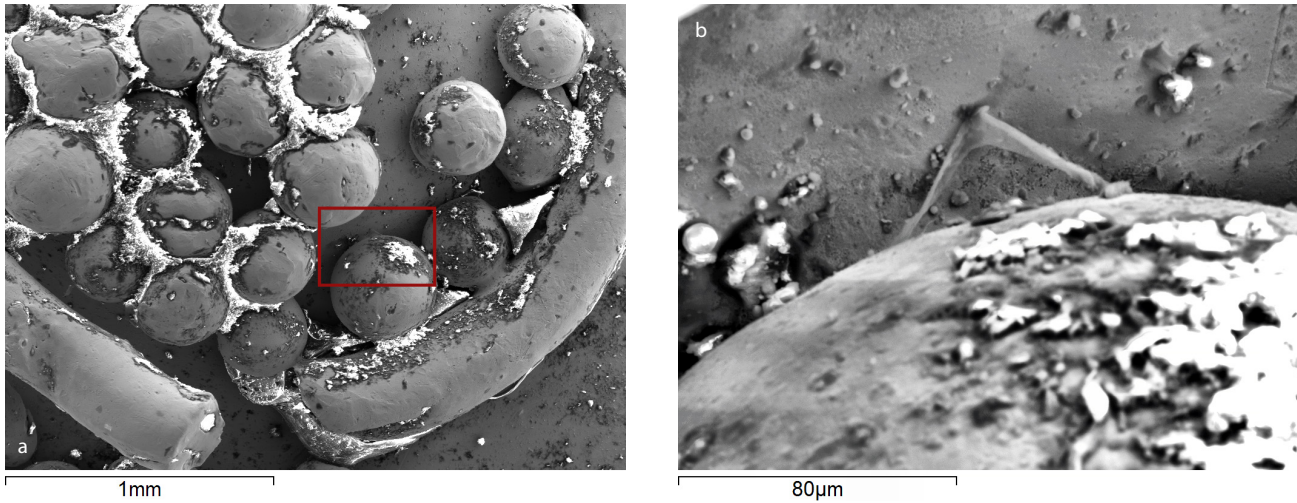


Figure 6.9. SE images of a detail of pendant N 1855A, revealing the presence of a small piece of gold stuck under one of the granules by increasing the magnification.

of the pendant, shown in Figure 6.10a, the smallest granule (1) has a diameter of 0.25 mm and the biggest granule (2) of 0.5 mm whilst in Figure 6.10b the smallest granules (1,2) have a diameter of less than 0.2 mm and the biggest (3) of 0.5 mm. This shows that the granules were not selected by diameter. Even more interesting is the shape of the granules. One shown in Figure 6.10a is a small piece of gold strip (3) whilst another (4) is a small piece of rounded wire. Interestingly, one hawk pendant from Tell el-Ajjul in the British Museum (EA 130764) contains granules with a wide variety of diameters and some small pieces of rounded wire. This is also the case of one of the pairs of crescent pendant contained in Tell el-Ajjul hoard 1299

(McGovern 1985), which show small pieces of gold strip and wire among the granules (Politis 2001, fig. 9.5). According to Petrie (1934, 5–6, pl. 14–26, 27), this pair of crescent pendants is probably a local Palestine imitation of the others contained in the same hoard.

Could this explain the small piece stuck under the granule in Figure 6.9? According to Nesler and Formigli (2004, 44), granules were produced in the past by heating small pieces of gold strips and wires. Due to surface tension, their shape change during solidification to reach a final spherical shape. All of these shapes have been observed under the SEM in ancient gold jewellery (e.g. Platz-Horster & Tietz 1995; Nesler & Formigli 2004; Guerra 2007). On the hawk's body

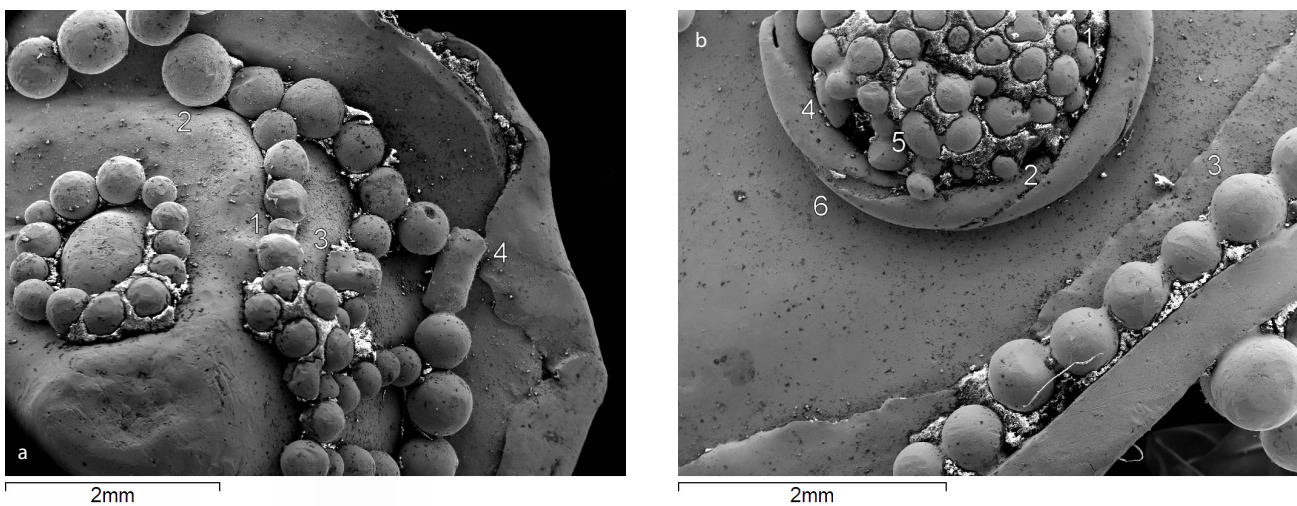


Figure 6.10. SE images of pendant N 1855A showing details related to the production of the granules and wires.

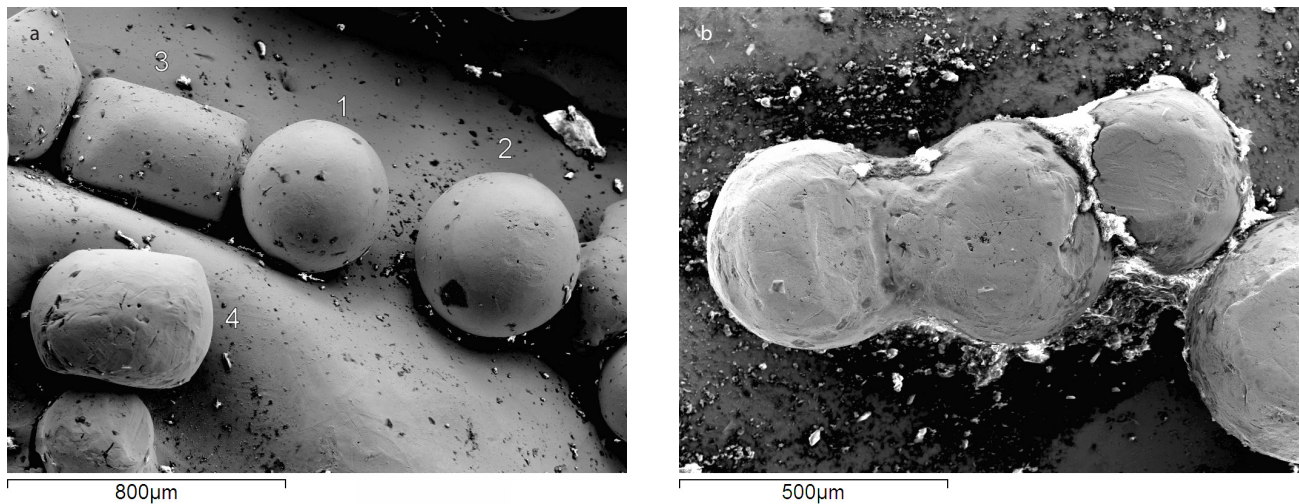


Figure 6.11. SE images of pendant N 1855A showing details related to the production of the granules.

(Fig. 6.11a), two perfectly rounded granules (1,2) are situated next to two small pieces of wire, one with the initial form (3) and the other that started to melt (4). Two pieces of wire in contact that did not completely form a larger sphere can be seen in Figure 6.11b. In Figure 6.10b, one small piece of rounded wire (4) is among the granules as well as another (5) not yet fully round. In this figure and in Figure 6.9 are shown wires made by twisting a gold strip. Their diameters are similar to the diameter of the small pieces used to make the granules.

SEM-EDS microanalysis

Among the electromagnetic radiation emitted by a sample bombarded in a SEM with an electron beam (Fig. 6.7) are X-rays produced in the sample by photoelectric effect (see Chapter 6.4). As each chemical element emits a unique pattern of X-rays, by equipping the SEM with an energy dispersive X-ray spectrometer (EDS or EDX) it is possible to obtain chemical qualitative and quantitative information on the sample elemental composition. The detection and processing of the emitted characteristic X-rays are similar for SEM-EDS and EDXRF. Additionally, information about the microstructure of the sample can also be obtained in a SEM by EBSD (electron backscatter diffraction), when equipped with an appropriate detection system (e.g. Northover & Northover 2012, Pérez-Arantegui & Larrea 2015). Analysis using an electron probe and wavelength dispersive spectrometry (WDS) is carried out with an equipment very similar to an SEM. Named Electron Probe Micro Analyser (EPMA), it enables high spatial resolution chemical analysis with improved detection limits and low spectral interferences.

SEM-EDS is one of the most widely used methods for examining jewellery. It provides access to imaging and analysis of very small details, such as PGE (platinum group elements) inclusions found on the surface of objects made from alluvial gold (Meeks & Tite 1980) and the small jewellery components like granules and wires. However, as mentioned, the depth of analysis with an electron beam is quite small. For pure gold, the radius of the hemisphere centred on the electron beam impact point at the surface of the sample, representing the theoretical interaction volume, is under $1\ \mu\text{m}$ for a beam energy under 25 keV (Fig. 6.7). This can be exploited in the case of jewellery, through elemental mapping with high spatial resolution. Elemental mapping, which is one of the most interesting possibilities offered by SEM-EDS, combines image with chemical analysis, providing for a chosen area the distribution on the surface of the object of the selected chemical elements, which after processing can be represented in colour codes (Olsen 1988; Meeks 1998; Friel & Lyman 2006; Wu et al. 2021).

Pendant N 1855A has no visible PGE inclusions, but its many small components have been analysed by EDS, such as those indicated in Figure 6.12 in the pendant's edge. The results obtained for these and other components of the pendant are summarized in Table 6.2, showing that they are all made from alloys containing 4 to 6 wt% Ag and no copper. The analysis by μPIXE (see Chapter 6.5) of several parts of the pendant revealed that it contains only 0.1–0.2 wt% Cu (Table 6.2). Therefore, the amounts of copper in the alloys are below the detection limits of EDS.

The analyses carried out in the joints of several granules and wires showed no change in composition and none of the joints has the morphology expected for

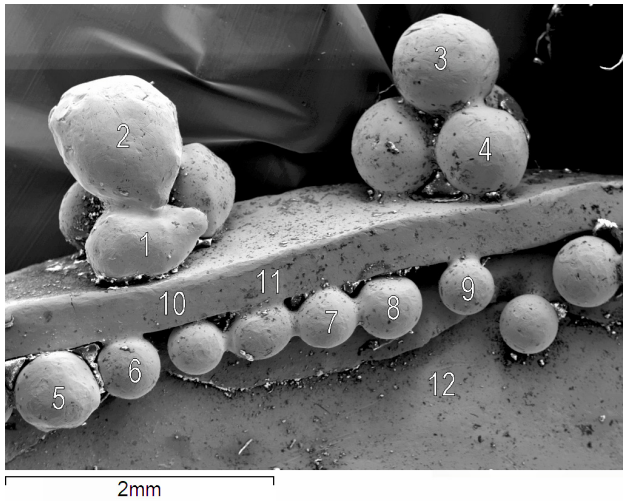


Figure 6.12. SE image of a detail of pendant N 1855A edge, where are shown the areas analysed by EDS (composition given in Table 6.2). It is noticeable the different shapes of the granules in the conic ornaments and the different sizes of the aligned ones.

hard soldering. Politis et al. (2002) have also observed this for two crescent pendants from Tell el-Ajjul in the Ashmolean Museum (1949.307 and 1949.308). Only the small piece of gold strip under the granule in Figure 6.9 could be a partially melted paillon (a piece of sheet solder coated with flux, see Grimwade 2002). However, this suggestion is not validated by the composition of the granule and the small strip, as they both contain c. 5 wt% Ag and no copper. The small components of the pendant's decoration have probably been assembled by diffusion bonding, using copper compounds and an organic glue. With this technique, it is possible to obtain very thin joints. However, most often placed under the granules and wires, these joints are difficult to analyse without sampling. Parrini et al. (1982) were able to observe by SEM-EDS an increase in the joints of the amount of copper, from 1.3 to 5 wt%, only when they analysed in section small samples taken from two ancient pieces of jewellery with granulation

Notes

1. In the list of Drovetti's jewellery ('Bijoux', nos. 250–72, 'Inventaire de la collection Drovetti, 1827', Archives des musées nationaux, Registres des Collections, répertoires et inventaires, 20150162/86), earring N 1855A is no. 258, described as follows: 'Chaîne, travail de gourmette, avec plaque représentant un épervier'. The penannular earring

Table 6.2. Results obtained by SEM-EDS and μ PIXE analysis of several components of gold pendant N 1855A.

| Area of analysis | Cu wt% | Ag wt% | Au wt% |
|------------------------------------|--------|-----------|--------|
| <i>EDS (nos. Fig. 6.12)</i> | | | |
| big granule 1 | 0.0 | 4.22 | 95.78 |
| big granule 2 | 0.0 | 4.25 | 95.75 |
| big granule 3 | 0.0 | 4.07 | 95.93 |
| big granule 4 | 0.0 | 4.34 | 95.66 |
| small granule 5 | 0.0 | 4.99 | 95.01 |
| small granule 6 | 0.0 | 4.32 | 95.68 |
| small granule 7 | 0.0 | 4.15 | 95.85 |
| small granule 8 | 0.0 | 4.29 | 95.71 |
| small granule 9 | 0.0 | 4.98 | 95.02 |
| edge sheet 10 | 0.0 | 5.56 | 94.44 |
| edge sheet 11 | 0.0 | 5.62 | 94.38 |
| base sheet 12 | 0.0 | 6.24 | 93.76 |
| <i>EDS (other areas)</i> | | | |
| Granules on the body (35 analysed) | 0.0 | 4.7 ± 0.4 | 95.3 |
| Wires around granules (6 analysed) | 0.0 | 5.3 ± 0.3 | 94.6 |
| Base sheet (5 analysed) | 0.0 | 6.2 ± 0.2 | 93.75 |
| Suspension ring (2 analysed) | 0.0 | 6.4 ± 0.2 | 93.5 |
| <i>PIXE</i> | | | |
| Base sheet | 0.1 | 6.2 | 93.7 |
| Wire around granules | 0.15 | 6.2 | 93.8 |
| Suspension ring 1 | 0.2 | 6.2 | 93.6 |
| Suspension ring 2 | 0.2 | 6.0 | 93.8 |
| Granule on the body | 0.1 | 5.4 | 94.5 |
| Granule on the edge | 0.15 | 4.9 | 94.9 |

N 1855B studied in Chapter 10.3 is not included in this list, but was represented mounted together with N 1855A without the chain (Fontenay 1887, 138).

2. It is tempting to mention the posture of the hawks represented in the Old Assyrian gilded ivory plaques from Achemhöyük and on a ceramic lid from Mallia (dated to 19th–18th century BC, Aruz 2008).
3. One hawk earring from Gaza (Petrie 1932, pl. 1) stolen in London (Tufnell 1983) is not included.
4. Two disc pendants in Leiden (AO 1c (a) and (b)) said to be from the same find (Lilyquist 1994), seem from visual observation the work of two goldsmiths.

References

For references see pp.185–91 at the end of this chapter.

Chapter 6.4

Elemental analysis of goldwork with portable XRF equipment

Maria F. Guerra & Marcos Martín-Torres

X-ray fluorescence spectrometry (XRF) is one of the most versatile techniques applied to the determination of the elemental composition of ancient gold, and one of the most commonly used – in this project and others. The reasons for its popularity include its penetration depth, often yielding reliable results about the bulk of an object even if analysed non-invasively from the surface, along with the growing availability of relatively affordable mobile devices. This makes it possible to bring the instrument to the field or the museum store, minimizing thus the risk of moving precious objects. While there is no doubt that this instrumentation allows faster and cheaper analyses of larger numbers of objects, it is important to make sure that calibrations and operating parameters are appropriate for the material in hand. Equally, considerations such as sample geometry and the presence of surface treatments ought to be factored in when interpreting the results.

XRF is based on wavelength dispersive (WD) or energy dispersive (ED) detection of the characteristic (or fluorescent) X-rays emitted by the atoms in a sample when bombarded with an incident beam of photons. In most cases, incident radiation is generated by an X-ray tube, but synchrotron radiation and gamma rays emitted by radioactive sources are other possible sources for XRF. Other techniques applied to the determination of the elemental composition of ancient materials are based on the same phenomenon, but use other sources of incident radiation. Examples are PIXE (discussed in Chapter 6.5), which typically uses proton beams although other ion beams can be employed (such as alpha particles), and EDS (discussed in Chapter 6.3), which uses incident electron beams.

In the case of XRF, as the X-rays hit the sample, the energy of the incident photon is transferred to inner shell electrons in the atoms of the material analysed; these are ejected, and electrons from higher shells

subsequently fill the shell vacancies (photoelectric effect). For each of these so-called transitions, an X-ray with an energy that corresponds to the binding energy of the ejected electron is emitted (fluorescent radiation). This is why each chemical element emits a unique pattern of characteristic X-rays. The elemental composition of the analysed objects is thus based on the collection of the emitted X-rays, whose intensity increases with the concentration of the element in the bombarded material. Calculations are carried out with very good accuracy by using physical models that predict these interactions (fundamental parameters), and these may be supplemented by analysing reference materials of known composition (empirical calibration).

Photons are neutral, which means that their penetration is high compared to charged particles; however, in materials made of elements with high atomic number (Z), such as gold, their absorption is also high. Due to the probabilities associated to both the atom excitation and the emission of photons (fluorescent yield), XRF is a technique more adapted to the analysis of elements of medium and high Z . The quality of the data that can be obtained is very dependent on the characteristics of the equipment used and on the analytical parameters chosen, such as the accelerating voltage, beam current, and acquisition time – in addition to matrix-matched correction procedures employed to transform the raw spectrum generated by the detector into elemental compositions.

The equipment available for XRF spectrometry can take different forms: it can be stationary for *ex situ* analysis in the laboratory, or mobile for *in situ* analysis. The latter range from desktop-based instruments of considerable weight to fully handheld devices weighing less than 2 kg. WD detectors (WD-XRF) allow for lower detection limits and fewer spectral interferences, but these require a monochromator to diffract the

characteristic radiation emitted from the sample, thus these systems are less compact and more difficult to move than those using ED.¹ ED-XRF is therefore the most common method found in mobile equipment and the most widespread technique for the analysis of the elemental composition of archaeological jewellery, because often the items cannot be moved from their location.

The XRF system of the NMS used in the analysis of the jewellery items from that collection is an Oxford Instruments ED 2000 air-path X-ray fluorescence (XRF), with a Rhodium target X-ray tube collimated to a point of about 2×1.5 mm, coupled to a Si(Li) detector using the Oxford Xpert Ease software. At the British Museum, the XRF system employed for analysis of the Egyptian jewellery discussed in this volume is a Bruker Artax spectrometer with a Mo X-ray tube, a 50 kV, 50 W high voltage generator and a Peltier cooled Silicon Drift Detector (SDD) detector with an energy resolution of 150 eV at 5.9 keV (Mn $K\alpha$).

Stationary XRF equipment usually allows for higher performance than mobile and handheld equipment, for example in terms of the spatial resolution and detection limits. For example, very compact systems include small X-ray tubes, which means a low intensity source of radiation resulting in lower measurement precision and need of longer acquisition times. These systems cannot be enhanced by X-ray optics, which means that they provide beam spot sizes typically in the order of a few millimetres in diameter, and are therefore less suited for the analysis of small objects or details thereof. Conversely, large systems use high power X-ray tubes with high flux and polycapillary optics that improve the spatial resolution. Using μ beams, these systems can provide elemental maps of the analysed areas with a spot down to a few tens of μ m. Use these systems might require to move objects to laboratories. Some commercial systems are however equipped to be transported for *in situ* analysis² and several research teams (for example Scrivano et al. 2017) have developed compact in-house systems. The benchtop M4 Tornado from Bruker used in Chapter 6.8 for the study of the corrosion mechanisms of gold alloys, providing spot sizes down to 25 μ m for Mo $K\alpha$ radiation, is competitive in spatial resolution with the μ PIXE system described in Chapter 6.5, which in routine uses a 50 μ m diameter proton beam (that can be lowered, but at the expense of the detection limits). In order to reach even higher spatial resolution, it is possible to use EDS (see Chapter 6.3). When using a field emission gun (FEG-SEM) it is possible to obtain resolutions down to a few nanometers (Burgess et al. 2013) for the determination of elements contained in the outermost layer.

Several mobile systems were used for the study of Egyptian jewellery in this volume. Figures 6.13 to 6.15 show images of the analysis of jewellery at the Petrie Museum using two instruments. Figure 6.13 shows the CNRS XRF portable system, consisting on an Ag Moxtek End Window X-ray Source operated at 35 kV and 95 μ A, a Peltier cooled X-ray SDD AXAS V detector produced by Ketek, with a resolution of 144 eV at 5.9 keV, and an Amptek ADC/MCA 8000A,

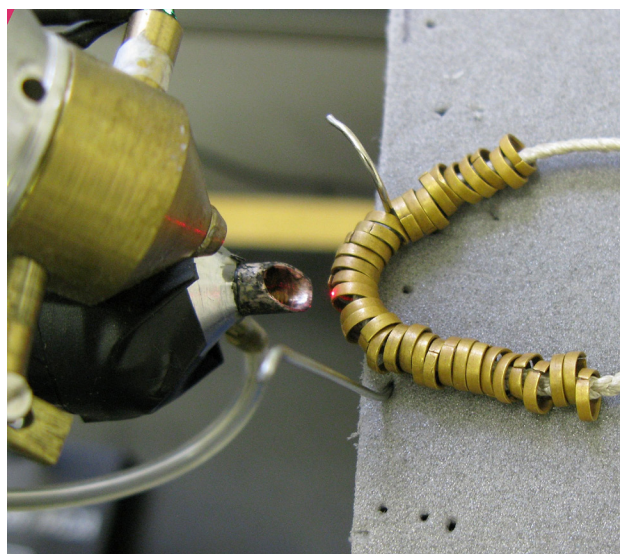
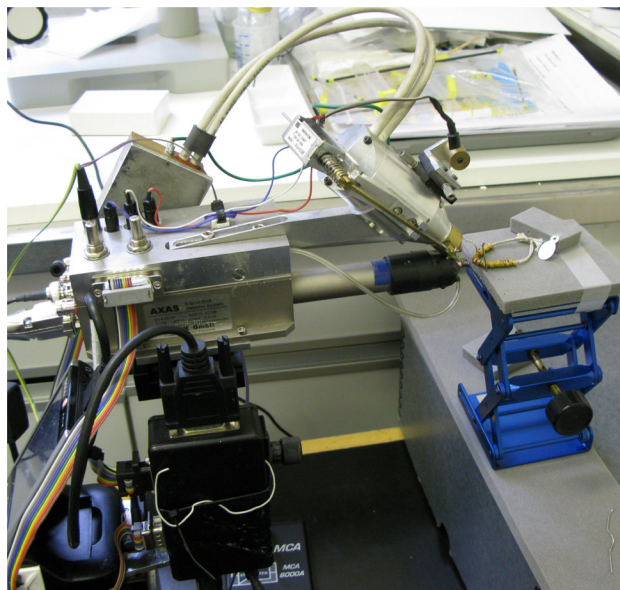


Figure 6.13. Analysis of Egyptian jewellery at the Petrie Museum, using the CNRS in-house built portable XRF spectrometer where can be seen the positioning at the surface of the object of the 1 mm^2 beam spot (area of analysis) using a laser beam.

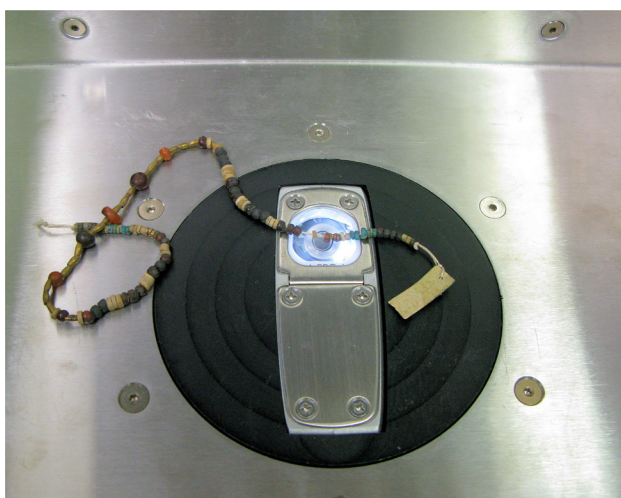
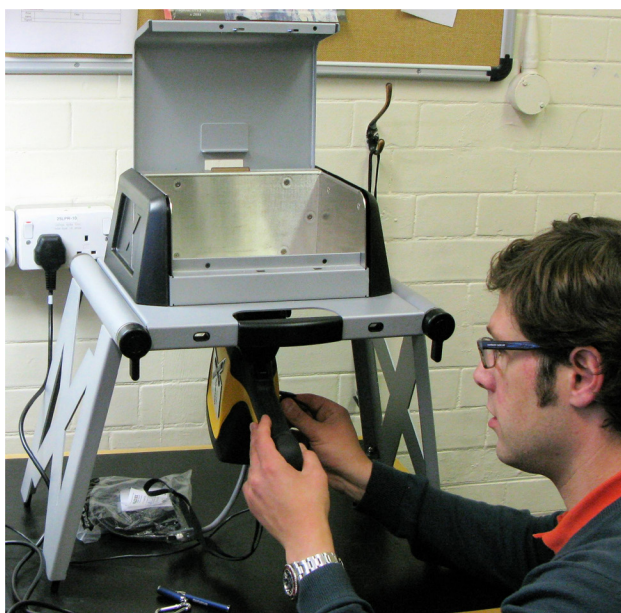


Figure 6.14. Analysis at the Petrie Museum, using the handheld XRF equipment of the Institute of Archaeology, UCL, of string of beads UC26275. Each bead was positioned for analysis using the integrated camera.

mounted on a home-made XYZ table at a geometry of 45° source-sample and 90° source-detector (Viguerie et al. 2009). Two laser point the beam spot of 1 mm² on the object surface. Spectra are processed with free, open-source, PyMCA fundamental parameters software (Solé et al. 2007). A set of certified gold alloys was used to construct the calibration matrix (Adrimi-Sismani et al. 2009).

Figure 6.14 shows the UCL Institute of Archaeology handheld XRF. While the instrument can be used by hand, it can also be mounted on a workstation for

mobile benchtop use. This instrument is an Olympus Innov-X Delta Premium, with Rh X-ray tube and a Peltier-cooled SDD, running at 40 kV and 100 µA, with an Al filter and a resolution better than 150 eV at 5.9 keV. The instrument has a collimator allowing to narrow down the beam to a 3 mm diameter, and an integrated camera that shows and records the location of the analysed area. The spectra were evaluated using the manufacturers' Alloy Plus method, based on fundamental parameters and optimized with additional reference materials.

Two additional handheld systems, shown in Figures 6.15 and 6.16, were used during the project, one belonging to the C2RMF (Guerra & Pagès-Camagna 2019) and another to the University of Liverpool (Trolen et al. 2019). They are both Niton XL3t systems from Thermo Scientific with GOLDD technology, equipped with 50 kV, 200 µA X-ray tube with Ag anode, a Si PIN detector, a 3 mm spot collimator and a CCD camera for locating the regions of analysis. They were both set to 'Precious Metals' alloy mode and mounted on their workstations for mobile benchtop use. Acquisition times varied between 180s and 300s, and data processing was made with the software delivered with each equipment. Data could be relied through the systematic analysis of the same set of gold standards made from varied gold alloys (Tissot et al. 2015).

In spite of the limitations imposed by the relatively large 3 mm spot of the handheld XRF systems, by using the workstation and the built-in camera it was possible to analyse even small gold beads. Figure 6.14b illustrates the analysis of one of the gold beads from string of beads UC26275 in the Petrie Museum, found in the burial of a child excavated at Qau, precisely positioned using the integrated camera of the



Figure 6.15. The handheld XRF equipment of the C2RMF with its lightweight stand.



Figure 6.16. Analysis of penannular earring 6146b from Riqqa, in the collection of the Manchester Museum, using the handheld XRF equipment of the University of Liverpool.

Table 6.3. Results obtained using handheld XRF for three gold beads from string UC26275. Each bead was positioned for analysis using the integrated CCD camera of the equipment.

| | Au wt% | Ag wt% | Cu wt% |
|-------------------|--------|--------|--------|
| big ring bead | 68.4 | 47.1 | 3.7 |
| small ring bead 1 | 51.0 | 46.3 | 3.6 |
| small ring bead 2 | 40.1 | 52.0 | 9.9 |

Olympus Innov-X handheld XRF. Table 6.3 provides the data obtained for three individual ring beads, two small ones and a large one, analysed in the described conditions. The results obtained show variability of the gold alloys employed in a single necklace, but as the beam spot is larger than the analysed area of the smallest beads, analytical uncertainty is increased.

The objects discussed in this volume were analysed by XRF using the experimental conditions described in this chapter, and the data processed with the same sets of reference materials that include gold alloys containing variable amounts of silver and copper.

Notes

1. Recent systems such as the benchtop S6 Jaguar from Bruker are quite compact, but they still weigh more than 130 kg.
2. Systems that can be transported for *in situ* analysis are for example the Artax and the M6 Jetstream from Bruker.

References

For references see pp.185–91 at the end of this chapter.

Chapter 6.5

New analytical development for the analysis of Egyptian jewellery at AGLAE: mapping hard soldered joins and PGE inclusions

Quentin Lemasson, Brice Moignard, Claire Pacheco,
Laurent Pichon & Maria F. Guerra

The *New AGLAE* external beamline developed at the AGLAE accelerator of the C2RMF is totally dedicated to the non-invasive analytical study of cultural heritage. The extracted beamline has been especially developed to solve questions raised by these objects: determination of the elemental and structural composition of ancient materials, providing data on the manufacture technologies of the objects, on the provenance of the materials, and on their alteration mechanisms.

A new scanning system (Pichon et al. 2014) was recently developed to produce fast elemental maps with high spatial resolution. The fast data acquisition using a list mode is compatible with high sensitivity PIXE measurements, even when trace elements have to be detected. This new fast mapping setup developed at the AGLAE accelerator provides, in the case of the Egyptian jewellery, an opportunity to approach the composition of hard soldered joins and of platinum-group elements (PGE) inclusions present on the surface of the gold objects. This setup can be used even when the very uneven volume and heterogeneity of the areas to be analysed may raise major analytical challenges.

Clues on the composition of joining areas and PGE inclusions are of key importance to the understanding of crafting methods and to the identification of the type of gold employed. In Egypt, jewellery was often constructed by joining different parts. Hard soldering (Maryon 1941) seems to be widely used and may attain a very high quality for some particular jewellery items buried with important individuals (Schorsch 1995; Troalen et al. 2014). Hard solder alloys, or fillers, are in this case gold base alloys with a lower melting point than the gold alloys used to manufacture the parts to be joined. It is however difficult to estimate the original composition of hard solders, in particular in the case of small objects, since, at high temperature, the filler

runs between the parts to be joined forming an interface that after cooling down contains a combination of both the filler and the base alloys.

Concerning the presence of PGE inclusions in Egyptian gold artefacts, this was observed for the first time on the surface of objects from the excavations at Naqada (Petrie & Quibell 1896). Work recently published on Egyptian gold jewellery (Troalen et al. 2009, 2014; Miniaci et al. 2013; Guerra & Pagès-Camagna 2019) has highlighted the presence of those inclusions in the majority of the objects so far analysed. Indeed, the presence of PGE inclusions in gold objects is often related to the use of alluvial gold (Ogden 1977) and might be an indicator of the source of the metal, as done with success for gold provenancing in other areas (for example Bouchard & Guerra 2009).

Fast mapping with PIXE at AGLAE

In 2017, after significant analytical developments, the AGLAE accelerator became *New AGLAE*. In the frame of this development, a new detection system (Fig. 6.18) was implemented (Pichon et al. 2014). One of the objectives of the project was to design and set up a new non-invasive acquisition system that improves the quality of the X-ray spectra collected with reduced beam currents when sensitive materials such as works of art are analysed. This fast data acquisition through a list mode was intended to be compatible with high sensitivity PIXE measurements, which means detection of major, minor and trace elements. To that end, the volume dedicated to the detection of the emitted radiations (X-rays, gamma rays, particles) nearby the beam extraction was increased to implement a cluster of five detectors, as shown in Figure 6.17. This system also provides the possibility to accomplish large and/

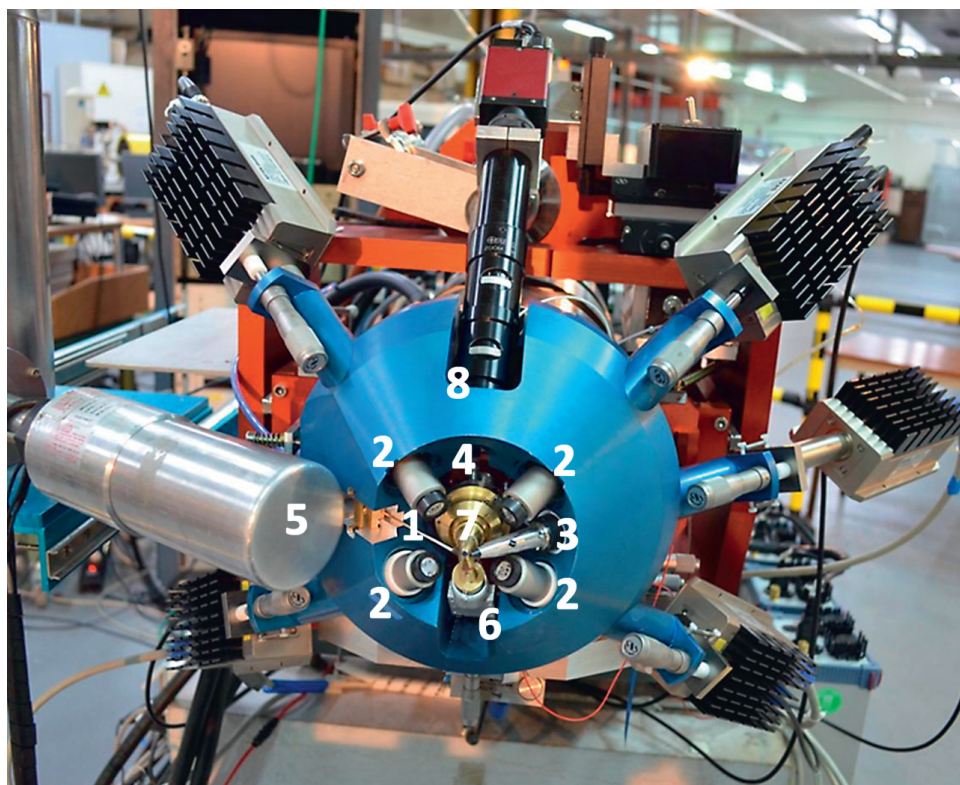


Figure 6.17. View of the AGLAE external microprobe where the detectors are located. 1: IBIL (Ion Beam Induced Luminescence) collection optical fibre, 2: high energy X-ray detectors, 3: low energy X-ray detector, 4: annular charged particle detector, 5: gamma-ray detector, 6: dose detector, 7: Si_3N_4 exit window, 8: video microscope.

or fast maps by scanning the beam across the artefacts. When mapping, a multi-parameter system saves each event registered by the X-ray, the gamma-ray and the particle detectors, simultaneously with the x and y positions of the beam on the sample.

Several in-house programs have been developed to process the dataset produced at AGLAE (Pichon et al. 2015). AGLAEMap is used for mapping handling and visualization. Elemental distribution is achieved by selecting in the spectra the regions of interest that correspond to X-ray lines chosen for each chemical element to be determined. This software has other resources, such as the possibility of obtaining elemental compositions from specific subareas selected directly from a larger area of interest or an elemental distribution map. Quantitative processing of the spectra is carried out with GUPIXWIN software (Campbell et al. 2010), which is coupled to the in-house TRAUIX software for automated calculation. TRAUIX can also provide quantitative calculation mapping.

When analysing gold alloys, PIXE is carried out with detectors covered with Al filters of $200\ \mu\text{m}$ for the determination of major elements, and with Cu filters of $75\ \mu\text{m}$ for the determination of minor and trace elements (Guerra 2004; Guerra & Calligaro 2004). Analyses are performed with a 3 MeV proton beam of 10 nA intensity and $50\ \mu\text{m}$ diameter and a total acquisition time of 5 minutes. The mapped area

can be adapted regarding the area of interest from $100 \times 100\ \mu\text{m}^2$ to several cm^2 with a resolution down to $20 \times 20\ \mu\text{m}^2$. The small size of the beam combined with the map acquiring capacities of the system to pings with small pixel sizes allow high spatial resolution acquisitions. Therefore, fine analysis down to beam size of small areas of interest, such as inclusions and joins, becomes possible.

Analytical challenges

The identification and localization of small PGE inclusions on the surface of jewellery is usually carried out under a stereomicroscope. After localization, their elemental composition is often obtained by SEM-EDS. These time consuming operations are only achievable for visible inclusions and objects that can fit in the SEM chamber. Equally, the identification of the use of a hard solder process might not be an easy task. In the case of Egyptian jewellery it has been demonstrated that the morphology of the joining areas very much depends on the expertise of the goldsmith. Some are quite thick, as expected for hard soldering, and thus easily visible, whilst others are almost invisible even when observed under the SEM (Troalen et al. 2014; Tate et al. 2009). The use of fast high-resolution PIXE mapping of areas containing joins and PGE inclusions should very much simplify the process.

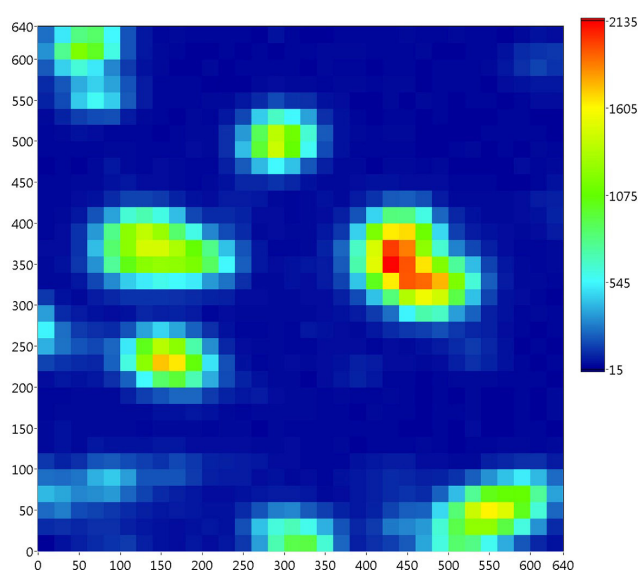


Figure 6.18. Elemental distribution by PIXE in colour scale of Ir ($L\alpha$ -line) on a selected region ($640 \times 640 \mu\text{m}^2$, pixel size $40 \times 40 \mu\text{m}^2$) of the cartouche-shaped box, one of the three elements of an armband bearing the name of Ahmose I in the collection of the Louvre Museum (E7168).

In order to discuss the possibilities of the new PIXE method developed at AGLAE for the analysis of Egyptian jewellery, the results obtained for nine gold jewellery items in the collection of the Louvre Museum, dated to late 17th Dynasty to early 18th Dynasty, are used as support (see Chapter 9.4). These objects were assembled using hard solder processes and show on their surfaces several PGE inclusions of different sizes (Lemasson et al. 2015; Guerra & Pagès-Camagna 2019), ranging from 50 to 200 μm diameter.

To reach good spatial resolution, equilibrium has to be found between the beam spot diameter and the detector count rates. This is a real analytical challenge in the case of gold objects, because PGE inclusions and joins might be heterogeneous in composition and have irregular shapes. By scanning a whole area containing PGE inclusions or joining areas, an elemental distribution map of the selected chemical elements can be constructed. Figure 6.18 shows an example of the intensity distribution map of iridium in colour scale for a small region ($640 \times 640 \mu\text{m}^2$) at the surface of one of the analysed objects. The data obtained can be exploited by selecting several areas of interest within the map (i.e. PGE inclusions or joining areas). For each of them, the concentrations of the elements in the alloys can be calculated by using the extracted spectra, which enables comparisons between the area of interest and surrounding regions. The accuracy of

the results relies on two main parameters: the depth of analysis and the homogeneity of the analysed area.

Estimating the depth of analysis

The objects analysed and the data obtained are discussed in Chapter 9.4. Their majority is made of alloys with silver contents higher than 20 wt% and copper contents ranging from 0.1 to 5.2 wt%. These results are consistent with the few data available for jewellery from the same periods (Troalen et al. 2009, 2014; Miniaci et al. 2013; Lilyquist 2003; Guerra & Pagès-Camagna 2019) and with data reported for other Egyptian items (Gale & Stos-Gale 1981). However, if all PGE inclusions analysed contain Ru, Os and Ir, such as those in other Egyptian objects analysed, Pt could also be found in some of them.

When running quantitative calculations, a key point is the estimation of the depth of analysis at the experimental conditions. Penetration depths of the incident proton beam and of the emitted X-rays for the three major elements of four representative gold alloys are given in Table 6.4a. The proton beam penetration ranges from 25 to 30 μm for all the analysed alloys whilst the penetration depth for the Au L-lines and the Cu K-lines ranges from 5 to 10 μm . The depth of analysis for the Ag K-lines being 18–36 μm , the information obtained for silver is limited by the depth penetration of the incident proton beam. Since the compounds that develop by atmospheric corrosion are generally contained in a very thin layer, under 1 μm (Guerra & Tissot 2013; Tissot et al. 2019), data obtained by PIXE should not be affected by possible surface heterogeneities.

The same calculations were carried out for the four characteristic elements of the PGE inclusion alloys. The results are shown in Table 6.4b. The penetration depths are similar to those calculated for the gold base alloys, which means that the matrix effects are comparable for gold alloys and PGE alloys. In PGE alloys that are particularly rich in Os and Ir the depth penetration is lower, because of the higher matrix density. Since the depth of analysis of PGE inclusions is around 10 μm , except for Ru that can go up to 20 μm , the gold matrix under a PGE inclusion might also be detected when using a 3 MeV proton beam for PIXE analysis.

Homogeneity of the analytical data

When analysing PGE inclusions and hard soldered joins, a major concern is the homogeneity of the data obtained. In fact, the quite variable shape and dimensions of the PGE inclusions and of the hard soldered joins, in particular their thickness, contribute to the

Table 6.4a. Depth of analysis calculated for four typical Egyptian gold alloys at our experimental conditions: an incident proton beam of 3 MeV and the emitted X-rays used for quantitative analysis.

| Alloy (wt%) | 3 MeV proton penetration depth (μm) | X-ray penetration depth (μm) | | | | | | |
|-------------|--|---|------------------|------------------|------------------|------------------|------------------|------------------|
| | | Cu | Ag | Au | Ru | Os | Ir | Pt |
| Cu–Ag–Au | | K α -line | K α -line | L α -line | K α -line | L α -line | L α -line | L α -line |
| 1–6–93 | 28.1 | 5.3 | 18.7 | 8.3 | 13.0 | 6.8 | 7.2 | 7.8 |
| 4–43–53 | 32.5 | 7.0 | 36.4 | 10.7 | 25.3 | 9.1 | 9.3 | 10.0 |
| 4–27–69 | 31 | 6.4 | 27.7 | 9.7 | 19.3 | 8.3 | 8.4 | 9.1 |
| 1–19–80 | 29.7 | 5.7 | 22.9 | 9.1 | 16.0 | 7.4 | 7.9 | 8.5 |

Table 6.4b. Depth of analysis calculated for four typical PGE inclusions of the analysed panel at our experimental conditions: an incident proton beam of 3 MeV and the emitted X-rays used for quantitative analysis.

| Alloy (wt%) | 3 MeV proton penetration depth (μm) | X-ray penetration depth (μm) | | | | | | |
|-------------|--|---|------------------|------------------|------------------|------------------|------------------|------------------|
| | | Cu | Ag | Au | Ru | Os | Ir | Pt |
| Ru–Os–Ir–Pt | | K α -line | K α -line | L α -line | K α -line | L α -line | L α -line | L α -line |
| 47–35–18–0 | 27.0 | 6.4 | 19.6 | 10.8 | 24.3 | 8.7 | 9.4 | 10.1 |
| 25–40–35–0 | 25.5 | 5.7 | 17.9 | 9.2 | 16.4 | 7.4 | 8.0 | 8.6 |
| 5–20–65–10 | 24.0 | 4.8 | 16.0 | 7.7 | 11.7 | 6.2 | 6.7 | 7.2 |
| 5–55–40–0 | 23.6 | 4.9 | 16.2 | 7.8 | 11.8 | 6.3 | 6.8 | 7.3 |

analytical difficulties raised by their analysis. While their surface dimensions are visible and can easily be calculated, their thickness remains unknown.

The influence of the heterogeneous thickness of a PGE inclusion on the calculation of the alloy composition was explored by analysing in four different zones one of the largest inclusions visible in Figure 6.18. Data obtained is shown in Table 6.5. As expected, the concentrations of Cu, Ag and Au (contained in the gold base alloy under the inclusion) increase from the centre (where the inclusion is thicker) to the edges (where the inclusion is thinner). Despite the corresponding decrease of the concentrations of Ru, Os, Ir and Pt from the centre to the rim, when the data is normalized to 100 wt% for these four elements that constitute the PGE alloys, data obtained for the four zones, shown in Table 6.6, is similar. The standard deviation, around 5–10%, is probably caused by matrix effects due to the presence of high amounts of

Os and Ir or due to errors induced by the lowering down count rates when reaching the inclusion edges. Therefore, data obtained for all the analysed areas can be considered homogeneous

The thickness of the analysed inclusion can be estimated. If we assume that the proton beam is always contained in 3×3 pixels (i.e. an area of $60 \times 60 \mu\text{m}^2$), we can consider that for area 1 in Table 6.5 the surrounding gold alloy is not significant. Therefore, the Cu, Ag and Au contents calculated for area 1 are only the result of the beam penetration reaching the gold base alloy under the inclusion. By considering the depth of analysis calculated in Table 6.4b for the elements contained in the analysed layer, the thickness of the largest inclusion in Figure 6.18 can be estimated to be around $5 \mu\text{m}$.

The analytical problem raised by the PGE inclusions is similarly raised by the hard soldered joints. As the beam spot size is much smaller than the join,

Table 6.5. Results obtained for selected areas of the biggest PGE inclusion of Figure 6.18 from the centre to the rim.

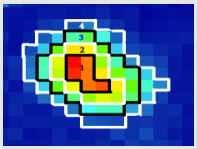
|  | Cu wt% | Ag wt% | Au wt% | Ru wt% | Os wt% | Ir wt% | Pt wt% |
|---|--------|--------|--------|--------|--------|--------|--------|
| 1 | 0.5 | 7.2 | 19.4 | 14.3 | 26.4 | 25.2 | 2.7 |
| 2 | 0.8 | 11.6 | 31.2 | 11.4 | 20.8 | 20.0 | 1.7 |
| 3 | 1.2 | 18.8 | 46.8 | 7.1 | 11.5 | 11.1 | <0.8 |
| 4 | 1.5 | 25.2 | 59.0 | 2.9 | 4.1 | 3.8 | <0.8 |

Table 6.6. Results obtained for the PGE inclusion and the gold alloy calculated based on data provided in Table 6.5, normalized to 100 wt% for each matrix. The analysed gold base alloy is also given.

| | Ru wt% | Os wt% | Ir wt% | Pt wt% |
|---|--------|--------|--------|--------|
| 1 | 20.9 | 38.5 | 36.8 | 3.9 |
| 2 | 21.1 | 38.5 | 37.2 | 3.2 |
| 3 | 23.4 | 37.8 | 36.3 | 2.4 |
| 4 | 25.4 | 35.9 | 33.9 | 4.8 |

| | Cu wt% | Ag wt% | Au wt% |
|------------|--------|--------|--------|
| 1 | 1.9 | 26.6 | 71.5 |
| 2 | 1.8 | 26.5 | 71.6 |
| 3 | 1.8 | 28.1 | 70.1 |
| 4 | 1.8 | 29.4 | 68.8 |
| Base alloy | 1.9 | 30.8 | 67.3 |

if the thickness of the join is higher than the depth of penetration of the proton beam, the results obtained by PIXE represent the composition of the joining area. Otherwise, data obtained by PIXE represent both the solder alloy and the gold base alloy. In this case, the composition of the hard solder cannot be exactly estimated. With the two soldered parts and the interface being alloys of the same elements (Au, Ag, Cu), it is impossible to make an accurate calculation of their distribution, as carried out above for the PGE inclusions. The concentration gradients that are observed can be attributed to heterogeneities caused by the soldering process, to differences in the join thickness, or to the likely combination of these two factors.

Limits of detection

The quality of the PIXE analysis of a PGE inclusion can be estimated. Since the inclusion is just a part of the mapping and the mapping is fast, the counting rate statistics by pixel associated to the elements that constitute the inclusion might be poor, resulting in higher detection limits than those obtained by point analysis. For an acquisition time shorter than 5 minutes, the charge by pixel ranges typically between 1 and 10 nC. Grouping pixels enables better statistics.

In the case of the PGE inclusions analysed in this work, according to the size of the inclusion, the acquisition time and the intensity of the beam, the limits of detection are quite variable: 1000–5000 ppm for Ru, 1000–7000 ppm for Os, 500–2000 ppm for Ir, and 1500–6000 ppm for Pt. These limits of detection are calculated based on the overall spectra, which include information on the gold base alloys. The variable thickness and irregular shape of the inclusions make quite unavoidable to get spectra without the gold base alloys under the inclusions. For the largest

inclusions (more than 100 μm wide), the limits of detection remain nonetheless the same when only the PGE matrix is considered in the calculation. For small inclusions, between 50 μm and 100 μm wide, that are difficult to separate from the surrounding gold base alloys, limits of detections attain 1–5 wt% if only the PGE matrix is taken into account. These limits of detection are adequate in most of the cases to determine the alloying elements of PGE inclusions, even when present in low concentrations. To determine trace elements, limits of detection can be enhanced by either using higher currents or by increasing the acquisition time.

PGE inclusions on hard soldered joins

This section reports one of the most challenging situations in the case of goldwork: a joining area containing PGE inclusions, as observed for one of the objects analysed in this work. Figure 6.19 shows the quantitative element distribution maps in colour scale for Cu, Ag, Au, Ir, Ru and Os, obtained for one hard soldered join ($240 \times 640 \mu\text{m}^2$) of the analysed Egyptian item, overlapped by several PGE inclusions. We could resolve the overlap by using the alloying elements of the PGE alloys and the major elements of the gold base alloy and the hard solder alloy. High variations in the Au, Ag and Cu contents can be interpreted as indicators of the presence of the filler.

The three PGE inclusions visible in Figure 6.19 are localized either on the interface where the filler ran or on the gold base plate of the object. Their compositions are different (though two inclusions are similar), but this fact is independent of their location on the object's surface. Table 6.7 summarizes the average compositions of the three PGE inclusions and of the gold alloys used to make both the base gold plates and the filler, calculated by selecting the corresponding areas in the maps and normalizing each alloy to

Table 6.7. Results obtained for the PGE inclusions, the hard solder alloy and the base alloy, normalized to 100 wt%, calculated by scanning the joining area shown in Figure 6.19.

| | Ru wt% | Os wt% | Ir wt% | Pt wt% |
|---|--------|--------|--------|--------|
| 1 | 39.5 | 31.2 | 28.5 | 0.8 |
| 2 | 26.1 | 33.1 | 37.5 | 3.3 |
| 3 | 2.9 | 83.2 | 10.0 | 3.9 |

| | Cu wt% | Ag wt% | Au wt% |
|--------|--------|--------|--------|
| Gold | 0.8 | 3.7 | 95.5 |
| Solder | 10.0 | 8.2 | 81.8 |
| PGE1 | 0.8 | 4.5 | 94.7 |
| PGE2 | 9.2 | 7.1 | 83.7 |
| PGE3 | 9.3 | 8.3 | 82.4 |

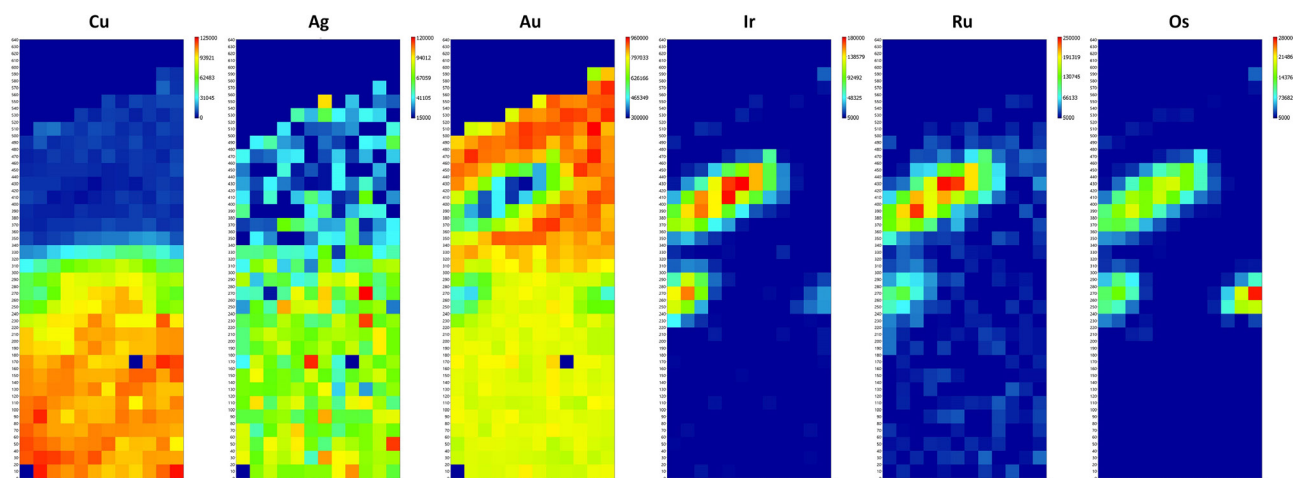


Figure 6.19. Elemental distribution by PIXE in colour scale of Cu, Ag, Au, Ir, Ru and Os on a selected region ($240 \times 640 \mu\text{m}^2$, pixel size $40 \times 40 \mu\text{m}^2$) of a finger-ring bearing the name of Ahhotep in the collection of the Louvre Museum (E3297). In this region are localized PGE inclusions over a hard soldered join.

100 wt%. The Cu, Ag and Au ratios close to each PGE inclusion are similar to the ratios found either for the filler (for two PGE inclusions) or for the gold base plate (third PGE inclusion), which tends to support the spatial delimitation chosen for the PGE inclusions in the calculations. From the data obtained it is obvious that the hard solder alloy is produced by simple addition of Cu to the alloy used in the fabrication of the parts to be soldered.

Conclusion

The new detection system implemented in the AGLAE extracted beamline is well suited for the analytical study of Egyptian gold objects, particularly for the analysis of hard soldered joins and of PGE inclusions related to the alluvial origin of the gold. Despite the very variable thickness of the joining area and the very variable shapes and dimensions of the PGE inclusions, we were able to show that when fast analysis is performed in areas difficult to locate by visual observation, the analytical difficulties can be surmounted and the experimental setup described in this work becomes a powerful system of analysis. We could also show that the system is suitable to resolve complex situations, such as the overlap of a join with PGE inclusions.

Some difficulties were nevertheless encountered when processing the data. These difficulties are connected to the selection of the areas to be processed

for quantitative analyses. A compromise must be reached between selecting a high number of pixels necessary to obtain more accurate measurements and the precise delimitation of the areas of interest without adding extra information from the surrounding areas. The selection depends on the user's choice. The biggest limitation to achieve good detection limits is the study of very small areas of interest containing a very low number of pixels. The mapping monitoring system enables each pixel to correspond to a fixed charge. Therefore, for each map the detection limits are improved by expanding the selected area of interest.

For the Egyptian jewellery analysed, it was possible to show the addition of Cu to the gold base alloy to produce the hard solder alloy (further discussion is presented in Chapter 9.4). Concerning the PGE inclusions, each of them can be analysed separately to reveal the variety of their compositions, even within a same object. Many of them are binary and ternary alloys belonging to the expected Os-Ir-Ru system (Meeks & Tite 1980). Nonetheless, contrary to what could be expected from the few data published for Egyptian goldwork, some of our objects have PGE inclusions also containing Pt. The presence of this element might reflect use of gold from other origins.

References

For references see pp.185–91 at the end of this chapter.

Chapter 6.6

Double Dispersive X-Ray Fluorescence analysis for the provenance of gold

Martin Radtke & Uwe Reinholz†

When gold is analysed with synchrotron X-ray fluorescence (SRXRF), one of humankind's most fascinating materials meets state-of-the-art technology. SRXRF is among the most versatile tools for the characterization of materials. It combines high spatial resolution with good detection limits, allowing work in a normal atmosphere for the analysis of large objects that do not fit into sample chambers.

An important source of information about ancient gold is the examination of whole artefacts or samples with non- or minimal destructive techniques. Various different techniques such as inductively coupled plasma mass spectrometry (ICP-MS) and particle-induced X-ray emission (PIXE) have been applied to determine trace elements in gold, which can give important insights into provenance (Guerra & Calligaro 2004; Kovacs et al. 2009; Schlosser et al. 2012).

For the analysis of metals, all measurements with SR are non-invasive. The analysis of trace elements in gold with SRXRF, based on the detection of characteristic emission lines, is especially challenging, because of the L-lines of gold, their escape and sum peaks, as well as the Raman signal overlap with the signals from the trace elements which shall be determined. To overcome this problem, not all elements are measured simultaneously, which is the standard for XRF analysis. Instead, optimized conditions are used sequentially for specific groups of elements.

In this contribution, we demonstrate the potential of analysing trace elements in gold samples with double dispersive synchrotron radiation-induced X-ray fluorescence (D²XRF). The D²XRF setup was developed especially for the detection of platinum in gold. It is based on a pnCCD detector chip and a lithium fluoride 200 crystal combining the advantages of energy and wavelengths dispersive measurements (Radtke et al. 2016). While it was first developed for platinum, it is also useful for the detection of lead and bismuth in

gold. The advantages in using synchrotron radiation as excitation source are that the measurements are totally non-destructive and the energy can be tuned to optimize the measurement conditions.

D²XRF

The detection of trace elements with energy dispersive X-ray fluorescence (ED-XRF) is complex, when an element adjacent in the X-ray spectrum is present in high concentrations (Guerra et al. 2005, 2008; Radtke et al. 2013). If the trace element is the heavier one, the main element saturates the detector. When the trace element is lighter than the main element, then an excitation energy can be chosen below the edge of the main element, therefore the fluorescence for this element is not excited. However, in this case, Raman scattering is inevitably induced, which is very likely to overlap with the desired fluorescence signal (Sokaras et al. 2010). The analyses of platinum in gold provide a typical example of this problem. While the platinum is present in the ppm range, the gold accounts typically for more than 80 wt%.

There are two main advantages of using wavelength dispersive systems (WDS) for XRF analyses (von Bohlen et al. 2005). First, the energy resolution is much better than in energy dispersive systems. This is helpful to resolve peak overlaps which can occur for K- and L- lines, for example arsenic K-lines and lead L-lines, and makes it easier to resolve neighbouring elements such as gold and platinum. Furthermore, if the excitation energy is chosen properly, like in our case, it is possible to resolve the overlap of Pt-L_{α1} line with the Au Raman scattering. The second big advantage is, that the detector does not saturate with unwanted information, as not all lines are analysed simultaneously.

Of course, there are as well drawbacks. Compared to an energy dispersive system, the acquisition time

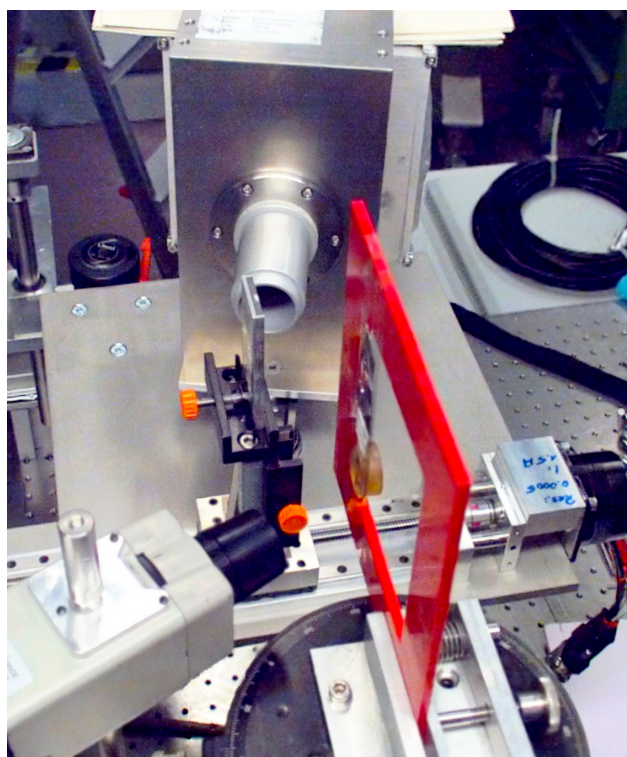
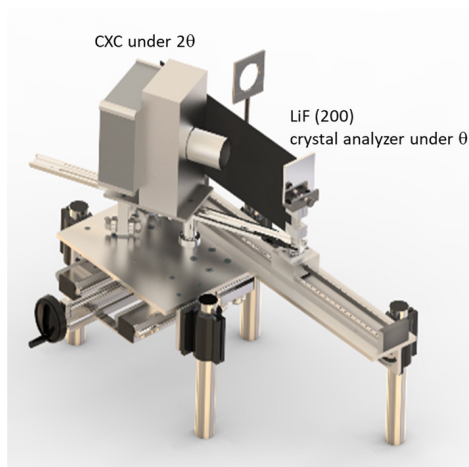


Figure 6.20. The developed setup for D^2XRF measurements. 3D model of the D^2XRF apparatus (top), set-up in use with sample holder (above). Different fluorescence energies are reflected under different angles from the crystal and therefore are detected on different positions on the pnCCD.

is significantly higher, because each element must be measured separately. Another disadvantage in traditional WDS systems is the restricted efficiency due to the collimators used to define the θ - 2θ geometry. These disadvantages can be overcome by using several detection channels in parallel and more sophisticated

geometries, like the Rowland circle (Beckhoff et al. 2007). Another possibility is to use a newly developed double dispersive setup, the so-called D^2XRF . This is based on flat crystal geometry and uses an energy dispersive pnCCD chip for detection. This set-up realizes the easiest configuration for a wavelength dispersive measurement. The sample is excited with a pencil beam and the characteristic lines are dispersed via a crystal onto a CCD chip.

The setup is illustrated in Figure 6.20. While the main dispersion is done by the crystal, the additional energy resolution of the used pnCCD chip allows an effective suppression of the background, resulting in strongly improved detection limits making the use of additional collimators unnecessary. Depending on the chosen geometrical distances, not only one fluorescence line, but a whole energy range of approximately 1000 eV, can be detected simultaneously.

Crystal

To maintain the easy geometry, a flat crystal was selected. There are two important parameters influencing the selection of the crystal type. The reflectivity determines together with the intensity of the exciting radiation the achievable count rate. The most important parameter is the d-spacing according to Bragg law as the geometry and the achievable energy resolution are strongly influenced by this parameter. We decided to use a LiF200 crystal with $2d = 4.027$ Angstrom. LiF200 is described as the best general crystal, which combines high intensity and high dispersion (Kirz & Vaughan 1985).

Energy Dispersive CCD Detector

A silicon-based energy-dispersive pnCCD chip (Meidinger et al. 2006) was used as detector. This chip serves as well as detector in the colour X-ray camera (CXC), which was jointly developed by PNSensor GmbH (Munich, Germany), the Institute for Scientific Instruments GmbH (IFG, Berlin, Germany), the BAM (Bundesanstalt für Materialforschung und -prüfung, Berlin, Germany), and the Institut für Angewandte Photonik e.V. (IAP, Berlin, Germany) (Ordavo et al. 2011; Scharf et al. 2011). While the standard operation of the CXC allows to measure two-dimensional element distributions or the measurement of spatially resolved XANES distributions, the use of the chip without optics opens unique possibilities in transmission geometry as well (Boone et al. 2014). The pnCCD chip has a sensitive area of 12.7×12.7 mm² consisting of 264×264 pixels of 48×48 μm^2 . The device has high quantum efficiency (95–30%) for photons with energies between 2 and 20 keV. The lowest energy limit is determined by the 50 μm beryllium window, the highest one,

and by the 450 μm chip thickness. Detector readout is performed in a column-parallel, split-frame method in which each half of the illuminated pnCCD chip is physically transferred in 50 μs to a dark frame storage area. This reduces illumination during further signal processing by two dedicated CAMEX chips for each half of the pnCCD chip, effectively splitting the total illuminated chip area in four quadrants. Event analysis is performed to determine the centre of gravity and total deposited energy for each incident photon, as the corresponding electron charge cloud created in the detector material can be distributed over multiple pixels depending on the photon energy and point of incidence with respect to the pixel boundaries. The pnCCD is therefore a single photon counter. Full detector readout occurs at a frequency of 1000 Hz.

Beamlines

First experiments were performed at BAMline (Riese-meier et al. 2005) and final measurements on Egyptian gold foils were carried out at mySpot beamline (Paris et al. 2007), the high energy beamlines for XRF measurements at the electron storage ring BESSY-II at Helmholtz-Zentrum Berlin (HZB, Berlin, Germany). The primary radiation source of this beamlines is a 7 T wavelength shifter. The energy of the X-ray beam can be tuned by a double-crystal Si(111) monochromator (DCM). A double multilayer monochromator (DMM) or a mirror is used for suppression of higher harmonics.

Samples were mounted under 45° and the crystal under 90° in relation to the incoming beam. The position of the detector was determined by the Bragg angle at the analysed energy to achieve the classical θ - 2θ geometry. The distance between the crystal and the detector was chosen in a way that the observed energy region was sufficient to analyse all lines of interest simultaneously. Typical distances were 10 cm from sample to crystal and 15 cm from crystal to the detector. The horizontal size of the beam was varied between 5 μm and 1 mm to determine the influence of the beam size on the achievable energy resolution. The energy resolution of the monochromatic radiation was in the best case $\Delta E = 2.4$ eV. The results are discussed below.

Data processing

To achieve the final wavelength dispersive spectra, a two-step process for data processing is necessary. In a first step, measured data are saved in a hyper-spectral data cube with $264 \times 264 \times 1000$ channels, were '264 \times 264' is the above-mentioned pixel number of the CCD chip and '1000' the quantity of channels for the energy-dispersive spectra in each pixel. In the first step, all spectra of one column are added, resulting in a matrix of 264 spectra in the order of 1000 channels.

Each of the 264 columns represents one energy interval $\Delta E = 2.4$ eV of the wavelength dispersive spectrum. The second step is to extract the necessary information from the energy dispersive spectra; the events in the matching energy range are added. Thereby the choice of the adequate region of interest (ROI) is fundamental. In order to determine the background more precisely, it is also possible to fit the characteristic lines in the sum spectra for each column.

D²XRF performance

To determine the achievable energy resolution under different conditions a 1 mm thick pure copper plate was used. While the distances between sample, crystal and detector are determined by the energy range, which should be measured simultaneously, the parameters which influence the energy resolution were the beam size on the sample (Fig. 6.21a,b) and the order of the Bragg reflection from the crystal (Fig. 6.21c). The used LiF200 crystal shows first and second order Bragg reflections. Of course, the use of smaller beams and higher-order reflections reduces count rate resulting in prolonged measurement times or worse statistics. Therefore, all measurements were done with the full available beam.

The minimum detection limit (MDL) for platinum in gold was determined with a reference material for fine gold from the Royal Canadian Mint (Ottawa, Canada), RM8058, with a certified Pt concentration of 40.8 ppm. Samples NA-Au-30 and NA-Au-31 from Aurubis AG (Hamburg, Germany), with a known Pt concentration of 58 and 1152 ppm, respectively, served as control samples.

For the Pt measurements, the choice of the optimal excitation energy E_0 was crucial. The lower limit for E_0 was the L3 absorption edge of Pt 11564 eV, and the upper limit was restricted by the position of the Raman scattering, which must be completely separated from the Pt fluorescence line. To fulfil these conditions an excitation energy just above the Pt edge was selected. Figure 6.22 shows two spectra, which are measured on the 58 ppm NA-Au-30 standard at the BAMline. In Figure 6.22a, the energy dispersion of the pnCCD chip is not used, while in Figure 6.22b the use of the energy dispersion of the pnCCD chips makes it possible to distinguish all features of the spectra: Pt, Au and Raman lines are clearly visible. Gold lines are present, because the third harmonic was not fully suppressed in the exciting beam.

The motivation to build the D²XRF set-up was the improvement of MDL. In order to enhance the conditions, we transferred the set-up to the mySpot beamline, where a higher flux is available and a mirror

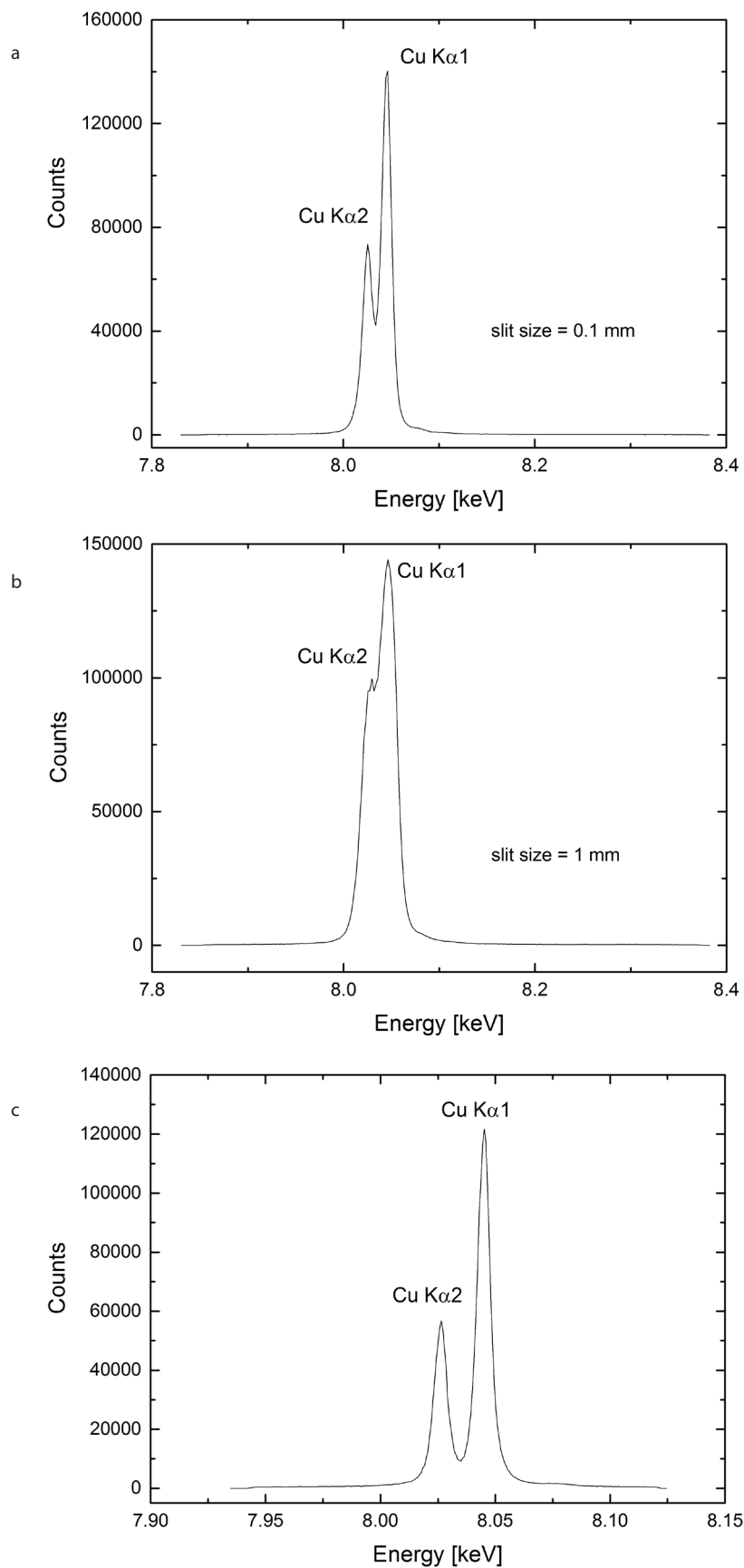


Figure 6.21. Comparison of the Cu K α peak for (a) 0.1 mm and (b) 1 mm beam size. The degradation of the energy resolution from 12.6 to 18.4 eV FWHM is clearly visible. (c) The Cu K α peaks for 1 mm² beam size using the second-order reflex. The energy resolution of 7.7 eV FWHM allows the complete separation of the 20 eV peaks. Reprinted with kind permission from Radtke et al. (2016).

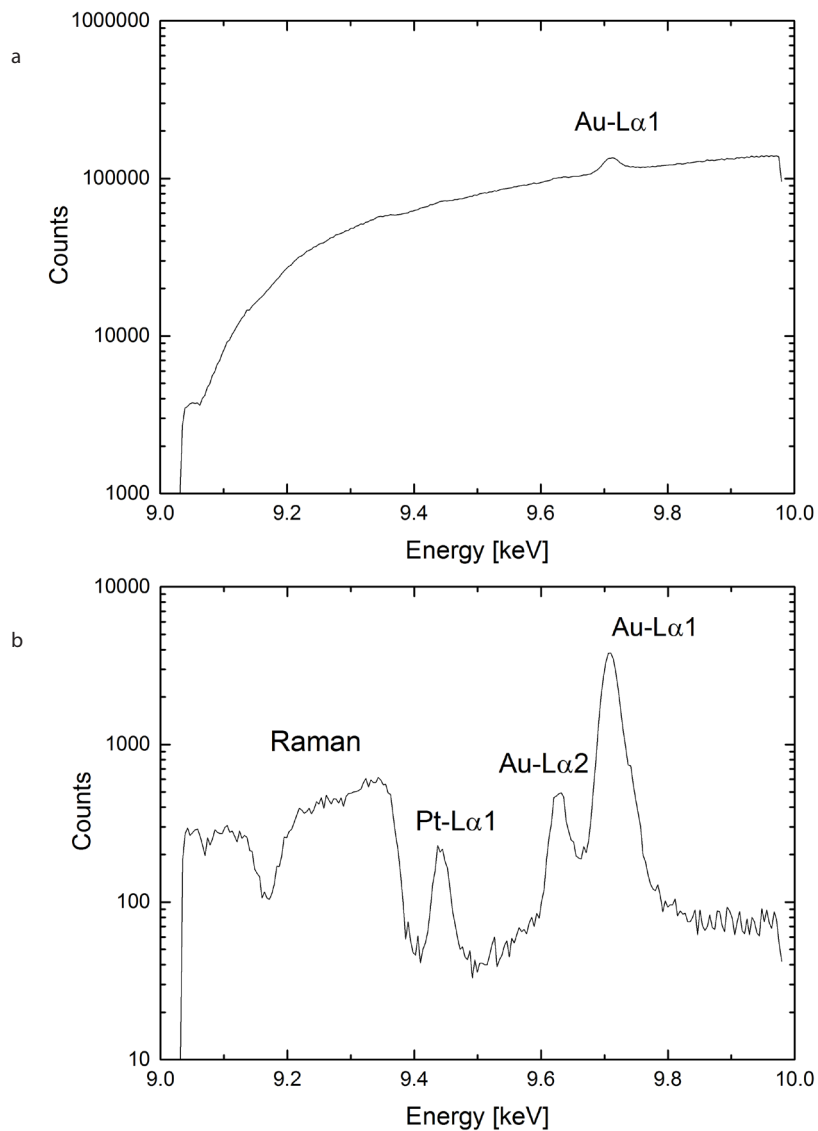


Figure 6.22. The effect of the energy dispersion of the pnCCD chip. Both diagrams show the measurement of an Au standard containing 58 ppm Pt at the BAMline: (a) without energy dispersion only the highest Au peak is visible; (b) with energy dispersion all spectral features (fluorescence peaks and Raman scattering) are clearly visible and distinguishable. Reprinted with kind permission from Radtke et al. (2016).

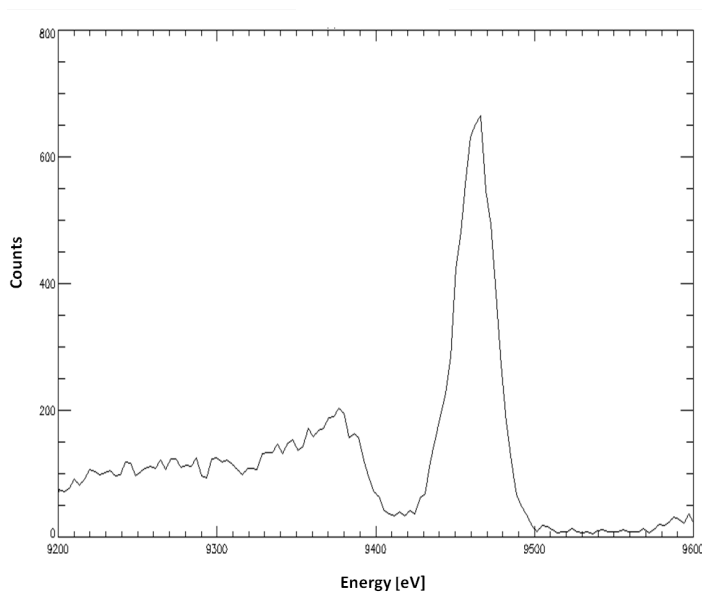


Figure 6.23. D²XRF spectrum of NA-Au-30 at the mySpot beamline. For a measurement time of 1000 s an MDL of 0.9 mg/kg was achieved.

placed before the DCM suppresses the harmonics. The D²XRF spectrum of Figure 6.23 were measured with this set-up. The absence of the Au L-lines is obvious. Additionally, the considered ROI was optimized for the Pt-L_{a1} peak to suppress the unavoidable contribution of the Raman scattering. As result, an MDL of 0.9 ppm was reached, which is to our knowledge the best value for non-destructive analysis of Pt in Au.

Application

The first application of the D²XRF system concentrated on the analysis of Pt in Egyptian gold foils. The excellent MDL obtained for the analysis of Pt using D²XRF allows the determination of low Pt contents in gold alloys, even when very thin gold items were analysed (Radtke et al. 2016).

The presence of platinum in gold is representative of the exploitation of alluvial deposits, and high contents of this element have been used to provenance particular gold productions. However, among the scarce publications on Egyptian gold leaf, only one, which concentrates on gilded wood samples from the tomb of Tutankhamun (Rifai & El Hadidi 2010), pointed out the presence of Pt in the alloys.

In this work, two gold foils from gilded wood objects from the tombs excavated by John Garstang at the southern edge of the so-called North Cemetery at Abydos were analysed by D²XRF (these objects are discussed in Chapter 8.6). The concentrations of the major elements in the different gold alloys were analysed by SEM-EDS, PIXE and μ XRF (Tissot et al. 2015).

The Pt concentrations in the two analysed Egyptian foils and in a gold alloy of known composition ('RUS' containing 192–314 ppm, determined by ICP-MS in solution mode and laser ablation mode) were calculated with the rule of proportion using RM 8058 certified gold reference material containing 40 ppm of Pt (NIST RCM FAU8 Fine Gold). Signals were normalized prior to the calculations to the total intensity of the Raman scattering in the energy range from 9200 to 9350 eV. The Pt signal was summarized in the energy range from 9420 to 9460 eV prior to the calculations. The D²XRF measurements of control sample RUS yielded 242 ppm. The presence of Pt could be verified for the two analysed Egyptian foils. The concentrations were quantified to be 339–340 ppm, confirming the alluvial

origin of the gold. The results obtained prove the possible use of Pt as a provenance indicator even for very thin foils, but such small amounts of Pt in very thin gold foils cannot be measured with any other currently available non-destructive technique.

Conclusions

The newly developed D²XRF set-up, which consists of an energy dispersive pnCCD chip as detector and a flat crystal for wavelength dispersion, allows with a very simple geometry the detection of highly resolved wavelength dispersive X-ray fluorescence spectra with 264 channels. The simultaneously detected energy range is typically in the range of 630 to 1000 eV, which means a resolution of 2.4 to 4 eV/channel. Energy resolution and detected range can be easily modified by changing the distances from sample to crystal and from crystal to pnCCD, respectively.

The ability to use energy-resolved single-photon counting with the pnCCD makes the use of additional collimators unnecessary and results in spectra with effective reduced background. The ability of D²XRF was demonstrated by the excellent results obtained for the analysis of Pt in thin gold foils, a difficult analytical assignment. Currently, amounts of Pt in gold alloys with MDL of 0.9 ppm can only be measured non-destructively by D²XRF.

The concentrations of Pt present in the Egyptian gold foils from Abydos could be quantified, evidencing the use of alluvial gold. D²XRF can be applied to other analytical challenges like the non-destructive detection of lead and bismuth in gold. This can be an indication to identify modern electrolytic refined gold. An example for this is the result of the investigation of the gold treasure of Bernstorf (Radtke et al. 2017). The D²XRF set-up is routinely available at the BAMline and mySpot beamline at BESSY-II.

Acknowledgement

We thank HZB (Berlin, Germany) for the allocation of synchrotron radiation beamtime.

References

For references see pp.185–91 at the end of this chapter.

Chapter 6.7

3D imaging, colour and specularity of an Egyptian Scarab

Lindsay MacDonald & Mona Hess

The analysis of Egyptian gold items shows evidence for polychrome effects, using not only coloured materials but also several gold alloys with different copper and silver contents. The latter necessitate an effective method for analysing the colours present in the object – knowing that in some alloys atmospheric corrosion may alter the surface, and ‘hide’ the original colour.

The physical surface of an artefact is influenced by decorative techniques, evidenced by the presence of tool marks, and by wear-marks, giving indications about the object’s intended function and possible re-use. Scientific visual analysis requires images of high quality, at different scales and depths. For this reason, we wished to investigate the capability of 3D image acquisition to represent the colour and surface detail of materials used in the production of Egyptian gold jewellery.

The object selected for this pilot study is a small scarab of engraved steatite set in a gold band, from the UCL Petrie Museum of Egyptian Archaeology (UC11365, Fig. 6.24). Dated to the Late Middle Kingdom (1850–1750 BC), it is inscribed in hieroglyphs on the underside with the personal name and title ‘estate overseer of the granary Iufseneb’ within the scroll border. The hole of 2.8 mm diameter drilled through the centre suggests that it may have been suspended on a cord worn around the wrist or neck, or fitted onto a metal rod in a ring mounting, and used as an administrative seal in clay tablets or in wax on papyrus.

3D digitization

Different methods of 3D acquisition were studied for their ability to represent the original colours and surface details for visual inspection of toolmarks and other material properties. The scarab poses particular challenges for imaging due to its characteristics: a small object, with finely engraved inscription, the

back is curved and polished to a semi-gloss finish, and the encircling chased gold band has a high metallic specularity.

Photogrammetric method

The scarab was placed on a rigid black card, onto which were affixed a number of retro-reflective targets for geometric camera calibration (Fig. 6.25). Around 80 images were taken using a fixed Nikon D3200 camera with 105 mm macro lens, from various angles by rotating the tray, and by turning the scarab onto its side. Flash lighting was diffused by soft boxes and reflectors pointed towards the ceiling. The image set was processed with an in-house software pipeline at UCL, enabling a dense and accurate 3D point cloud to be generated (Ahmadabadian et al. 2013). After geometrically correcting (‘undistorting’) the images, by estimating parameters from the camera’s chip size and focal length, the approximate 3D coordinates were extracted from the images. A photogrammetric bundle adjustment with the relative orientation parameters of each camera position enabled the scale factor to be estimated and then applied to the camera locations and 3D coordinates of the scarab surface. These data were input into the processing software to generate a dense point cloud.

As the scarab needed to be repositioned during acquisition in order to obtain images of the whole object, each ‘scene’ was reconstructed separately, then cleaned and fused together during post-processing. The resulting 3D surface geometry shows a greater variance, or level of noise, than that of a laser scanner (compare Fig. 6.27 middle to Fig. 6.28 middle). However, this method of photogrammetric imaging, including a colour chart and subsequent calibration, enables the acquisition of accurate colour data, which is essential for cultural heritage applications. If a mesh is reconstructed from the point cloud, the colour texture



Figure 6.24. Six views of scarab UC11365, Petrie Museum. Dimensions (in mm) 26.7 (W) × 18.6 (H) × 11.4 (D). Photographed with a Nikon D200 camera with Nikkor 200 mm macro lens, illuminated by 16 flashlights in a circular ring.



Figure 6.25. Photogrammetric imaging setup with scarab UC11365 on target board.

obtained from the imagery can then be reprojected onto the surface giving a high resolution rendering even on a lower resolution geometric structure.

3D colour laser scanning

A 3D colour laser scanner at UCL has been used extensively for digitization of museum objects, and for traceable and repeatable production of metric surface models. It delivers 3D RGB point data at a sampling

interval of 0.1 mm (100 μm) with an absolute accuracy of 0.025 mm (25 μm) over the object surface (Hess & Robson 2010). Twenty-six separate scans of the scarab were made, with the object turned to many different orientations to ensure that all surfaces were captured. The corresponding point clouds were merged to produce a 3D representation with c. 402,000 points.

Photometric stereo

The dome imaging system at UCL enables sets of images of an object to be taken with illumination from different directions (Fig. 6.26). A hemisphere of 104 cm diameter is fitted with 64 flash lights, and calibrated so that the geometric centroid coordinates of every light source are known to within 3 mm (MacDonald et al. 2015). A Nikon D200 digital camera at the 'north pole' captures a series of 64 colour images, each illuminated from a different direction and all in pixel register. This enables the object to be visualized from the fixed viewing angle of the camera, i.e. vertically from above, for many different angles of incident light. Image sets captured by the system can be visualized for a directional light source by the polynomial texture mapping (PTM) technique, which has numerous applications in archaeology and cultural heritage (Earl et al. 2010).

Six sets of images from the UCL dome were used to reconstruct the 3D surface of the scarab by

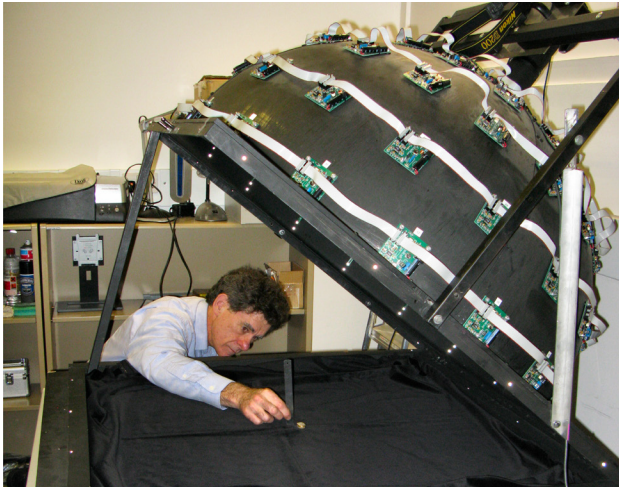


Figure 6.26. Positioning scarab UC11365 on the baseboard of the UCL dome.

the photometric stereo method (MacDonald & Robson 2010), by determining the surface normal vector at each pixel then integrating the set into a consistent surface. An adaptive method was developed to find an optimal subset of intensities from all 64 candidates at each pixel, by sorting them into order and selecting a range between the shadow and specular regions, followed by regression over this subset for an accurate estimate of the normal vector (see below). The height

field was reconstructed as a digital terrain map by projecting the surface gradients onto Fourier basis functions to ensure integrability (MacDonald 2015), then exported as a point cloud for 3D visualization.

Evaluation of 3D reconstruction methods

The various 3D representations were evaluated for visibility of toolmarks and other material treatments. The 3D coloured point clouds produced by the models were rendered for display.

The photogrammetric method showed realistic colour and significant detail (Fig. 6.27), with a resolution of approximately 20 pixels/mm (50 μm sampling). The overall geometry was accurate but was compromised by holes in the 3D point cloud from missing data due to specular reflection from the gold during the acquisition process. There was also a noticeable level of surface noise in the reconstruction.

The 3D colour laser scanner produced good geometric accuracy, but the rendition of surface detail was poor (Fig. 6.28). Even though the scanner was expected to show sufficient details with a sampling distance of 100 μm , i.e. a spatial resolution of 10 points/mm, it did not meet the expectation, and revealed less detail than shown by magnification with a hand lens. The finest surface feature that can be wrought on an artefact by a craftsman with manual techniques is approximately 40 μm in width, to capture which the scanner should be



Figure 6.27. (left) Photogrammetric reconstruction; (centre) without colour. Although the colour was close to original object, the method produced a significant quantity of surface noise and holes in the 3D point cloud. (right) Detail of scarab top, showing erroneous cut by craftsman.



Figure 6.28. 3D point cloud generated by the colour laser scanner, showing the redness caused by non-optimal laser wavelengths.



Figure 6.29. 3D reconstruction from photometric normals produced a very dense point cloud with outstanding detail of surface features.

able to resolve 20 μm , i.e. 50 pixels/mm or 1250 pixels per inch (MacDonald 2010). Moreover, the rendering of surface colour shows less fidelity to real colour than with a camera, because the monochromatic sampling of the reflectance spectrum by the three lasers leads to severe metamerism (MacDonald 2011).

The photometric stereo reconstruction in 3D was accurate over the rounded back of the scarab for a range of $\pm 45^\circ$ from the vertical (Fig. 6.29), and gave excellent rendering of fine detail, especially helpful for reading the hieroglyphs on the underside. Comparison of the 3D point cloud produced by the photometric stereo technique with the reference point cloud from the laser scanner (Fig. 6.30) shows that the mean error was less than 0.25 mm, but around the sides and the gold band, the errors were larger in the range 0.4 to 0.7 mm.

The results of the qualitative evaluation of the three reconstruction methods are summarized in Table 6.8. The laser scanner gave results that were excellent in terms of geometric accuracy, because of the precision of its coordinate measuring machine (CMM), but its results were inferior in both colour and spatial resolution to the other techniques which derived 3D from sets of photographic images (MacDonald et al. 2014). For all methods the time required to set up and digitize the object was typically about an hour, followed by a day or more of operator time and/or computing time to process the data to produce the final 3D representation. In terms of portability, the photogrammetric method was best by far, because it required only a camera and aboard with targets affixed, whereas the photometric stereo method relied on the dome structure to provide the camera support and multiple sources of illumination.

Colour of gold

There is nothing absolute about the colour of any object surface: it changes continually with illumination and orientation. Colorimetry specifies the colour as the product of the illuminating power by the reflectance factor of the surface by the sensitivity of the observer, integrated over all wavelengths of the visible spectrum. This is the basis of the ubiquitous CIE system (Colorimetry 2004), but it relies on the assumption that the surface is perfectly matte so every point reflects the incident light equally in all directions, i.e. that it is Lambertian. In fact, almost

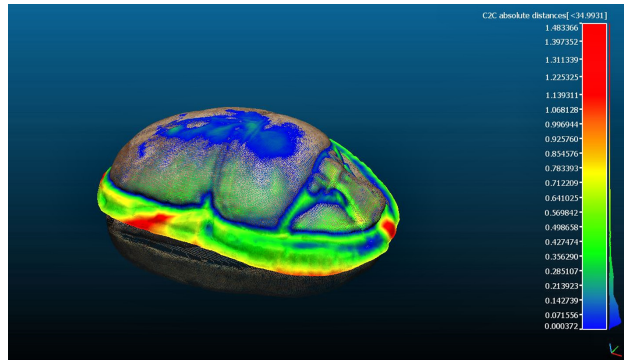


Figure 6.30. Comparison of point cloud from photometric stereo reconstruction with point cloud from laser scanner, using the CloudCompare utility.

all real materials exhibit some angular dependence in the way they reflect light, and this behaviour must be taken into account when modelling appearance, by adding a gloss component to the underlying diffuse colour. The added light may appear as a sheen over the surface or as localized specular highlights, but its effect is to modulate the lightness and thereby to change the apparent colour.

This is especially true of gold, which combines glitter, specularity and sheen over a wide range of angles to give it a uniquely lustrous quality that sets it apart from ordinary materials. To specify the colour of gold only by a single colorimetric triplet, or even by a single reflectance spectrum, would be dull indeed. As a demonstration, the gold band around the scarab was measured with an Xrite i1Pro spectrophotometer. The instrument illuminates the sample at 45° and analyses the radiation reflected perpendicular to the surface, averaging the rays over a circular beam area of diameter 3.5 mm. The spectral reflectance distributions from 10 successive measurements are shown in Figure 6.31. The characteristic rise in reflectance factor between 480 and 540 nm corresponds to an energy band at 2.3 eV in pure gold where free electrons in the d-band can make the transition to unoccupied states in the conduction band (Saeger & Rodies 1977).

It is evident in the set of measurements that, although the shape of the curve remains the same, the magnitude of the reflectance varies by a factor of 1.5. This can be explained by the measurement geometry

Table 6.8. Qualitative comparison of 3D representations.

| Technology | Colour | Geometry | Resolution | Cost | Portability |
|--------------------------|--------|-----------|------------|--------|-------------|
| Photogrammetric method | Good | Good | High | Low | Good |
| 3D colour laser scanning | Poor | Excellent | Medium | High | Impossible |
| Photometric stereo | Good | Poor | High | Medium | Poor |

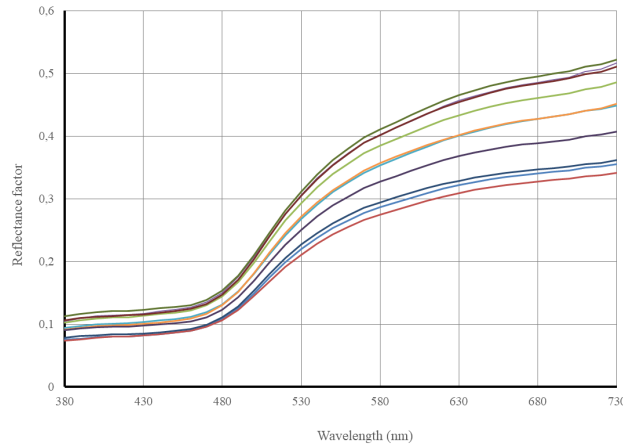


Figure 6.31. (top left) Measurement of gold band on scarab; (bottom left) underside of instrument, showing measuring aperture; (right) set of reflectance spectra.

of the instrument, which is designed for measurement of flat surfaces, such as prints on paper, which may or may not be glossy. The 45° angle of incident light and 0° angle of view for the sensor ensure that the specular component of reflection is avoided as far as possible. But when the instrument is removed and then brought back each time with the aperture in a slightly different position over the relief surface of the gold, a different distribution of scattered light reaches the sensor and hence the reading changes.

The majority of variation in the measured colorimetric values is in the luminance, not the colour: in CIE 1931 chromaticity coordinates the mean and standard deviation in x, y, Y are $[0.4076 \pm 0.0013, 0.4166 \pm 0.0012, 30.19 \pm 4.39]$ and in $L^*a^*b^*$ the corresponding range is $[61.65 \pm 3.83, 3.28 \pm 0.46, 36.26 \pm 1.95]$. The latter are plotted in Figure 6.32, showing lightness (L^*) vs chroma (C^*) and the chromatic plane a^*b^* . The standard D65 daylight illuminant was used for computation of the $L^*a^*b^*$ values.

Specularity of gold

The scarab was photographed under the illumination dome in six different orientations, with a Nikkor 200 mm macro lens giving a spatial resolution of approximately 66 pixels/mm, i.e. each pixel representing $16 \mu\text{m}$ on the object surface.

All 64 images in the set from the dome are in pixel register, so each pixel may be regarded as a vector of 64 intensity values, each representing the amplitude of the light reflected from that point on the surface toward the camera for the angle of incidence corresponding to the position of the lamp. The distribution of these 64 intensity values gives an indication of the type of surface (Fig. 6.33).

A notable characteristic of gold, and indeed of all shiny materials, is that it reflects strongly in the specular direction. So in the pixel vector a few intensity values are much larger than the others, corresponding

to positions where the surface normal is close to the bisector of the angle between the illumination vector (toward the light) and the view vector (toward the camera). This results in images with high dynamic range where a few pixels may be 100 times greater in value than the majority. In the dome, images are captured and processed as linear intensities with 16-bits per channel (range 0–65535), setting the lens aperture

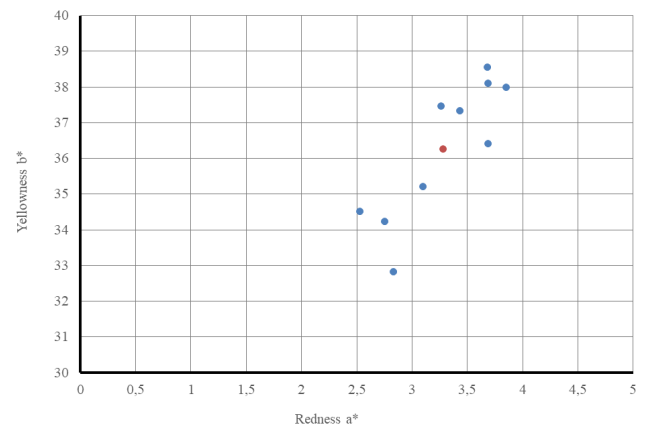
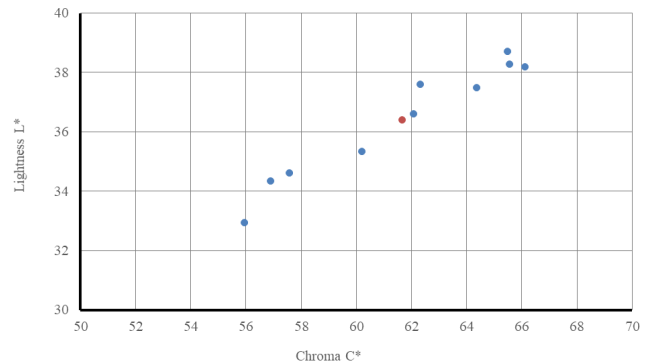


Figure 6.32. Colorimetric coordinates of 10 measurements at different positions on the gold band around the scarab (mean shown in red).

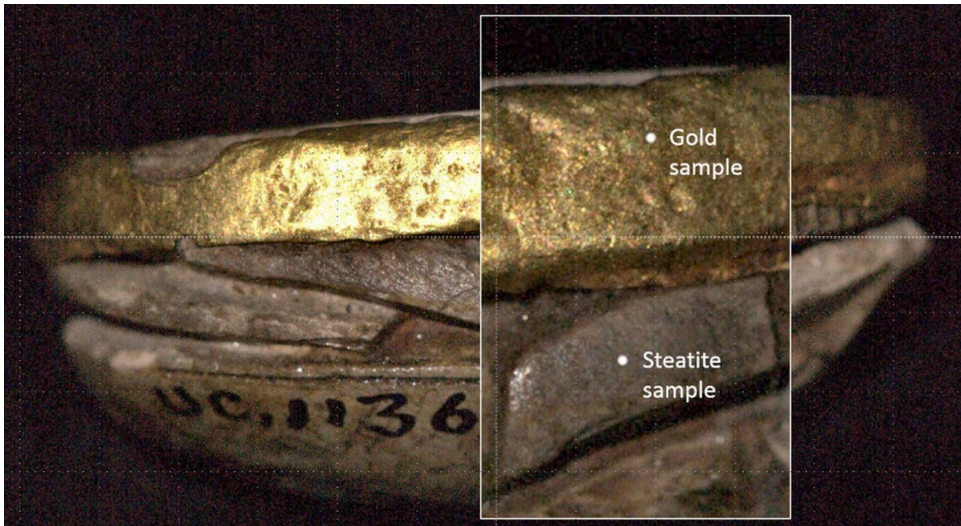


Figure 6.33. Image of left side of scarab, with enlarged detail showing sampling locations for gold and steatite.

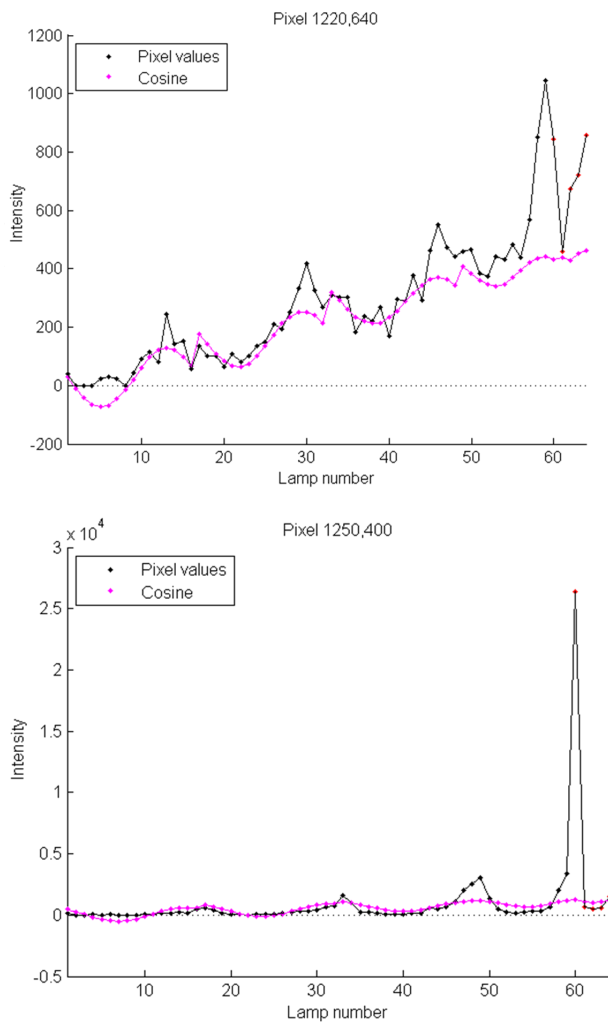


Figure 6.34. Intensity distributions from 64 lamps for a single pixel for: (top) steatite; (above) gold; sampled at positions shown in Figure 6.33.

to $f/8$ to avoid over-exposure. Figure 6.34 (right) shows the intensity distribution for a single pixel on the gold band. The maximum value is over 26,000 and seven are in the range 1000–4000, but most others are less than 300. The magenta curve shows what the intensities would be for a perfectly matte (Lambertian) surface with the same albedo and normal angle. It is clear that the specular peaks are much greater in intensity than the cosine, but all other values are lower. Thus, the metallic gold surface is generally darker than the diffuse equivalent, except for a few bright highlights.

The processing method is to identify from the sorted intensity distribution of a 3×3 pixel neighbourhood a limited range of values between the shadow and specular regions, which are taken to be representative of the non-specular 'body colour' of the object. Then, using the principle of 'shape from shading', a regression is performed on the corresponding lamp vectors to estimate the most probable direction of the surface normal vector at that pixel (MacDonald 2014). The albedo is the magnitude of the normal vector, and its appearance is surprisingly dark (Fig. 6.35 left). The normal vectors are represented in Figure 6.35 (right) by the conventional false-colour coding scheme with X components in red, Y in green and Z in blue.

The second stage of processing is to determine the specular vector at each pixel, i.e. the direction of maximum specular reflectance. First, the specular quotient (ratio) is calculated between the actual intensity value and the diffuse component for each lamp. This would be the black value divided by the magenta value for each of the 64 points in Figure 6.35. For semi-matte surfaces the quotient values are typically in the range 0.5 to 2.5, but for high gloss and shiny metallic surfaces they may be very large. In this case the gold band has a bright lustre rather than a brilliant shine,

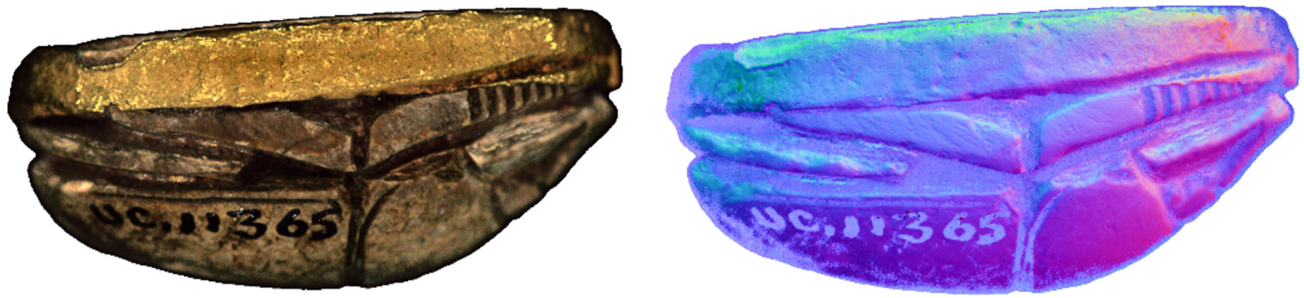


Figure 6.35. Image components derived from processing the original set of 64 images: (left) albedo, (right) normals.

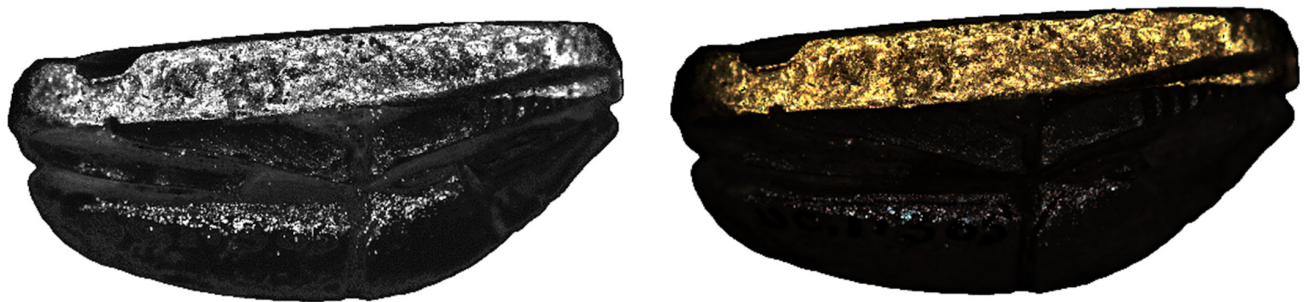


Figure 6.36. Image components: (left) specular quotient, (right) specular colour.

with a maximum specular quotient value of 67.5 and mean of 11.2 with standard deviation 2.7 (Fig. 6.36).

One might suppose that the specular angle should be exactly double that of the normal, as it would be for a perfect mirror surface, but in fact there is a great deal of variation. This is caused by granularity of the metallic gold and surface imperfections, such as scratches and dust, which cause perturbations in the direction of the strongest reflectance. The scatter is clear when the specular angle relative to the Z-axis is plotted against the normal angle for 10 000 points randomly selected throughout the gold band region of the image (Fig. 6.36 left). Instead of lying along the line of slope 2, they are spread over a wide range of angles, both greater than and less than the normal angle. The horizontal lines of red dots in the figure are computational artefacts, where the specular vector lies exactly toward the lamp, in this case in the second tier of the dome with an incident angle of approximately 26° .

The specular colour at each pixel is computed from the colours of the selected specular values, using the same weighting factor derived from the specular quotient. The result is shown in Figure 6.36 (right) and it is apparent that the specular colour of the gold band is lighter and less saturated than the albedo colour in Figure 6.36 (left). The relationship of the angles can be explored by plotting corresponding values for a

random selection of 10,000 points throughout the area of the gold band. In the 3D scatter plot of Figure 6.37 (right) the albedo colours are shown as black dots and the specular colours as red dots in a normalized R,G,B cube. Also shown are lines representing the first principal component of each cluster of points, which tend in different directions. The albedo (body colour) is darker, whereas the specular colour is lighter and closer to the neutral axis, although the specular data is more scattered. Both are below neutral on the blue axis, meaning that both are yellowish. The two vectors in RGB colour space (denoted by the red and black lines in Fig. 6.37 right) may be considered as equivalent to the interface and body colours identified by Shafer in his proposal for a dichromatic model of reflection from a material surface (Shafer 1985).

The angular distribution of the specular quotient around the specular peak has been found for a variety of materials to be modelled well by a modified Lorentzian function, which takes the form of a curved peak plus a linear flank (MacDonald 2014). The parameters of the curve are determined for each pixel by fitting the distribution of specular quotient values in the polar plane (Fig. 6.38 left). The function generated by the mean parameter values over all pixels in the gold band has an angular width at half-maximum amplitude of 17.5° (Fig. 6.38 right). This is in good

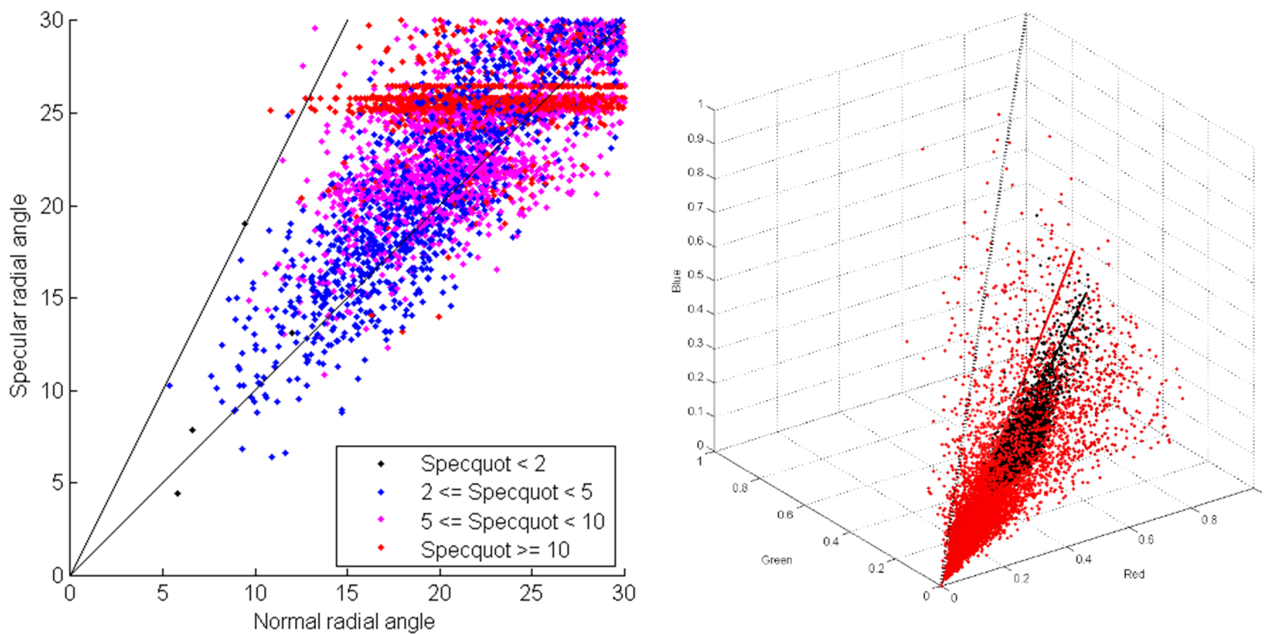


Figure 6.37. (left) Scatter plot of specular vector angle vs normal vector angle; (right) specular vs albedo colours for 10,000 random points in gold band.

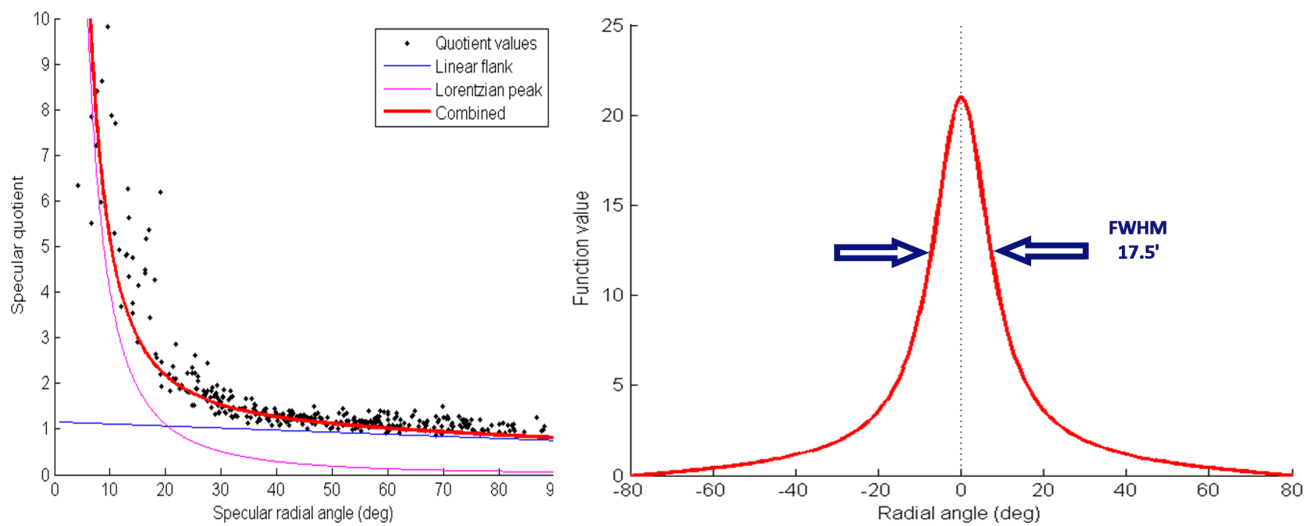


Figure 6.38. (left) Fitting of flank and Lorentzian function through specular quotient values; (right) function generated with mean of parameter values.

agreement with values found in other studies of gold (Lee et al. 2006). Note that the specular reflection is not restricted mirror-like to the specular peak angle, but extends over a wide range of angles, which gives gold its characteristic lustre. Without this broad flank in the specular reflectance distribution, the rendering of gold would be darker with scattered pinpoint highlights and would not be realistic.

The complete model for rendering images under a single light source adds the diffuse and specular terms. This gives images that are realistic in appearance and a good match to actual photographs. Figure 6.39 juxtaposes the actual photographic image taken in the dome illuminated by lamp 60 (high up in the dome to the right) with the rendered image illuminated from the same angle. Although not identical, the two are



Figure 6.39. (left) Original photograph and (right) rendered image, both illuminated from same hemisphere coordinates as original lamp.

similar in terms of the overall tonality and distribution of highlights. Because the model is based on a continuous function of angle, images can be rendered for a virtual light source at any position in the hemisphere.

Thus, the colour of gold can be represented as a sum of two components: a dark reddish-yellow 'body colour', the albedo corresponding to the diffuse reflectance from the material, plus a bright yellowish highlight with a broad angular distribution around the specular peak. Multiple reflections from facets on the surface may cause the spectrum of the reflected light to be multiplied and hence to appear darker and more saturated. When the object is diffusely illuminated, with incident light from many directions, the characteristic golden radiance suffuses the whole surface and brings it to life.

Acknowledgements

This study was facilitated by the European COST Action TD1201 Colour and Space in Cultural Heritage (COSCH). Some of these results were presented previously in a conference paper (MacDonald et al. 2014). Thanks especially to colleagues in the 3DIMPact research group Stuart Robson and Ali Hosseinaveh Ahmadabadian, who carried out the 3D laser scanning and the point cloud processing and the photogrammetric reconstruction (Ahmadabadian et al. 2013).

References

For references see pp.185–91 at the end of this chapter.

Chapter 6.8

The corrosion of precious metals: the case of Egyptian goldwork

Isabel Tissot & Maria F. Guerra

Corrosion is the degradation of a material, often a metal, resulting from a chemical or an electrochemical reaction with its environment. These irreversible processes lead to changes in the metal properties (including optical properties related to aesthetics such as lustre, colour etc.) and, depending on their nature and extent, they may result in a significant loss of material. Some metals are chemically more reactive in burial, indoor and outdoor environments. For example, copper and iron corrode more easily than silver and gold; this is the main reason for the latter being called noble metals.

The tendency to undergo a corrosion process depends primarily on the metal reactivity to oxidize. When metals are exposed to air and to pollutants in the presence of an electrolyte (related to the atmospheric humidity), they undergo an atmospheric corrosion process, such as tarnishing and chloridation by reaction with sulfur and chlorine compounds, respectively. To understand the corrosion processes and their influence on the different properties of metals, several investigations can be developed. In these studies, the identification of the corrosion products and the description of the corrosion mechanisms are considered. These studies are fundamental to define and implement corrosion control and preservation measurements.

Considering the study of ancient silver and gold alloys, there are several references dating back to the 1950s and even earlier (Costa 2001). The studies on silver corrosion are more numerous and recurrent than those of gold corrosion. In fact, studies on the corrosion of gold alloys emerged in the 1980s in the domains of modern jewellery (Courty et al. 1991; Carvalho et al. 2009) and dentistry (Fioravanti 1988; Corso et al. 1985a, 1985b; Chana et al. 1984). More recently, the use of gold and silver nanoparticles in catalysis, biological sensors and nanoelectronics domains increased the research on gold and silver corrosion, particularly to characterize corroded nanosurfaces (Sawada et al. 2019; Keast et al.

2016; Elechiguerra et al. 2005) and produce nanoporous metals by using corrosion processes, like chemical and electrochemical dealloying (Weissmüller et al. 2009; Fujita 2017). However, and contrarily to silver alloys, studies on the corrosion of gold alloys devoted to the field of cultural heritage are only occasionally carried out (Huang et al. 2021; Tissot et al. 2019; Lu et al. 2015; Corregidor et al. 2013; Liang et al. 2011; Campo et al. 2009; Bastidas et al. 2008; Gusmano et al. 2004a). The corrosion of gold objects is visually evidenced by a colour change; the surface can, for example, display multi-hued reddish areas, as shown in Figure 6.40.

Since the corrosion processes lead to alterations in the surface colour of the objects, a direct impact is observed on its perception. Consequently, there is a tendency to carry out regular restoration cleanings to remove the corrosion films, but often these take place without previous detailed characterization of the corroded surface. Therefore, the corrosion film thickness being unknown, these interventions may remove a layer thicker than the corrosion itself, leading to a loss of information related to the object production, for example intentional patinas or toolmarks. In addition, proceeding with restoration actions without characterizing the environment parameters, such as relative humidity and pollutants, responsible for the corrosion development, leads to unneeded repetitive restoration actions. To shed new light on the corrosion of precious metals, in particular of gold alloys, research has been developed in the last few years to define analytical strategies, which can often fully describe the corroded surface and the corrosion mechanisms.

Corrosion of precious metals

Although silver and gold are considered corrosion-resistant, this is not the case for their alloys. Objects made from silver-copper, gold-silver and

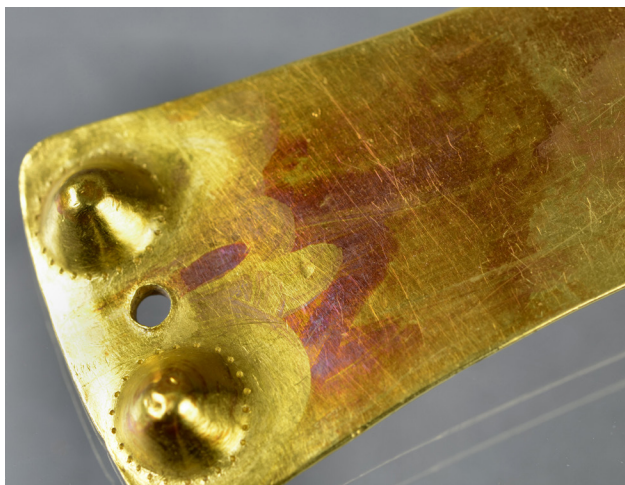


Figure 6.40. Detail of the Early Bronze Age archer's armband (Au 51) in the collection of the Portuguese National Museum of Archaeology, displaying a reddish corroded layer with iridescent effect.

gold-silver-copper alloys corrode, because the alloying elements have significant influence on the development of corrosion. Corroded silver and gold alloys exhibit a dull surface and may show a colour variation with a wide range of shades of yellow, red, violet, blue and green that can also be black in the case of silver. As referred, the corrosion processes result from ongoing chemical or electrochemical reactions at the surface of the alloy, which are specific to a given environment: burial, indoor and outdoor. Several factors influence the corrosion development, namely the environment parameters, the alloy composition and the fabrication techniques used to make the object.

Depending on the compounds present in the surrounding environment, which act as corroding agents, distinct corrosion products develop at the surface of the metallic surface. When silver and gold alloys are exposed to atmospheric corrosion (indoor and outdoor environments), humidity and the presence of gaseous pollutants such as H_2S , NO_x , SO_2 , O_3 induce the development of corrosion processes. The main corrosion products of silver-copper alloys are sulfur-based compounds, such as acanthite (Ag_2S) and stromeyerite (AgCuS). Other corrosion products such as silver and copper oxides have also been reported for these alloys (Salem 2017; Keturakis et al. 2016). In environments with a high concentration of chlorine compounds, such as some burial contexts and the maritime coastal areas, the development of chlorine-based corrosion products was observed, including the presence of chlorargyrite (AgCl) and paratacamite or atacamite ($\text{Cu}_3(\text{OH})_6\text{Cl}_2$) (Vassilou et al. 2009).

Considering gold alloys, several corrosion products have been identified on corroded objects. The main product resulting from atmospheric corrosion has been mostly identified as acanthite Ag_2S (Yang et al. 2007; Gusmano et al. 2004a, 2004b), but other corrosion products such as covellite (CuS), chalcocite (Cu_2S), petrovskaitite (AuAgS) and uytenbogaardtite (Ag_3AuS_2) have also been identified (Guerra & Tissot 2015; Bastidas et al. 2008; Griesser et al. 2005). References on corrosion of ancient gold objects caused by chloride compounds are to our knowledge inexistent, probably due to the insignificant influence of this element on the development of corrosion when compared to that of sulfur. Nevertheless, significant work has been developed on the corrosion of gold alloys employed in dentistry, among which can be found several approaches to corrosion processes in chlorine solutions. Those works refer to the preferential corrosion of silver and copper, but the corrosion products formed are not detailed (Corso et al. 1985a, 1985b; Sarkar et al. 1979).

As mentioned, another factor influencing the development of corrosion is the composition of the alloys used to manufacture the object. For example, the addition of copper to silver increases the corrosion resistance that becomes higher for silver-copper alloys than for pure copper and pure silver (Tissot et al. 2017; Tissot et al. 2016; Assaf et al. 2002). Recent studies revealed that the corrosion film that develops under the same conditions (corrosion medium and time period) at the surface of pure copper, pure silver and sterling silver (an alloy containing 7.5 wt% Cu) have distinct thicknesses. When immersed for 1 minute in a sulfur containing solution, the thicknesses of the corrosion layers were estimated to be about 90 nm higher for the pure elements than for the silver-copper alloy (Tissot et al. 2016).

On the contrary, the addition of alloying elements such as silver and copper to gold results in gold alloys with lower corrosion resistance. According to Randin et al. (1992), gold-silver-copper ternary alloys are more corrosion resistant than gold-silver and gold-copper binary alloys. Several authors suggested that above 50 at% of gold in the alloy, which corresponds to a gold concentration of 75.6 wt% for a gold-copper alloy and 64.6 wt% for a gold-silver alloy, the corrosion rate is low (Forty 1981). However, recent studies have demonstrated that corrosion occurs for ternary gold alloys containing 83 wt% Au (Tissot et al. 2019) or even higher amounts (Lu et al. 2015; Gusmano et al. 2004a). Under the same corrosion conditions, silver alloys and gold alloys corrode at distinct rates. The thickness of the corrosion layer that develops at the surface of gold alloys is thinner than that at the surface

of silver alloys. Tissot et al. (2019) reported the formation of an 80 nm thick layer for a gold alloy containing 17 wt% Ag and 7 wt% Cu immersed in a corrosive sulfur-based medium for 39 hours, whilst the same thickness was attained for sterling silver after only 3 minutes of immersion in the same solution.

Finally, the corrosion process is influenced by the technology of production of an object, because of thermo-mechanical processing that changes the metal microstructure, such as mechanical deformations and recrystallization annealing (Cason et al. 2015; Wanhill 2011; Alvarez et al. 2002; Rapson 1996). Stress-induced corrosion has been reported for silver alloys. One example is the Egyptian silver vase in the collection of the Allard Pierson Museum, dated to 300–200 BC (Wanhill et al. 1998). Stress-induced corrosion has only rarely been reported for ancient gold objects. One example is an Iron Age earring from the Pancas treasure (Alenquer, district of Lisbon, Portugal; Barreiros & Marcelo 2014; Tissot et al. 2013), shown in Figure 6.41a. In addition to metal cracking and fragmentation, stress-induced corrosion influences the nature of the corrosion products that develop on localized areas, for example, along cracks. Such is the case of an Early Bronze Age gold diadem shown in Figure 6.41b (Tissot et al. 2014).

In recent years, there has been an increase in the number of publications focusing on the corrosion of silver and gold objects exhibited in museums (Tissot et al. 2014, 2019; Corregidor et al. 2013; Guerra & Tissot 2013, 2015; Liang et al. 2011). This is probably due to the increase of pollutants concentration in the atmosphere. In the framework of the multi-disciplinary project CNRS PICS 5995, a few corroded Egyptian gold objects were studied. The results obtained are described below.

Corrosion of Egyptian goldwork

The studied corpus

Alfred Lucas made the first reference to the corrosion of Egyptian gold objects in 1926 (Lucas 1926). He attributed the coloured spots on the surface of some excavated gold objects to the development at the surface of the gold alloys of the corrosion products of the alloying elements. According to him, the dull and tarnished yellow areas are composed of silver and copper corrosion products, the grey ones contain silver chloride, and the reddish-brown areas result from the presence of iron and copper oxides. The corrosion of Egyptian objects made from gold alloys was occasionally addressed by other authors after the studies by Lucas. Frantz & Schorsch (1990) studied a group of nine objects and indicated that the reddish colouration observed results from tarnishing and is due to the presence of petrosvkaite (AgAuS). They attributed the different colour hues to the variation in thickness of the corrosion film and to the presence of other compounds such as uytenbogaardtite (Ag_3AuS_2). Abdrabou et al. (2018) and Rifai & El Hadidi (2010) identified on the corroded surface of Egyptian gold foils a higher concentration of silver and sulfur when compared to the non-corroded surfaces. Although with some uncertainties, the coloured surfaces were ascribed by some authors to an intentional surface treatment and not to alteration resulting from a corrosion process.

In this work we studied three jewellery items and eight gold foil fragments showing different surface colours and textures. Dated to different periods and kept in different collections, all of them show surface colour alteration, but display distinct surface colours in the corroded areas that can be separated into two types. One of the colour alterations is red and homogeneous;

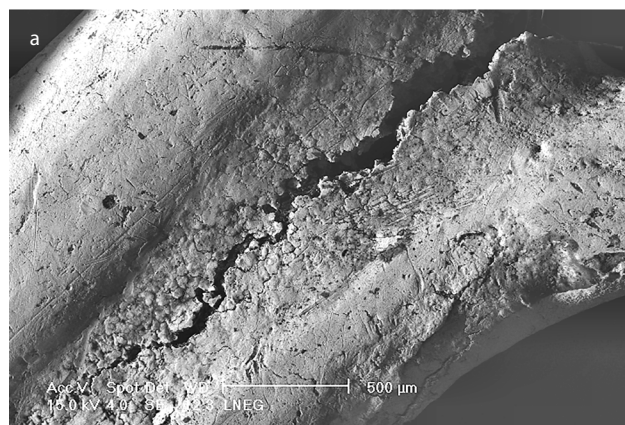


Figure 6.41. Stress-induced corrosion of (a) a fracture in an Iron Age earring and (b) a crack in an Early Bronze Age diadem (Au 835 and Au 133, National Museum of Archaeology, Portugal).

Table 6.9. List of the studied objects with their identification, accession number, and collection.

| Object | Acc. No. | Collection | Chronology |
|-----------------------|----------------|-----------------|------------------------------|
| Element of an armband | E7168 | Louvre Museum | Bearing the name of Ahmose I |
| Signet ring | E7725 | Louvre Museum | Bearing the name of Ahhotep |
| Biconical bead | A.1914.1096 | NMS | Tomb 72 Haraga (12th Dyn.) |
| Foil fragments (8) | 431-24, 432-25 | Garstang Museum | Abydos (12th Dyn.) |

the other is heterogeneous with areas going from dark yellow to violet, blue and red.

The objects, listed in Table 6.9, were made using distinct alloys and fabrication techniques. Two of them, in the collection of the Louvre Museum, are dated to the 17th–18th Dynasties (objects are shown



Figure 6.42. (a) The corroded surface of a gold cartouche-shaped box bearing the name of Ahmose I (E7168, Louvre Museum). (b) Some highly corroded beads found in 12th Dynasty tomb 72 excavated at Haraga (NMS A.1914.1096).



Figure 6.43. Fragments of corroded gold foils from several burials excavated at Abydos, North Cemetery, in the collection of the Garstang Museum of Archaeology.

in Fig. 9.20 in Chapter 9.4). One of them is a cast signet ring bearing the name of queen Ahhotep. The other, whose corroded surface is shown in Figure 6.42a, is a cartouche-shaped element of an armband bearing the name of king Ahmose I, found in the burial of his brother Kamose at Dra Abu al-Naga (Guerra & Pagès-Camagna 2019). The third object is a biconical bead from a string found in tomb 72 excavated at Haraga, containing the intact burial of a young girl, dating to the mid-late 12th Dynasty (Troalen et al. 2016). Presently this bead is contained in a highly corroded string of beads in the collection of NMS (shown in Fig. 8.6 in Chapter 8.2). Some of these corroded beads are shown in Figure 6.42b. We also studied eight gold foil fragments in the collection of the Garstang Museum of Archaeology, University of Liverpool (Tissot et al. 2015), shown in Figure 6.43. The gold foils, some still attached to gilded objects (shown in Figure 6.44), are described in Chapter 8.6. They were found in tombs excavated between 1906 and 1909 by John Garstang in the so-called North Cemetery at Abydos (Snape 1987).

The study of those objects, described below, included the identification of the corrosion products and the investigation of the relation between the surface alteration and the fabrication techniques by using SEM-EDS, FEG-SEM-EDS and μ XRF.

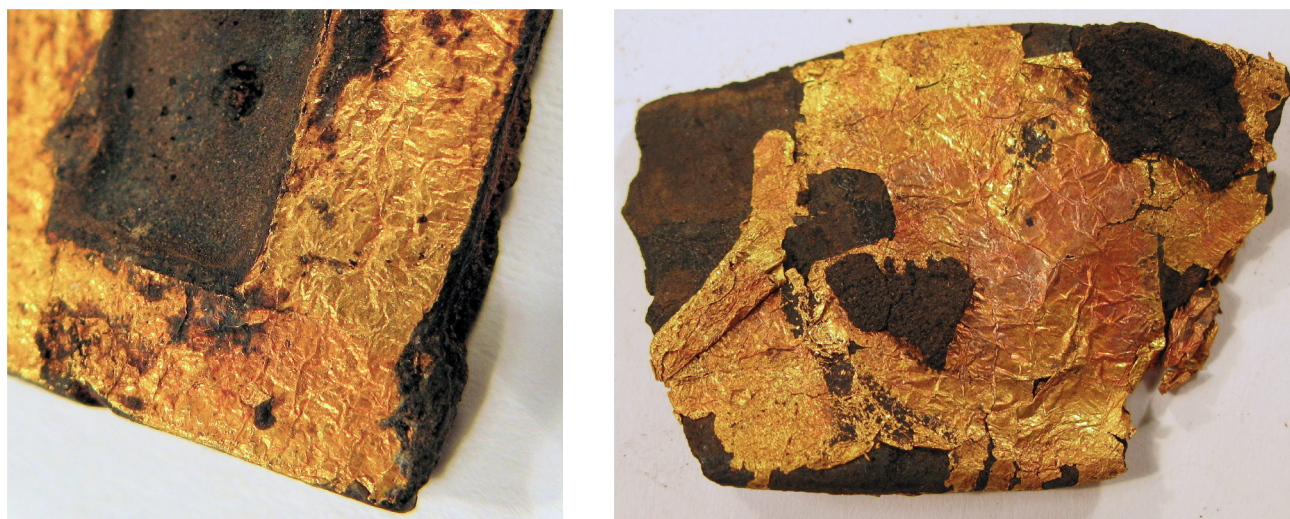


Figure 6.44. Fragments of wood with gold leaf excavated at Abydos, North Cemetery, in the collection of the Garstang Museum: on the left from tomb 381 (E. 5727) and on the right from tomb 533 (E. 5726).

Analytical protocol

The jewellery and foil fragments listed in Table 6.9 were analysed for the composition of the gold alloys and the composition and morphology of the corrosion products. The elemental composition of the gold-based alloys was determined by μ XRF and the morphology and elemental composition of the corrosion products by SEM-EDS and FEG-SEM-EDS. According to the collections where the objects are kept, different equipment was employed for the study.

A small piece of the bead from Haraga lost by corrosion and the eight gold foil fragments were analysed at the LIBPhys, NOVA University of Lisbon, by μ XRF using a M4 Tornado equipment from Bruker (Tissot et al. 2015) comprising an Rh target X-ray source, coupled to an XFlash® SDD detector, with a 30 mm² sensitive area and energy resolution <145 eV at 5.9 keV. The polycapillary X-ray optics offers a spot size down to a 25 μ m at a working distance of 10 mm. Spectra were collected with the X-ray tube operating at 50 kV and 300 μ A with 300 s acquisition time. The spectra deconvolution was made using Bruker M-Quant software and the quantification of the major elements was obtained using Au and Ag L $_{\alpha}$ -lines and Cu K $_{\alpha}$ -line. The objects were examined by FEG-SEM-EDS at the National Laboratory for Energy and Geology (LNEG) in Lisbon, with a Philips XL 30 FEG model, with a field emission electron source operated with acceleration voltage from 10 to 15 kV. Qualitative and semi-quantitative elemental analyses were performed with an EDS (EDAX) system equipped with a Si(Li) detector with a 3 μ m super ultra-thin window (SUTW) allowing detection of light elements. X-ray

spectra were collected in spot mode analysis for 300 s acquisition time. Semi-quantitative analyses were done by EDAX software, using ZAF matrix correction model and confirmed using a range of homemade gold standards certified by other techniques (Tissot et al. 2013).

The component of an armband in the form of a cartouche and the signet ring in the collection of the Louvre Museum were analytically studied at the Centre de recherche et de restauration des musées de France (C2RMF) in Paris. The alloys were determined by PIXE at the AGLAE van de Graaff accelerator using a 3 MeV proton μ beam at the regular experimental conditions employed for the analysis of gold alloys (Guerra 2004, 2008). The objects were also examined by SEM-EDS using a FEI Philips XL 30 CP with controlled pressure. Image capture and X-ray spectra were collected in spot mode for a 300 s acquisition time and acceleration voltages from 10 to 20 kV.

Characterization of the corroded surface

Elemental composition of the corroded surface

All the objects show corroded surfaces that can be separated in two colour alterations: i) a heterogeneous colouration with a colour variation from dark yellow, violet, and blue to red (Fig. 6.45a) and ii) a homogeneous red colouration (Fig. 6.45b). The signet ring, the cartouche and the bead are in the last group, but the gold foil fragments show both corrosion types. However, as shown in Table 6.10, the composition of the alloy is quite variable, with silver contents ranging from 2 to 35 wt% and copper contents from 0 to 4 wt%.

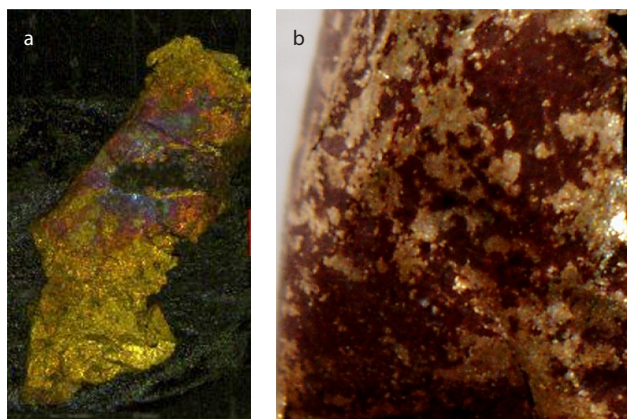


Figure 6.45. (a) Gold foil fragment from Abydos with a heterogeneous coloured surface. (b) Fragment from one gold bead from Haraga tomb 72, with a homogeneous surface of red colour.

Surface analysis of the gold foils by μ XRF shows an increase of the Ag content in the corroded surface areas with heterogeneous colouration. These results suggest the existence of a relationship between the colour of the corrosion products and the surface silver content, as shown in Figure 6.46. The increase of the silver content on the corroded areas suggests the formation of an Ag-based corrosion product, which is in accordance with the results published by other authors for corroded Egyptian objects (Abdrabou et al. 2018; Rifai & El Hadiddi 2010; Frantz & Schorsch 1990). The gold foils with heterogeneous colour surface are made from alloys with a silver content above 9–10 wt%. This fact could suggest that this type of corrosion is related to silver contents in gold alloys equal or higher than 10 wt%.

On the contrary, the homogeneous red colouration is observed for objects with a wide range of silver contents (from 2 to 35 wt%). This is exemplified in the diagram of Figure 6.47, plotting the gold/silver ratio as a function of the sulfur content, measured by μ XRF at the surface of one foil fragment and of the bead from Haraga. The bead contains 35 wt% Ag and 3 wt% Cu and the gold foil contains 4 wt% Ag and amounts of copper below 0.3 wt%. For both objects, we observed in the corroded areas a significant increase of the amounts of sulfur and a quite small variation of the silver contents.

Summing up, although the composition obtained by μ XRF corresponds to an average of the substrate and the corrosion layer, because the depth resolution is higher than the thickness of the corrosion layer, there was observed for the analysed corroded areas a significant increase in silver in the case of

Table 6.10. Results obtained by μ PIXE, SEM-EDS and μ XRF, normalized to 100 wt%, for the objects listed in Table 6.9 (Troalen et al. 2016; Tissot et al. 2015; Lemasson et al. 2015).

| Object | Acc. No. | wt% | | |
|-----------------------|-------------|-----|----|----|
| | | Au | Ag | Cu |
| Element of an armband | E7168 | 66 | 31 | 3 |
| Signet ring | E7725 | 84 | 12 | 4 |
| Biconical bead | A.1914.1096 | 62 | 35 | 3 |
| Foil fragments (8) | 431-24, 1.1 | 96 | 4 | 0 |
| | 431-24, 1.2 | 98 | 2 | 0 |
| | 432-25, 2.1 | 94 | 6 | 0 |
| | 432-25, 2.2 | 88 | 11 | 1 |
| | 432-25, 2.3 | 79 | 20 | 1 |
| | 432-25, 2.4 | 96 | 4 | 0 |
| | 432-25, 2.5 | 92 | 7 | 1 |
| | 432-25, 2.6 | 89 | 10 | 1 |

the heterogeneous colour surfaces and a significant increase in sulphur in the case of the homogeneous colour surfaces.

Morphology of the corrosion products

As the heterogeneous and the homogeneous coloured layers that develop in the corroded areas at the surface of the gold objects show distinct elemental compositions, the corroded surfaces were observed under the SEM. In this way, we verified that the heterogeneous and the homogeneous colourations present distinct morphologies.

The surface morphology of the heterogeneous colour alteration, with red and blue areas (Fig. 6.47b), shows in the red area a regular nanoporous layer containing round particles (Fig. 6.48a). The blue area is composed of three different layers (Fig. 6.48b): the first is morphologically similar to the one observed for the red areas, the second contains agglomerates of corrosion products, and the third contains thin tubes randomly distributed (Fig. 6.48c). This latter layer is visible in areas with accentuated corrosion. SEM-EDS analysis of the blue areas reveals an increase of the Ag and S contents that vary according to the distinct mentioned layers (Table 6.11). The silver content, which for the base alloys is c. 10 wt%, attains 80 wt% in the first layer, 65 wt% in the second layer and 54 wt% in the third one.

When the colouration of the corroded area is red and homogeneous, at the surface are observed aggregates of small round particles that form a nanoporous layer. This phenomenon is similar to what is observed for the red heterogeneous corrosion (Fig. 6.49a). Areas with more accentuated corrosion present on the top of the porous layer randomly oriented

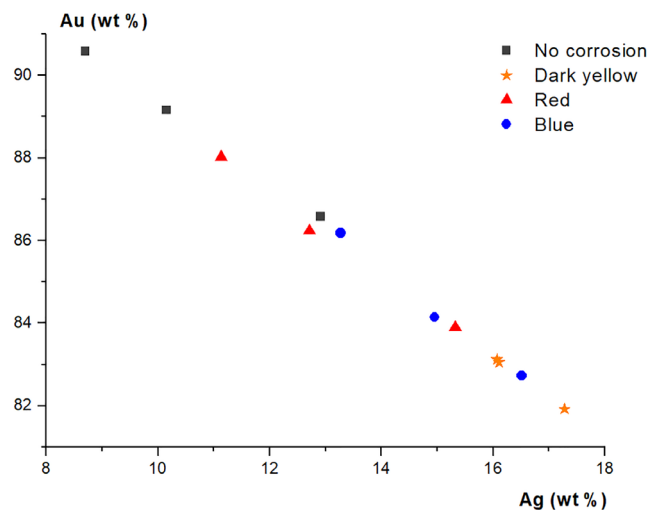


Figure 6.46. Gold versus silver contents obtained by μ XRF for the different corrosion colours of a gold foil fragment (no. 2.6, Garstang Museum 432-25) showing a heterogeneous coloured surface.

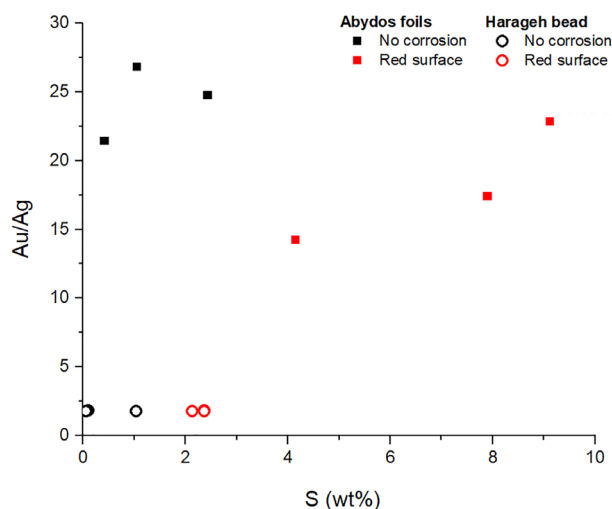


Figure 6.47. Ratio Au/Ag versus S content obtained by μ XRF for the corroded (red surface) and non-corroded areas of one of the gold foil fragments from Abydos (2.4, Garstang Museum 432-25,) and the bead from Haraga.

hollow polycrystalline tubular formations, and therefore a layered corrosion process (Fig. 6.49b).

Interestingly, the corrosion products present at the surface of the Haraga bead (Fig. 6.49c) and of the armband cartouche are mixed with silicates from the burial contexts, which seemingly prevented the development of tubular shaped corrosion products.

Table 6.11. Results obtained by SEM-EDS, normalized to 100 wt%, for the three distinct layers observed in the blue corroded area of foil fragment 2.6 (shown in Fig. 6.48b).

| | | wt% | | | |
|---------------|-----------|------------|------------|------------|------------|
| | | Au | Ag | Cu | S |
| | | L α | L α | K α | K α |
| Base alloy | | 89 | 10 | 1 | |
| Corroded area | 1st layer | 15 | 80 | 1 | 4 |
| | 2nd layer | 28 | 65 | 1 | 6 |
| | 3rd layer | 36 | 54 | 1 | 9 |

However, they present the same two-layer morphology, the first of which is composed of aggregates of small round particles.

EDS analyses of the corroded surface of the gold foil fragments with homogeneous corrosion show for the first layer an increase in silver and sulphur contents when compared to the base alloy composition, suggesting the formation of silver-sulfur-based compounds (Table 6.12). The areas with higher concentrations of

Table 6.12. Results obtained by SEM-EDS, normalized to 100 wt%, for the base alloy and corrosion layer of foil fragment 2.4 (GM 432-25).

| | | wt% | | | |
|---------------|---------------|------------|------------|------------|------------|
| | | Au | Ag | Cu | S |
| | | L α | L α | K α | K α |
| Base alloy | | 96 | 4 | 1 | |
| Corroded area | 1st layer | 68 | 23 | 1 | 8 |
| | tubular forms | 67 | 23 | 1 | 9 |

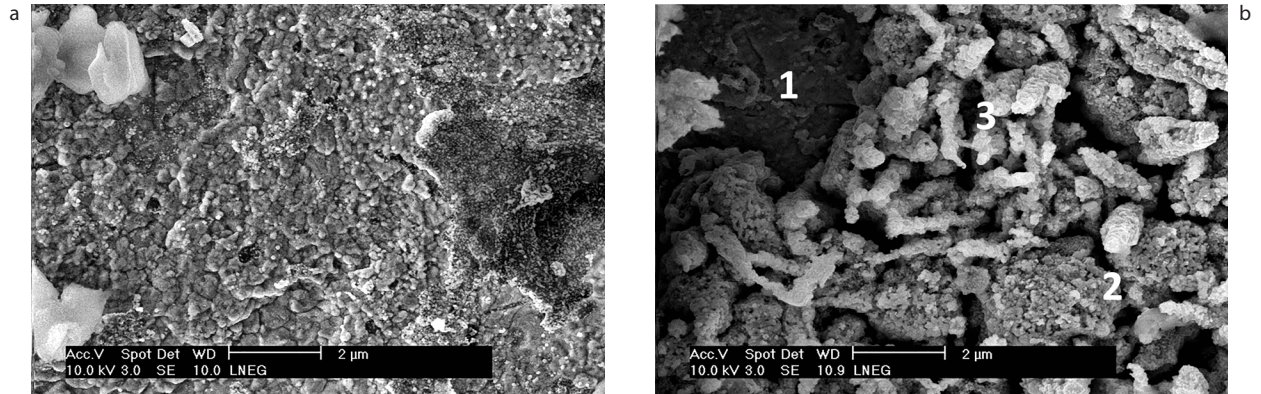


Figure 6.48. FEG-SEM-SE micrographs of the heterogeneous corroded area of foil fragment 2.6 from Abydos (Garstang Museum 432-25): (a) the red area and (b) the blue area. The blue area is composed of three distinct layers: layer 1) nearer the surface, morphologically similar to the red corroded areas; layer 2) containing corrosion products featuring nanoparticles agglomerates; and layer 3) containing corrosion products featuring thin nanotubes, which are shown in (c).

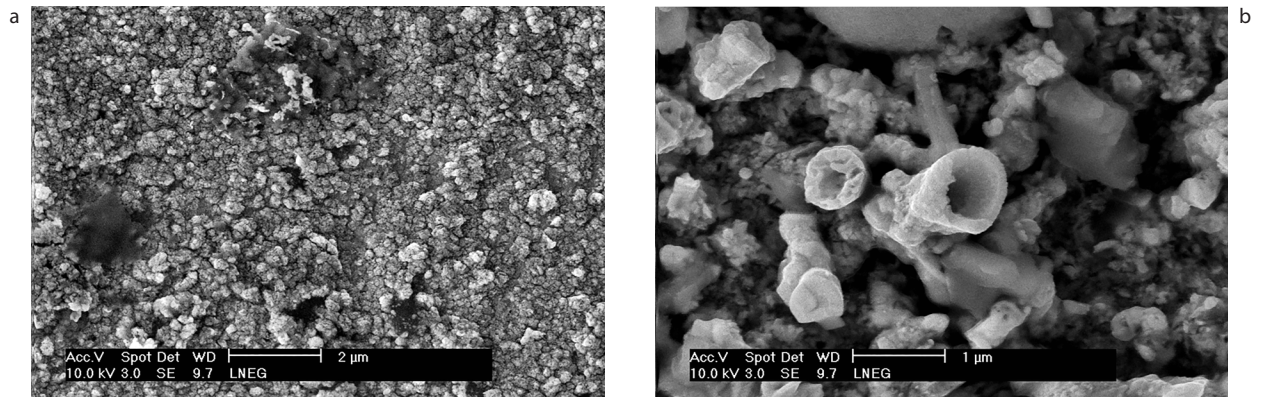
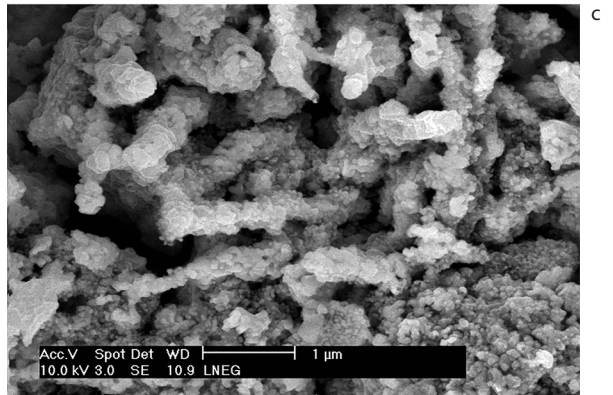


Figure 6.49. FEG-SEM-SE micrographs of homogeneous red corroded areas of (a) foil fragment 2.4 from Abydos with (b) a detail of the polycrystalline tubular formations, and of (c) the fragment of a bead from Haraga showing different layers of corrosion products mixed with silicates from the burial context.

tubular nanostructures show silver contents higher than 20 wt% and 9 wt% S.

Considering both the composition and the morphology of the two corrosion types (heterogeneous and homogeneous), it is possible to suggest that the different colours are related to the thickness of the corroded layer and to the presence of corrosion products with different morphologies, and hence to different corrosion phases. The elemental analysis of the corroded areas suggests the formation of distinct silver-based corrosion products. To confirm this, it would be necessary to carry out a structural identification. An attempt was made on one of the gold foil fragments by using X-ray diffraction (XRD). However, no corrosion products could be identified, which may be explained by the fact that the corrosion compounds may be less crystalline or present at too low quantity. In fact, the corrosion thickness of gold alloys is nanometric, inferior to the XRD depth resolution. Tissot et al. (2019) recently demonstrated by using *in situ* ellipsometry that at the surface of a ternary gold alloy containing 76 wt% Au, 17 wt% Ag and 7 wt% Cu, upon 39 h exposure to a high concentration sulfur-based solution, a two-layered corrosion film forms, with 80 nm total thickness (60 nm thick inner layer and 20 nm thick outer layer). This confirms the formation of layered structures, as observed for the studied Egyptian objects.

Intergranular corrosion and stress corrosion cracking

Intergranular corrosion and stress corrosion cracking were observed under SEM for the bead from Haraga and for the armband cartouche bearing the name of king Ahmose I.

Intergranular corrosion and stress corrosion cracking are usually associated either with casting defects or with production techniques that involve substantial plastic deformation. These two types of corrosion are related to the alteration of the metal microstructure, where adjacent grains are separated by grain boundaries. Intergranular corrosion is the preferential corrosion along the grain boundaries, or adjacent to grain boundaries, while the bulk of the grains remains unaffected. Stress-corrosion cracking is induced by the combined action of tensile stress and a reactive environment. The tensile stress may be in the form of either directly applied stresses or residual stresses (Rapson 1996; Forty 1981).

Under SEM the bead from Haraga tomb 72 showed a porous surface texture indicating that annealing during the production process of the gold foil by hammering was incomplete. The annealing temperatures used in the manufacture of the majority of the beads from that tomb were below those required to

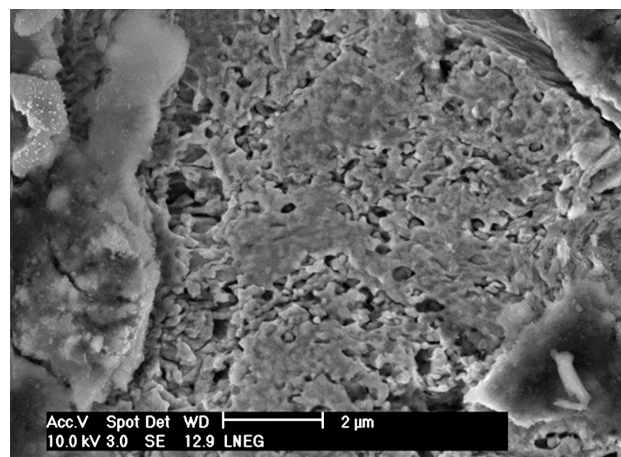


Figure 6.50. FEG-SEM-SE micrograph of the fragment of a bead from Haraga showing the heterogeneous surface caused by improper annealing.

obtain a homogenous surface, as shown in Figure 6.50, leading to a less hard surface (Cason et al. 2015). After formation, the crack propagates along the boundaries of several grains until a critical velocity of propagation is achieved resulting in fracture. Thereafter, the crack continues as a transgranular fracture (Merriman et al. 2005, 114). According to Dugmore et al. (1979, 141), the susceptibility to stress corrosion is also strongly dependent on the gold alloy composition, normally occurring for alloys with gold contents lower than 58 wt%. In the case of our bead, the gold content is 63 wt%; however, it should be also considered that the foil thickness increases its fragility.

On the cartouche bearing the name of Ahmose I, the corrosion develops along the grain boundaries, but the grains bulk remain almost unaffected (Fig. 6.51). This intergranular corrosion is often associated with chemical segregation effects or with the precipitation of specific phases along the grain boundaries (Dowben et al. 1987). Such precipitation can produce zones of reduced corrosion resistance. On the surface of the object, the presence of other corrosion products, randomly distributed, suggests the development of an independent corrosion process. This may indicate an atmospheric corrosion process that began during burial or exhibition.

Conclusions

The analytical characterization of the corroded surface of the Egyptian goldwork selected for study was an important contribution to the research on the corrosion mechanisms of ancient gold alloys. The analytical results showed that corrosion products develop in a

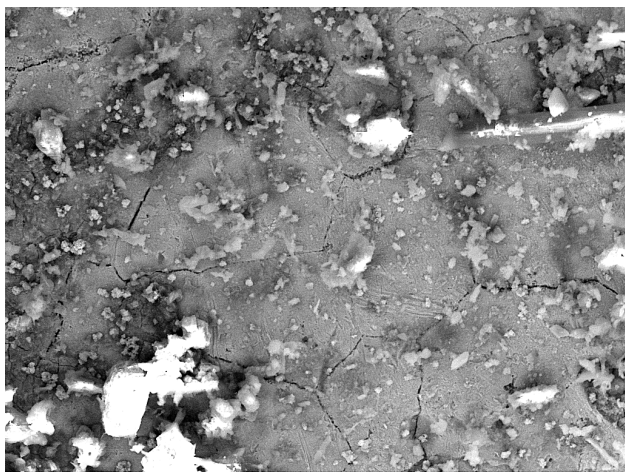


Figure 6.51. SEM-SE micrograph of the cartouche bearing the name of Ahmose I part of Kamose's armband, showing intergranular corrosion and the presence of corrosion products.

layer-by-layer structure containing different corrosion products. This type of corrosion mechanism was recently suggested for ternary gold alloys in sulphide environments (Tissot et al. 2019). The results obtained in this study also confirmed that the colour of the corroded areas is not only the result of the corrosion film thickness but also of the distinct morphologies of the formed corrosion products.

The analysed objects displayed homogeneous and heterogeneous coloured corrosion areas. Those in the first group exhibit red surfaces whereas the latter exhibit multi-coloured surfaces, ranging from dark yellow, to red and blue. Elemental data associated with each corrosion product morphology revealed the formation of gold-silver-sulfur based compounds and suggested the formation of different corrosion products for distinct gold-base alloys.

It was also shown that the fabrication techniques influence the development of intergranular corrosion and of stress corrosion cracking. These types of corrosion can produce zones of reduced corrosion resistance and induce the formation of corrosion products in localized areas. This contributes to the heterogeneous colouration of the corroded surfaces.

This study also contributed to the definition of new challenges concerning the conservation of Egyptian goldwork. Until recently, the corrosion products

of gold alloys have been considered to be mainly the result of the corrosion of the alloying elements, copper and silver, leading to the application of the same cleaning processes (Angelini et al. 2013). Therefore, the removal of corrosion products at the surface of gold alloys has been based on mechanical, chemical, and electrochemical methods commonly applied to clean objects made from silver alloys, which develop much thicker corrosion layers than gold alloys. Mechanical methods use abrasives (SiO_2 , Al_2O_3 , TiO_2 , CaCO_3 , etc.) mixed with organic substances (soaps, fatty acids, etc.) (Palomar et al. 2016; Wharton et al. 1990). Chemical methods are widely based on the use of acidified thiourea ($\text{CS}(\text{NH}_2)_2$), which acts as a chelating agent dissolving Ag_2S . Other weak acids, such as formic acid, and chelating agents, like ethylenediaminetetraacetic acid (EDTA), are also used. Electrochemical methods consider mainly the reduction of Ag_2S based on the assumption this is the main corrosion product formed during gold alloys corrosion. Other methods like laser cleaning (Lee et al. 2003; Degriigny et al. 2003; Siano & Salimbeni 2010), cold plasma (Ioanid et al. 2011) and UV/Ozone treatment (Hacke et al. 2003) were also applied. However, none of the used methods presents optimal results when the visual appearance, base metal loss, cleaning residues left on the surface and re-tarnishing are assessed (Palomar et al. 2016).

Based on the conservation methods currently used for gold alloys and on the recent research on their corrosion mechanisms, new conservation methodologies must be developed, considering the thinness of the corrosion layer of gold alloys. In addition, further investigation of the corrosion surfaces should be pursued, including structural identification of the corrosion products.

Acknowledgments

The authors are grateful to Dr. Maria Alexandra Barreiros (LNEG, Portugal) for support during this study and key SEM-EDS and FEG-SEM-EDS analysis that significantly broaden the quality of the results obtained, and to Dr. Lore Troalen (National Museums Scotland, UK) for access to the sample from Haraga tomb 72. Part of the work was developed under the scope of the CNRS-funded project PICS 5995 'Analytical study of Bronze Age Egyptian gold jewellery' and partially supported by the Fundação para a Ciência e Tecnologia in Portugal (SFRH/BDE/51439/2011).

References (for complete Chapter 6)

- Abdrabou, A., El Hadidi, N.M.N., Hamed, S. & Abdallah, M., 2018. Multidisciplinary approach for the investigation and analysis of a gilded wooden bed of King Tutankhamun. *Journal of Archaeological Science: Reports* 21, 553–64.
- Abramowitz, M., 2003, *Microscope. Basics and Beyond Series 1*, revised edition. Melville, NY: Olympus America Inc.
- Adriaens A. & Dowsett, M.G., 2004. Electron microscopy and its role in cultural heritage studies, in *Comprehensive Analytical Chemistry* 42, eds. K. Janssens & R. Van Grieken. Amsterdam: Elsevier B.V., 73–128.
- Adrimi-Sismani, V., Guerra, M.F. & Walter, P., 2009. La tombe mycénienne de Kazanaki (Volos) et le mythe de la Toison d'or. *ArcheoSciences* 33, 135–41.
- Ahmadabadian, A.H., Robson, S., Boehm, J. & Shortis, M., 2013. Image Selection in photogrammetric multi-view stereo methods for 3D reconstruction, in *Videometrics, Range Imaging, and Applications XII*, eds. F. Remondino, M.R. Shortis, J. Beyerer & F. Puente León. SPIE Conference Proceedings 8791. The International Society for Optical Engineering, Article 879107.
- Alvarez, M.G., Fernández, S.A. & Galvele, J.R., 2002. Effect of temperature on transgranular and intergranular stress corrosion crack velocity of Ag-Au alloys. *Corrosion Science* 44, 2831–40.
- Andrews, C., 1990. *Ancient Egyptian jewellery*. London: British Museum Publications.
- Angelini, E., Grassini, S. & Tusa, S., 2013. Underwater corrosion of metallic heritage artifacts, in *Corrosion and conservation of cultural heritage metallic artefacts*, eds. Dillmann, P., Watkinson, D., Angelini, E. & A. Adriaens. European Federation of Corrosion Publications 65. Cambridge: Woodhead Publishing Limited, 236–59.
- Aruz, J., 2008. Falcon with prey & Lid with falcons in *Beyond Babylon. Art Trade and Diplomacy in the Second Millennium BC*, eds. J. Aruz, K. Benzel & J. M. Evans. New York / New Haven / London: The Metropolitan Museum of Art / Yale University Press, 88–9.
- Assaf, F.H., Zaky, A.M. & El-Rehim, S.S.A., 2002. Cyclic voltammetric studies of the electrochemical behaviour of copper-silver alloys in NaOH solution. *Applied Surface Science* 187, 18–27.
- Barham, E., 2007. Controlled lifting and X-radiography of gold threads from ancient archaeological textiles, in *X-Radiography of Textiles, Dress and Related Objects*, eds. S. O'Connor & M.M. Brooks. Oxford: Butterworth-Heinemann, 302–6.
- Barreiros, M.A. & Marcelo, T., 2014. Estudos por SEM-EDS de torques, braceletes e arrecadas, in *A ourivesaria pré-histórica do Ocidente Peninsular Atlântico: compreender para conservar*, eds. M.F. Guerra & I. Tissot. Lisbon: AuCORRE, 59–62.
- Bass, G.F., 1986. A Bronze Age Shipwreck at Ulu Burun (Kaş): 1984 Campaign. *American Journal of Archaeology* 90(3), 269–96.
- Bass, M. (ed.), 2010. *Handbook of Optics I*, 3rd edition. The McGraw-Hill Companies, Inc.
- Bastidas, D.M., Cano, E., González, A.G., Fajardo, S., Lleras-Pérez, R., Campo-Montero, E., Belzunce-Varela, F.J. & Bastidas, J.M., 2008. An XPS study of tarnishing of a gold mask from a pre-Columbian culture. *Corrosion Science* 50, 1785–8.
- Beckhoff, B., Kanngießner, B., Langhoff, N., Wedell, R. & Wolff, H., 2007. *Handbook of Practical X-Ray Fluorescence Analysis*. Berlin Heidelberg: Springer-Verlag.
- Bianucci, R., Habicht, M.E., Buckley, S., Fletcher, J., Seiler, R., Öhrström, L.M., Vassilika, E., Böni, T., & Rühli, F. J., 2015. Shedding New Light on the 18th Dynasty Mummies of the Royal Architect Kha and His Spouse Merit. *PloS one* 10(7), e0131916.
- Binder, S., 2008. *The Gold of Honour in New Kingdom Egypt*. Oxford: Aris & Phillips Ltd.
- Blaber, M.G., Ford, M.J. & Cortie, M.B., 2010. The Physics and Optical Properties of Gold, in *Gold: science and applications*, eds. C. Corti & R. Holliday. CRC Press, Taylor and Francis Group, 13–30.
- von Bohlen, A., Hergenroder, R., Sternemann, C., Paulus, M., Radtke, M. & Riesemeier, H., 2005. Wavelength dispersive synchrotron microprobe used for material analysis. *Instrumentation Science & Technology* 33(2), 137–50.
- Boone, M.N., Garrevoet, J., Tack, P., Scharf, O., Cormode, D.P., Van Loo, D., Pauwels, E., Dierick, M., Vincze, L. & Van Hoorebeke, L., 2014. High spectral and spatial resolution X-ray transmission radiography and tomography using a Color X-ray Camera. *Nuclear Instruments & Methods in Physics Research A* 735, 644–8.
- Borel, T., 1995. La radiographie des objets d'art. *Techné* 2, 146–57.
- Bouchard, J.F. & Guerra, M.F., 2009. Archéologie pré-colombienne et analyses scientifiques. La figurine d'El Angel, une œuvre composite d'orfèvrerie de la culture La Tolita Tumaco (Équateur-Colombie). *ArcheoSciences* 33, 273–9.
- Brunetti, B.G., Cartechini, L., Miliani, C. & Sgamellotti, A., 2013. Metal Nanoparticles in Glass: Lustre, in *Modern Methods for Analysing Archaeological and Historical Glass*, ed. K. Janssens. John Wiley & Sons, Ltd., 583–608.
- Burgess, S., Li, X. & Holland, J., 2013. High spatial resolution energy dispersive X-ray spectrometry in the SEM and the detection of light elements including lithium. *Microscopy and Analysis* 27(4), S8–S13.
- Campbell, J.L., Boyd, N.I., Grassi, N., Bonnicks, P. & Maxwell, J.A., 2010. The Guelph PIXE software package IV. *Nuclear Instruments and Methods in Physics Research B* 268, 3356–63.
- Campo, E., Vera, E., Göllner, J., Ortiz, C.A. & Lleras, R., 2009. Degradación de piezas arqueológicas “Colección Calima” Museo del Oro. *Suplemento de la Revista Latinoamericana de Metalurgia y Materiales* S1(2), 657–61.
- Carvalho, O., Soares, D., Fonseca, A. & Silva, F.S., 2009. Tarnish and corrosion evaluation of a blue-gold based alloy. *Materials and Corrosion* 60, 355–9.
- Casali, F., 2006. X-ray and Neutron Digital Radiography and Computed Tomography for Cultural Heritage, in *Physical Techniques in the Study of Art, Archaeology*

- and *Cultural Heritage I*, eds. D. Creagh & D. Bradley. Amsterdam: Elsevier B.V., 41–123.
- Cason, C., Pezzato, L., Breda, M., Furlan, F. & Dabalà, M., 2015. Effect of microstructure and residual stresses, generated from different annealing and deformation processes, on the corrosion and mechanical properties of gold welding alloy wires. *Gold Bulletin* 48, 135–45.
- Champollion, J.-F., 1827. *Notice descriptive des monuments égyptiens du musée Charles X*. Paris: Imprimerie de Crapelet
- Chana, M.S. & Kuhn, A.T., 1984. A critique of the Tuccillo-Nielsen wheel method for tarnish testing of dental alloys. *Journal of Dentistry* 12, 314–8.
- Colorimetry, 2004. *CIE 15 technical report*, 3rd edition. Vienna: International Commission on Illumination.
- Corregidor, V., Alves, L.C. & Cruz, J., 2013. Analysis of surface stains on modern gold coins. *Nuclear Instruments and Methods in Physics Research B* 306, 232–5.
- Corso, P.P., German, R.M. & Simmons, H.D., 1985a. Corrosion evaluation of gold-based dental alloys. *Journal of Dental Research* 64, 854–9.
- Corso, P.P., German, R.M. & Simmons, H.D., 1985b. Tarnish evaluation of gold-based dental alloys. *Journal of Dental Research* 64, 848–53.
- Costa, V., 2001. The deterioration of silver alloys and some aspects of their conservation. *Studies in Conservation* 46(1), 18–34.
- Courty, C., Matthieu, H.J. & Landolt, D., 1991. Tarnishing of Au-Ag-Cu alloy studied by Auger electron spectroscopy and coulometry. *Materials and Corrosion* 42, 288–95.
- Croft, W.J., 2006. *Under the Microscope: A Brief History of Microscopy*. Singapore: World Scientific Publishing Co. Pte. Ltd.
- Curto, S. & Mancini, M., 1968. News of Kha' and Meryt. *The Journal of Egyptian Archaeology* 54, 77–81.
- Degrigny, C., Tanguy, E., Le Gall, R., Zafiropoulos, V. & Marakis, G., 2003. Laser cleaning of tarnished silver and copper threads in museum textiles. *Journal of Cultural Heritage* 4, 152–6.
- Dowben, P.A., Miller, A.H. & Vook, R.W., 1987. Surface segregation from gold alloys. *Gold Bulletin* 20, 54–65.
- Duczko, W., 1985. *The filigree and granulation work of the Viking Period. An analysis of the material from Björkö*. Birka V. Stockholm: Kungl. Vitterhets Historie och Antikvitets Akademien
- Dugmore, J.M.M. & DesForges, C.D., 1979. Stress corrosion in gold alloys. *Gold Bulletin* 4, 140–4.
- Earl, G., Martinez, K. & Malzbender, T., 2010. Archaeological applications of polynomial texture mapping: analysis, conservation and representation. *Journal of Archaeological Science* 37(8), 2040–50.
- Elechiguerra, J.L., Larios-Lopez, L., Liu, C., Garcia-Gutierrez, D., Camacho-Bragado, A. & Yacaman, M.J., 2005. Corrosion at the nanoscale: the case of silver nanowires and nanoparticles. *Chemistry of Materials* 17, 6042–52.
- Fearon, E., Sato, T., Wellburn, D., Watkins, K.G. & Dearden, G., 2007. Thermal effects of substrate materials used in the laser curing of particulate silver inks. *Laser Assisted Net Shape Engineering* 5, 379–90
- Festa, G., Minniti, T., Arcidiacono, L., Borla, M., Di Martino, D., Facchetti, F., Ferraris, E., Turina, V., Kockelmann, W., Kelleher, J., Senesi, R., Greco, C. & Andreani, C., 2018. Egyptian Grave Goods of Kha and Merit Studied by Neutron and Gamma Techniques. *Angewandte Chemie* 57(25), 7375–9.
- Fioravanti, K.J. & German, R.M., 1988. Corrosion and tarnishing characteristics of low content dental casting alloys. *Gold Bulletin* 21, 99–110.
- Fitton J.L., Meeks N.D. & Joyner, L., 2009. The Aigina treasure: catalogue and technical report, in *The Aigina Treasure, Aegean Bronze Age Jewellery and a Mystery Revisited*, ed. J.L. Fitton. London: The Trustees of the British Museum, 17–31.
- Fontenay, E., 1887. *Les bijoux anciens et modernes*. Paris: Maisson Quantin.
- Forty, A.J., 1981. Micromorphological studies of the corrosion of gold alloys. *Gold Bulletin* 14, 25–35.
- Frantz, J.H. & Schorsch, D., 1990. Egyptian Red Gold. *Archaeo-materials* 4, 133–52.
- Freestone, I., Meeks, N., Sax, M. & Higgitt, C. 2007. The Lycurgus Cup - A Roman nanotechnology. *Gold Bulletin* 40, 270–7.
- Freeth, T., Bitsakis, Y., Moussas, X., Seiradakis, J.H., Tselikas, A., Mangou, H., Zafeiropoulou, M., Hadland, R., Bate, D., Ramsey, A., Allen, M., Crawley, A., Hockley, P., Malzbender, T., Gelb, D., Ambrisco, W. & Edmunds, M.G., 2006. Decoding the ancient Greek astronomical calculator known as the Antikythera Mechanism. *Nature* 444(30), 587–91.
- Friel, J.J. & Lyman, C.H., 2006. X-ray Mapping in Electron-Beam Instruments. *Microscopy and Microanalysis* 12, 2–25.
- Fujita, T., 2017. Hierarchical nanoporous metals as a path toward the ultimate three-dimensional functionality. *Science and Technology of Advanced Materials* 18(1), 724–40.
- Gale, N. & Stos-Gale, Z. A., 1981. Ancient Egyptian Silver. *Journal of Egyptian Archaeology* 67, 103–15.
- Goldstein, J.I., Newbury, D.E., Michael, J.R., Ritchie, N.W.M., Scott, J.H.J. & Joy, D.C., 2018. *Scanning Electron Microscopy and X-Ray Microanalysis*, 4th Edition. New York: Springer-Verlag.
- Griesser, M., Traum, R., Mayerhofer, K.E., Piplits, K., Denk, R. & Winter, H., 2005. Brown spot corrosion on historic gold coins and medals. *Surface Engineering* 21, 385–92.
- Grimwade, M.F., 2002. *Handbook on soldering and other joining techniques in gold jewellery manufacture*. London: World Gold Council.
- Guerra, M.F., 2004. Fingerprinting ancient gold with proton beams of different energy. *Nuclear Instruments and Methods in Physics Research B* 226, 2004, 185–98.
- Guerra, M.F., 2006. Etruscan gold jewellery pastiches of the Campana's collection revealed by scientific analysis, in *De Re Metallica*, eds. M. Cavalini & G.E. Gigante. Roma: L'Erma di Bretschneider, 103–128
- Guerra, M.F., 2007. Examen et analyse de quelques bijoux de la collection Campana, in *Les bijoux de la collection Campana, de l'antique au pastiche*, eds. F. Gaultier & C. Metzger. Paris: École du Louvre, 145–77.
- Guerra, M.F., 2008. An overview on the ancient goldsmith's skill and the circulation of gold in the past: the role of X-ray based techniques. *X-ray Spectrometry* 37, 317–27.

- Guerra, M.F., 2018. Physicochemical approaches to gold and silver work, an overview: Searching for technologies, tracing routes, attempting to preserve. *Physical Sciences Reviews* 4(2), 1–15.
- Guerra, M.F., 2021. On gold recycling. A physicochemical point of view. *Archaeometry* 64(S1), 134–49.
- Guerra, M.F. & Calligaro, T., 2004. Gold traces to trace gold. *Journal of Archaeological Science* 31, 1199–1208.
- Guerra, M.F. & Pagès Camagna, S., 2019. On the way to the New Kingdom. Analytical study of Queen Ahhotep's gold jewellery (17th Dynasty of Egypt). *Journal of Cultural Heritage* 36, 143–52.
- Guerra, M.F. & Rehren, T., 2009. In-situ examination and analysis of the gold jewellery from the Phoenician tomb of Kition (Cyprus). *ArcheoSciences* 33, 151–8.
- Guerra, M.F. & Tissot, I., 2013. The role of nuclear microprobes in the study and conservation of gold and silver cultural heritage items: an overview. *Nuclear Instruments and Methods in Physics Research B* 306, 227–31.
- Guerra, M.F. & Tissot, I., 2015. Bronze Age and Iron Age gold torcs and earrings from the Iberian Atlantic façade: a non-invasive multi-analytical approach to the characterisation of the alloys and the corrosion. *X-ray spectrometry* 45(1), 5–13.
- Guerra, M.F., Calligaro, T., Radtke, M., Reiche, I. & Riesemeier, H., 2005. Fingerprinting ancient gold by measuring Pt with spatially resolved high energy Sy-XRF. *Nuclear Instruments and Methods in Physics Research Section B* 240(1-2), 505–11.
- Guerra, M.F., Radtke, M., Reiche, I., Riesemeier, H. & Strub, E., 2008. Analysis of trace elements in gold alloys by SR-XRF at high energy at the BAMline. *Nuclear Instruments and Methods in Physics Research B* 266(10), 2334–8.
- Gusmano, G., Montanari, R., Kaciulis, S., Mezzi, A., Montesperelli, G. & Rupprecht, L., 2004a. Surface defects on collection coins of precious metals. *Surface and Interface Analysis* 36, 921–4.
- Gusmano, G., Montanari, R., Kaciulis, S., Montesperelli, G. & Denk, R., 2004b. "Gold corrosion": red stain on a gold Austrian Ducat. *Applied Physics A* 79(2), 205–11.
- Hacke, A.M., Carr, C., Brown, A. & Howell, D., 2003. Investigation into the nature of metal threads in a Renaissance tapestry and the cleaning of tarnished silver by UV/Ozone (UVO) treatment. *Journal of Material Science* 38, 3307–14.
- Hass, G., 1955. Filmed surfaces for reflecting optics. *Journal of the Optical Society of America* 45, 945–52.
- Hess, M. & Robson, S., 2010. 3D colour imaging for cultural heritage artefacts, in *Proceedings of 5th Mid-Term Symposium Close Range Image Measurement Techniques*, eds. J.P. Mills, D.M. Barber, P.E. Miller & I. Newton. International Archives of the Photogrammetry, Remote Sensing and Spatial Information Sciences 38(5), 288–92.
- Hinsch, J., 2007. Mating Cameras to Microscopes in Digital Microscopy, in *Methods in Cell Biology* 81, 3rd Edition, eds. G. Sluder & D.E. Wolf. Elsevier Inc. 55–21.
- Huang, X., Uffelman, E., Cossairt, O., Walton, M. & Katsagelos, A.K., 2016. Computational Imaging for Cultural Heritage: Recent developments in spectral imaging, 3-D surface measurement, image relighting, and X-ray mapping. *IEEE Signal Processing Magazine* 33(5), 130–8.
- Huang, H., Xu, G. & Liu, X., 2021. Study on the Purity of Gold Leaf in a SO₂ Atmosphere at Ambient Temperature. *Material* 14(9), 2425.
- Ioanid, E.G., Ioanid, A., Rusu, D.E. & Doroftei, F., 2011. Surface investigation of some medieval silver coins cleaned in high-frequency cold plasma. *Journal of Cultural Heritage* 12, 220–6.
- Jansen, M., Hauptmann, A., Klein, S., & Zettler, R.L., 2021. Trace Elements and Isotopes: The Origin of Gold from Ur from a Geochemical Point of View, in *Ur in the Twenty-First Century CE*, eds. G. Frame, J. Jeffers & H. Pittman. Pennsylvania: Eisenbrauns, University Park, 273–92.
- Keast, V.J., Myles, T.A., Shahcheraghi, N. & Cortie, M.B., 2016. Corrosion process of triangular silver nanoparticles compared to bulk silver. *Journal of Nanoparticle Research* 18, 45–66.
- Keturakis, C.J., Notis, B., Blenheim, A., Miller, A.C., Pafchek, R., Notis, M.R. & Wachs, I.E., 2016. Analysis of corrosion layers in ancient Roman silver coins with high resolution surface spectroscopic techniques. *Applied Surface Science* 376, 224–51.
- Kirz, J. & Vaughan, D., 1985. *X-ray Data Booklet*. Berkeley: Lawrence Berkeley Laboratory, University of California.
- Kodak, 1966. *Industrial Radiography*. London: Kodak Ltd.
- Kovacs, R., Schlosser, S., Staub, S.P., Schmiderer, A., Pernicka, E. & Günther, D., 2009. Characterization of calibration materials for trace element analysis and fingerprint studies of gold using LA-ICP-MS. *Journal of Analytical Atomic Spectrometry* 24(4), 476–83.
- Lang, J. & Middleton, A. (eds.), 2005. *Radiography of Cultural Material*, 2nd edition. Oxford: Butterworth-Heinemann.
- Lee, H.J., Chen, Y.B. & Zhang, Z.M., 2006. Directional radiative properties of anisotropic rough silicon and gold surfaces. *International Journal of Heat and Mass Transfer* 49(23), 4482–95.
- Lee, J.M., Yu, J. & Koh, Y., 2003. Experimental study on the effect of wavelength in the laser cleaning of silver threads. *Journal of Cultural Heritage* 4, 157–61.
- Lemasson, Q., Moignard, B., Pacheco, C., Pichon, L. & Guerra, M.F., 2015. Fast mapping of gold jewellery from ancient Egypt with PIXE: Searching for hard-solders and PGE inclusions. *Talanta* 143, 279–86.
- Liang, C., Yang, C. & Huang, N., 2011. Investigating the tarnish and corrosion mechanisms of Chinese gold coins. *Surface and Interface Analysis* 43, 763–9.
- Lilyquist, C., 1993. Granulation and Glass: Chronological and Stylistic Investigations at Selected Sites, c. 2500–1400 BCE. *Bulletin of the American Schools of Oriental Research* 290/291, 29–94.
- Lilyquist, C., 1994. The Dilbat hoard. *The Metropolitan Museum Journal* 29, 5–36.
- Lilyquist, C., 2003. *The tomb of the three foreign wives of Tuthmosis III*. New York: The Metropolitan Museum of Art.
- Lu, T., Zhang, J., Lan, Y., Ma, Y., Chen, H., Ke, J. Wu, Z. & Tang, M., 2015. Characterization of tarnish spots in Chinese high-purity gold jewelry. *Gems & Gemology* 51, 410–18.

- Lucas, A., 1926. *Ancient Egyptian materials and industries*. London: Edward Arnold Publishers Ltd.
- MacDonald, L.W., 2010. The limits of resolution, in *Proceedings of the 2010 international conference on Electronic Visualisation and the Arts*, eds. A. Seal, J.P. Bowen, J.P. Bowen & K. Ng, Swindon: BCS Learning & Development Ltd., 149–56.
- MacDonald, L.W., 2011. Choosing optimal wavelengths for colour laser scanners, in *Nineteenth Color and Imaging Conference Proceedings*. San José, California: Society for Imaging Science and Technology, 357–62.
- MacDonald, L.W., 2014. Colour and directionality in surface reflectance. *Proceedings of Artificial Intelligence and the Simulation of Behaviour*. London: Society for the Study of Artificial Intelligence and the Simulation of Behaviour.
- MacDonald, L.W., 2015. Surface reconstruction from photometric normals with reference height measurements, in *Optics for Arts, Architecture, and Archaeology V*, eds. L. Pezzati & P. Targowski. SPIE Conference Proceedings 9527. The International Society for Optical Engineering, Article 952706.
- MacDonald, L.W. & Robson, S., 2010. Polynomial texture mapping and 3D representations, in *Proceedings of 5th Mid-Term Symposium Close Range Image Measurement Techniques*, eds. J.P. Mills, D.M. Barber, P.E. Miller & I. Newton. International Archives of the Photogrammetry, Remote Sensing and Spatial Information Sciences 38(5), 422–7.
- MacDonald, L.W., Hosseininaveh Ahmadabadian, A. & Robson, S., 2015. Determining the coordinates of lamps in an illumination dome, in *Videometrics, Range Imaging, and Applications XIII*, eds. F. Remondino & M.R. Shortis. SPIE Conference Proceedings 9528. The International Society for Optical Engineering, Article 95280I.
- MacDonald, L.W., Guerra, M.F., Pillay, R., Hess, M., Quirke, S., Robson, S. & Hosseininaveh Ahmadabadian, A., 2014. Practice-based comparison of imaging methods for visualization of toolmarks on an Egyptian scarab, in *Image and Signal Processing*, eds. A. Elmoataz, O. Lezoray, F. Nouboud & D. Mammass. Lecture Notes in Computer Science 8509. Cham, Switzerland: Springer, 239–46.
- Martinón-Torres, M., Valcárcel Rojas, R., Sáenz Samper, J. & Guerra, M.F., 2012. Metallic encounters in Cuba: The technology, exchange and meaning of metals before and after Columbus. *Journal of Anthropological Archaeology* 31, 439–54.
- Maryon, H., 1941. Archaeology and Metallurgy. I. Welding and Soldering, *MAN* 41(85), 118–24.
- Maxwell, J.A., Campbell, J.L. & Teesdale, W.J., 1989. The Guelph PIXE software. *Nuclear Instruments and Methods in Physics Research B* 43, 218–30.
- McGovern, P.E., 1985. *Late Bronze Age Palestinian pendants. Innovation in a Cosmopolitan Age*. JSTO/ASOR Monograph Series 1. Sheffield: JSOT Press.
- Meeks, N.D., 1998. Pre-hispanic goldwork in the British Museum: some recent technological studies. *Boletín Museo del Oro* 44-45, 107–37.
- Meeks, N.D., 2000. Scanning Electron Microscopy of the Refractory Remains and the Gold, in *King Croesus' Gold*, eds. A. Ramage & P. Craddock. London: British Museum Press, 99–156.
- Meeks, N.D. & Tite, M.S., 1980. The analysis of platinum-group element inclusions in gold antiquities. *Journal of Archaeological Science* 7(3), 267–75.
- Meeks, N., Cartwright, C., Meek, A. & Mongiatti, A. (eds.), 2012. *Historical technology, materials and conservation. SEM and Microanalysis*. London: Archetype Publications and The British Museum.
- Meidinger, N., Andritschke, R., Hartmann, R., Herrmann, S., Holl, P., Lutz, G. & Strueder, L., 2006. pnCCD for photon detection from near-infrared to X-rays. *Nuclear Instruments and Methods in Physics Research A* 565(1), 251–7.
- Merriman, C.C., Bahr, D.F. & Norton, M.G., 2005. Environmentally induced failure of gold jewelry alloys. *Gold Bulletin* 38, 113–19.
- Miniaci, G., La Niece, S., Guerra, M.F. & Hacke, M., 2013. Analytical study of the first royal Egyptian heart-scarab, attributed to a Seventeenth Dynasty king, Sobekemsaf. *British Museum Technical Research Bulletin* 7, 53–60.
- Morigi, M.P., Casali, F., Bettuzzi, M., Brancaccio, R. & D'Errico, V., 2010. Application of X-ray Computed Tomography to Cultural Heritage diagnostics. *Applied Physics A* 10(3), 653–61.
- Negbi, O., 1970. *The hoards of goldwork from Tell el-Ajjul*. Studies in Mediterranean Archaeology. Göteborg: Södra, Vägen 61.
- Nestler, G. & Formigli, E., 2004. *Granulazione etrusca un'antica arte orafa*. Siena: Nuova imagine.
- Northover, S.M. & Northover, J.P., 2012. Applications of Electron Backscatter Diffraction (EBSD) in Archaeology, in *Historical technology, materials and conservation. SEM and Microanalysis*, eds. N. Meeks, C. Cartwright, A. Meek & A. Mongiatti. London: Archetype Publications and The British Museum, 76–85.
- Oddy, A., 1977. The production of gold wire in Antiquity. Hand-making methods before the introduction of the draw-plate. *Gold Bulletin* 3(10), 79–87.
- Oddy, A., 2004. The manufacture of wire since the Bronze Age: a technological investigation using the microscope, in *Physics methods in archaeometry*, eds. M. Martini, M. Milazzo & M. Piacentini. Amsterdam: IOS Press, 257–67.
- Ogden, J.M., 1977. Platinum group metal inclusions in Ancient gold artifacts. *Journal of the Historical Metallurgy Society* 11(2), 53–70.
- Olsen, S.L., 1988. Applications of Scanning Electron Microscopy in Archaeology. *Advances in Electronics and Electron Physics* 71, 357–80.
- Ordavo, I., Ihle, S., Arkadiev, V., Scharf, O., Soltau, H., Bjeoumikhov, A., Bjeoumikhova, S., Buzanich, G., Gubzhokov, R., Gunther, A., Hartmann, R., Holl, P., Kimmel, N., Kuhbacher, M., Lang, M., Langhoff, N., Liebel, A., Radtke, M., Reinholz, U., Riesemeier, H., Schaller, G., Schopper, F., Struder, L., Thamm, C. & Wedell, R., 2011. A new pnCCD-based color X-ray camera for fast spatial and energy-resolved measurements. *Nuclear Instruments & Methods in Physics Research Section A* 654(1), 250–7.

- Palomar, T., Barat, B.R., García, E. & Cano, E., 2016. A comparative study of cleaning methods for tarnished silver. *Journal of Cultural Heritage* 17, 20–6.
- Paris, O., Li, C., Siegel, S., Weseloh, G., Emmerling, F., Riesemeier, H., Erko, A. & Fratzl, P., 2007. A new experimental station for simultaneous X-ray micro-beam scanning for small- and wide-angle scattering and fluorescence at BESSY II. *Journal of Applied Crystallography* 40, S466–S470.
- Parrini, P., Formigli, E. & Mello, E., 1982. Etruscan Granulation: Analysis of Orientalizing Jewelry from Marsiliana d'Albegna. *American Journal of Archaeology* 86(1), 118–21.
- Perea, A., García Vuelta, O. & Fernández Freire, C., 2010. *El proyecto AU, estudio arqueométrico de la producción de oro en la Península Ibérica*. Madrid: CSIC.
- Pérez-Arantegui, J. & Larrea, A., 2015. Electron backscattering diffraction as a complementary analytical approach to the microstructural characterization of ancient materials by electron microscopy. *Trends in Analytical Chemistry* 72, 193–201.
- Petrie, W.M.F., 1909. *Qurneh*. London: British School of Archaeology in Egypt.
- Petrie, W.F., 1931–4. *Ancient Gaza I to IV*. British School of Archaeology in Egypt. London: Quaritch.
- Petrie, W.F., 1952. *City of Shepherd Kings. Ancient Gaza V*. British School of Archaeology in Egypt. London: Quaritch.
- Petrie, W.M.F. & Quibell, J.E., 1896. *Naqada and Ballas*. London: B. Quaritch ed.
- Pichon, L., Moignard, B., Lemasson, Q., Pacheco C. & Walter, P., 2014. Development of a multi-detector and a systematic imaging system on the AGLAE external beam. *Nuclear Instruments and Methods in Physics Research B* 318, 27–31.
- Pichon, L., Calligaro, T., Lemasson, Q., Moignard, B. & Pacheco, C., 2015. Programs for visualization, handling and quantification of PIXE maps at the AGLAE facility. *Nuclear Instruments and Methods in Physics Research B* 363, 48–54.
- Platz-Horster, G. & Tietz, H.U., 1995. Sulla granulazione degli etruschi, in *Preziosi in oro, avorio, osso e corno*, ed. E. Formigli. Siena: Nuova Imagine, 56–62.
- Politis, T., 2001. Gold and Granulation: Exploring the Social Implications of a Prestige Technology in the Bronze Age Mediterranean, in *The social context of technological change: Egypt and the Near East, 1650–1550 BC*, ed. A.J. Shortland. Oxford: Oxbow Books, 161–94.
- Politis, T., Abraham, M., Northover, P. & Grime, G., 2002. PIXE, Electron Microprobe Data, and Experimental Archaeology: Tell el-Ajjul and Pilot Studies of Gold Granulation Joining Practices in the Mediterranean Bronze Age. *Materials Research Society Symposium Proceedings* 712, II7.3.1–10.
- Ponting, M., 2004. The scanning electron microscope and the archaeologist. *Physics Education* 39(2), 166–70.
- Pulak, C., 2008. The Uluburun shipwreck and Late Bronze Age trade, in *Beyond Babylon. Art Trade and Diplomacy in the Second Millennium BC*, eds. J. Aruz, K. Benzel & J. M. Evans. New York / New Haven / London: The Metropolitan Museum of Art / Yale University Press, 289–310.
- Radtke, M., Reinholz, U. & Gebhard, R., 2017. Synchrotron Radiation-Induced X-Ray Fluorescence (SRXRF) Analyses of the Bernstorff gold. *Archaeometry* 59(5), 891–9.
- Radtke, M., Buzanich, G., Guilherme, A., Reinholz, U., Riesemeier, H., Scharf, O., Scholz, P. & Guerra, M.F., 2016. Double Dispersive X-Ray Fluorescence (D2XRF) based on an Energy Dispersive pnCCD detector for the detection of platinum in gold. *Microchemical Journal* 125, 56–61.
- Radtke, M., Reiche, I., Reinholz, U., Riesemeier, H. & Guerra, M.F., 2013. Beyond the Great Wall: Gold of the Silk Roads and the First Empire of the Steppes. *Analytical Chemistry* 85(3), 1650–6.
- Randin, J.P., Ramoni, P. & Renaud, J.P., 1992. Tarnishing of AuAgCu alloys. Effect of the composition. *Materials and Corrosion* 43, 115–23.
- Rapson, W.S., 1996. Tarnish resistance, corrosion and stress corrosion cracking of gold alloys. *Gold Bulletin* 29, 61–9.
- Riesemeier, H., Ecker, K., Görner, W., Müller, B.R., Radtke, M. & Krumrey, M., 2005. Layout and first XRF Applications of the BAMline at BESSY II. *X-Ray Spectrometry* 34(2), 160–3.
- Rifai, M.M. & El Hadidi, N.M., 2010. Investigation and analysis of three gilded wood samples from the tomb of Tutankhamun, in *Decorated Surfaces on Ancient Egyptian Objects, Technology, Deterioration and Conservation*, eds. J. Dawson, C. Rozeik & M.M. Wright. London: Archetype Publications Ltd., 16–24.
- Saeger, K.E. & Rodies, J., 1977. The colour of gold and its alloys. *Gold Bulletin* 10(1), 10–14.
- Saleem, S.N. & Hawass, Z., 2014. Multidetector Computed Tomographic study of amulets, jewelry, and other foreign objects in Royal Egyptian Mummies dated from the 18th to 20th Dynasties. *Journal of Computer Assisted Tomography* 38(2), 153–8.
- Salem, Y., 2017. The influence of gaseous pollutants on silver artifacts tarnishing. *Open Journal of Air Pollution* 6, 135–48.
- Sarkar, N.K., Fuys, R.A. & Stanford, J.W. 1979. The chloride corrosion of low-gold casting alloys. *Journal of Dental Research* 58, 568–75.
- Sawada, H., Borisenko, K.B., Shima, M., Ikita, K., Hashiguchi, H., Onishi, I., Okunishi, E. & Kirkland, A.I., 2019. Corrosion of Gold by a Nanoscale Gold and Copper Beltlike Structure. *Journal of Physical Chemistry C* 123(32), 19920–6.
- Scharf, O., Ihle, S., Ordavo, I., Arkadiev, V., Bjeoumikhov, A., Bjeoumikhova, S., Buzanich, G., Gubzhokov, R., Guenther, A., Hartmann, R., Kuehbacher, M., Lang, M., Langhoff, N., Liebel, A., Radtke, M., Reinholz, U., Riesemeier, H., Soltau, H., Strueder, L., Thuenemann, A.F. & Wedell, R., 2011. Compact pnCCD-Based X-ray Camera with High Spatial and Energy Resolution: A Color X-ray Camera. *Analytical Chemistry* 83(7), 2532–8.
- Schlosser, S., Reinecke, A., Schwab, R., Pernicka, E., Sonetra, S. & Laychour, V., 2012. Early Cambodian gold and silver from Prohear: composition, trace elements and gilding. *Journal of Archaeological Science* 39(9), 2877–87.
- Schorsch, D., 1995. The Gold and Silver Necklaces of Wah. A Technical Study of an Unusual Metallurgical Joining

- Method, in *Conservation in ancient Egyptian collections*, eds. C. Brown, F. Macalister & M. Wright. London: Archetype Publications, 127–35.
- Schreiner, M., Melcher, M. & Uhlir, K., 2007. Scanning electron microscopy and energy dispersive analysis: applications in the field of cultural heritage. *Analytical and Bioanalytical Chemistry* 387, 737–47.
- Sciau, Ph., 2016. Transmission Electron Microscopy: Emerging Investigations for Cultural Heritage Materials, in *Advances in Imaging and Electron Physics* 198, ed. P.W. Hawkes. Elsevier Inc., 43–67.
- Scrivano, S., Ruberto, C., Gómez-Tubío, B., Mazzinghi, A., Ortega-Feliu, I., Ager, F.J., Laclavetine, K., Giuntini, L. & Respaldua, M.A., 2017. In-situ non-destructive analysis of Etruscan gold jewels with the micro-XRF transportable spectrometer from CAN. *Journal of Archaeological Science: Reports* 16, 185–93.
- Seipel, W., 2001. *Gold der Pharaonen*. Kunsthistorischen Museum. Viena: Skira ed.
- Shafer, S.A., 1985. Using color to separate reflection components. *Color Research & Application* 10(4), 210–18.
- Siano, S. & Salimbeni, R., 2010. Advances in laser cleaning of artwork and objects of historical interest: the optimized pulse duration. *Accounts of Chemical Research* 43(6), 739–50.
- Silverman, D., 1997. *Searching for Ancient Egypt*. Dallas: Dallas Museum of Art, Cornell University Press.
- Snape, S., 1987. *Mortuary Assemblages from Abydos I*. PhD Dissertation, University of Liverpool.
- Sokaras, D., Mueller, M., Kolbe, M., Beckhoff, B., Zarkadas, C. & Karydas, A.G., 2010. Resonant Raman scattering of polarized and unpolarized X-ray radiation from Mg, Al, and Si. *Physical Review A* 81(1), 012703.
- Solé, V.A., Papillon, E., Cotte, M., Walter, P. & Susini, J., 2007. A multiplatform code for the analysis of energy-dispersive X-ray fluorescence spectra. *Spectrochimica Acta Part B* 62, 63–8.
- Standish, C., Dhuime, B., Hawkesworth, C. & Pike, A., 2015. A Non-local Source of Irish Chalcolithic and Early Bronze Age Gold. *Proceedings of the Prehistoric Society* 81, 149–77.
- Stokes, D.J., 2008. *Principles and Practice of Variable Pressure Environmental Scanning Electron Microscopy (VP-ESEM)*. John Wiley & Sons, Ltd.
- Stokes, D.J., 2012. Environmental scanning electron microscopy for biology and polymer science, *Microscopy and Analysis*, 25th Anniversary Issue, 67–71.
- Tate, J., Eremin, K., Troalen, L.G., Guerra, M.F., Goring, E. & Manley, W.P., 2009. The 17th dynasty gold necklace from Qurneh, Egypt. *ArcheoSciences* 33, 121–8.
- Thiaudière, C., 2005. *Étude technique et typologique de la bijouterie ptolémaïque et romaine d'Égypte*. PhD Dissertation, Université de Limoges, section Histoire ancienne et archéologie.
- Tissot, I., Correia, J., Monteiro, O.C., Barreiros, M.A. & Guerra, M.F., 2019. When gold stops glittering: corrosion mechanisms of René Lalique's Art Nouveau jewellery. *Journal of Analytical Atomic Spectrometry* 34, 1216–22.
- Tissot, I., Monteiro, O.C., Barreiros, M.A., Correia, J. & Guerra, M.F., 2016. Corrosion of silver alloys in sulphide environments: a multianalytical approach for surface characterisation. *RSC Advances* 6, 51856–63.
- Tissot, I., Monteiro, O.C., Barreiros, M.A., Correia, J. & Guerra, M.F., 2017. The influence of the constituent elements on the corrosion mechanisms of silver alloys in sulphide environments: the case of sterling silver. *RSC Advances* 7, 28564–72.
- Tissot, I., Tissot, M. & Guerra, M.F., 2014. Atmospheric corrosion in museum context – the case of the treasure room from the National Archaeology Museum, Lisbon. *Corrosão e Protecção de Materiais* 4, 73–7.
- Tissot, I., Tissot, M., Manso, M., Alves, L.C., Barreiros, M.A., Marcelo, T., Carvalho, M.L., Corregidor, V. & Guerra, M.F., 2013. The earrings of Pancas Treasure: Analytical study by X-ray based techniques – A first approach. *Nuclear Instruments and Methods in Physics Research B* 306, 236–40.
- Tissot, I., Troalen, L.G., Manso, M., Ponting, M., Radtke, M., Reinholz, U., Barreiros, M.A., Shaw, I., Carvalho, M.L. & Guerra, M.F., 2015. A multi-analytical approach to gold in Ancient Egypt: Studies on provenance and corrosion. *Spectrochimica Acta Part B* 108, 75–82.
- Troalen, L.G. & Guerra, M.F., 2016. Gold from the tomb of Scribe Beri: a comparative analytical approach to the New Kingdom gold grave goods from Riqqa (Egypt). *Applied Physics A* 122, 210–16.
- Troalen, L., Guerra, M.F., Tate, J. & Manley, W.P., 2009. Technological study of gold jewellery pieces dated from Middle Kingdom to New Kingdom in Egypt. *ArcheoSciences* 33, 111–19.
- Troalen, L.G., Cox, D., Skinner, T., Ramsey, A. & Bate, D., 2010. Three-dimensional Computed Tomography X-Radiographic investigation of a 17th century watch from the wreck of the Swan, off Duart Point, Mull, Scotland. *International Journal of Nautical Archaeology* 39, 165–171.
- Troalen, L., Guerra, M.F., Maitland, M., Ponting, M. & Price, C., 2019. Analytical study of the Middle Kingdom group of gold jewellery from tomb 124 at Riqqa, Egypt. *X-ray Spectrometry* 48(6), 586–96.
- Troalen, L.G., Tissot, I., Maitland, M. & Guerra, M.F., 2016. Jewellery of a young Egyptian girl: Middle Kingdom goldwork from Haraga tomb 72. *Historical Metallurgy* 49, 75–86.
- Troalen, L.G., Guerra, M.F. & Tate, J., 2014. Goldwork in Ancient Egypt. Workshop practices at Qurneh in the 2nd Intermediate Period. *Journal of Archaeological Sciences* 50, 219–26.
- Tufnell, O., 1983. Some Gold Bird Ornaments Falcon or Wryneck? *Anatolian Studies* 33, 57–66.
- Ul-Hamid, A., 2018. *A Beginners' Guide to Scanning Electron Microscopy*. Switzerland: Springer Nature.
- Vassilou, P., Novakovic, J., Ingo, G.M. & de Caro, T., 2009. Corrosion of ancient silver alloys, in *Corrosion control in service of society, 17th International Corrosion Congress*. Houston: NACE International Inc., 2879.
- Viguerie, L. de, Duran, A., Bouquillon, A., Solé, V.A., Castaing, J. & Walter, P., 2009. Quantitative X-ray fluorescence analysis of an Egyptian faience pendant and comparison with PIXE. *Analytical and Bioanalytical Chemistry* 395, 2219–25.

- Wanhill, R.J.H., Steijaart, J.P.H.M., Leenheer, R. & Koenis, J.F.W., 1998. Damage assessment and preservation of an Egyptian silver vase (300–200 BC). *Archaeometry* 40, 123–37.
- Wanhill, R.J.H., 2011. Case histories of ancient silver embrittlement. *Journal of Failure Analysis and Prevention* 11, 178–85.
- Weissmüller, J., Newman, R.C., Jin, H.J., Hodge, A.M. & Kysar, J.W., 2009. Nanoporous metals by alloy corrosion: formation and mechanical properties. *Materials Research Society Bulletin* 34(8), 577–86.
- Wharton, G., Maish, S.L. & Ginell, W.S., 1990. A comparative study of silver cleaning abrasives. *Journal of the American Institute for Conservation* 29, 13–31.
- Williams, D.B. & Carter, C.B., 2009. *Transmission Electron Microscopy. A Textbook for Materials Science*, 2nd edition. Springer Science, Business Media.
- Wolf, D.E., 2007. The Optics of Microscope Image Formation in Digital Microscopy, in *Methods in Cell Biology* 81, 3rd edition, eds. G. Sluder & D.E. Wolf. Elsevier Inc., 12–42.
- Wu, Q., Watts, B., Döbeli, M., Müller, J., Butz, B., Lombardo, T., Schmidt-Ott, K., Fink, R., Nolting, F. & Ganz, D., 2021. Medieval nanotechnology: Thickness determination of Zwischgold samples. *Journal of Cultural Heritage* 49, 211–21.
- Yang, C., Liang, C. & Wang, P., 2007. Investigation of the tarnish on the surface of a panda gold coin. *Rare Metals* 26, 6–73.

Ancient Egyptian gold

This book aims to provide a new level of synthesis in the study of gold jewellery made in Egypt between 3500 BC and 1000 BC, integrating the distinct approaches of archaeology, materials science and Egyptology. Following accessible introductions to the art and use of gold in Ancient Egypt, and to current advances in technical analyses, the volume presents detailed results on the manufacturing technology and elemental composition of some 136 objects in the collections of six European museums, with discussion of the findings in historical and cultural contexts. The questions generated by the jewellery buried with a woman and a child at Qurna (Thebes) led to investigation of assemblages and individual artefacts from later and earlier periods in varied social contexts, from the rural environment of Qau and Badari, to sites connected with urban or royal centres, such as Riqqa, Haraga and Lahun. A final discussion of the Qurna group provides an agenda for future research.

Editors:

María F. Guerra is Director of research in Chemistry at the National Center for Scientific Research (UMR 8233 MONARIS, Sorbonne University). Her interests are in the analytical study of goldwork.

Marcos Martín-Torres is Pitt-Rivers Professor of Archaeological Science at the University of Cambridge, and editor of the *Journal of Archaeological Science*. He has a particular interest in past technologies.

Stephen Quirke is Edwards Professor of Egyptian Archaeology and Philology at the UCL Institute of Archaeology. His interests include Middle Kingdom social history, as well as the history of archaeology and collections.



Published by the McDonald Institute for Archaeological Research,
University of Cambridge, Downing Street, Cambridge, CB2 3ER, UK.

The McDonald Institute for Archaeological Research exists to further research by Cambridge archaeologists and their collaborators into all aspects of the human past, across time and space. It supports archaeological fieldwork, archaeological science, material culture studies, and archaeological theory in an interdisciplinary framework. The Institute is committed to supporting new perspectives and ground-breaking research in archaeology and publishes peer-reviewed books of the highest quality across a range of subjects in the form of fieldwork monographs and thematic edited volumes.

Cover design by Dora Kemp and Ben Plumridge.

ISBN: 978-1-913344-13-9

